STARS

Electronic Theses and Dissertations, 2004-2019

2006

Integrated Inp Photonic Switches

Daniel May-Arrioja
University of Central Florida

INTEGRATED INP PHOTONIC SWITCHES

by

DANIEL ALBERTO MAY ARRIOJA
B.S. Tuxtla Gutierrez Technical Institute, 1995
M.S. National Institute for Astrophysics, Optics, and Electronics, 1998
M.S. University of Central Florida, 2002

A dissertation submitted in partial fulfillment of the requirements
for the degree of Doctor of Philosophy
in the College of Optics and Photonics: CREOL and FPCE
at the University of Central Florida
Orlando, Florida

Fall Term
2006

Major Professor: Patrick LiKamWa

ABSTRACT

Photonic switches are becoming key components in advanced optical networks because of the large variety of applications that they can perform. One of the key advantages of photonic switches is that they redirect or convert light without having to make any optical to electronic conversions and vice versa, thus allowing networking functions to be lowered into the optical layer. InP-based switches are particularly attractive because of their small size, low electrical power consumption, and compatibility with integration of laser sources, photo-detectors, and electronic components.

In this dissertation the development of integrated InP photonic switches using an area-selective zinc diffusion process has been investigated. The zinc diffusion process is implemented using a semi-sealed open-tube diffusion technique. The process has proven to be highly controllable and reproducible by carefully monitoring of the diffusion parameters. Using this technique, isolated p-n junctions exhibiting good I-V characteristics and breakdown voltages greater than 10 V can be selectively defined across a semiconductor wafer.

A series of Mach-Zehnder interferometric (MZI) switches/modulators have been designed and fabricated. Monolithic integration of 1x2 and 2x2 MZI switches has been

demonstrated. The diffusion process circumvents the need for isolation trenches, and hence optical losses can be significantly reduced. An efficient optical beam steering device based on InGaAsP multiple quantum wells is also demonstrated. The degree of lateral current spreading is easily regulated by controlling the zinc depth, allowing optimization of the injected currents. Beam steering over a 21 microns lateral distance with electrical current values as low as 12.5 mA are demonstrated. Using this principle, a reconfigurable 1x3 switch has been implemented with crosstalk levels better than -17 dB over a 50 nm wavelength range. At these low electrical current levels, uncooled and d.c. bias operation is made feasible.

The use of multimode interference (MMI) structures as active devices have also been investigated. These devices operate by selective refractive index perturbation on very specific areas within the MMI structure, and this is again realized using zinc diffusion. Several variants such as a compact MMI modulator that is as short as 350 μm, a robust 2x2 photonic switch and a tunable MMI coupler have been demonstrated.

To my parents and family, specially my wife Lety, who has always supported me in

everything through all these many years.

ACKNOWLEDGMENTS

I am very grateful to Dr. Patrick LiKamWa for his continuous support during the development of the dissertation. I will always appreciate the freedom to start new projects. This has given me the confidence to realize different projects, and will be very valuable in the future. I would also like to thank my dissertation committee for taking the time to review this dissertation.

The time I spent at CREOL has been a marvelous experience, with so much research going around. I am also very thankful to the CREOL professors and colleagues, specially my group members (C. Kim, X. Dong, I. Shubin, I. Kim, N. Bickel, and H. Bang), regardless of their busy schedules they were always happy to help. I also want to express my appreciation to Dr. Javier J. Sánchez-Mondragón for his continuous support and encouragement.

Finally, but not least, I am grateful to my parents, brothers and my sister. They have been always there when I needed them the most. I want to specially thank my wife and my daughters for their never-ending support and cheers.

TABLE OF CONTENTS

LIST OF FIGURES

xiii

xiv

LIST OF TABLES

LIST OF ACRONYMS

WDM	Wavelength-Division Multiplexing
TDM	Time-Division Multiplexing
PICs	Photonic Integrated Circuits
MEMS	Micro-Electro-Mechanical Systems
SOAs	Semiconductor Optical Amplifiers
HBTs	Heterojunction Bipolar Transistors
HEMTs	High Electron Mobility Transistors
MQW	Multiple Quantum Wells
QCSE	Quantum Confined Stark Effect
QW	Quantum Well
MOCVD	Metal Organic Chemical Vapor Deposition
APCVD	Atmospheric Pressure Chemical Vapor Deposition
LPCVD	Low Pressure Chemical Vapor Deposition
PECVD	Plasma Enhanced Chemical Vapor Deposition
RF	Radio Frequency
RIE	Reactive Ion Etching
DI	Deionized

SEM	Scanning Electron Microscopy
ICP/RIE	Inductively Coupled Plasma Reactive Ion Etching
SIMS	Secondary Ion Mass Spectrometry
TLM	Transmission Line Method
RTA	Rapid Thermal Annealing
I-V	Current-Voltage
MZI	Mach-Zehnder Interferometer
FD-BPM	Finite Difference Beam Propagation Method
BOE	Buffered Oxide Etchant
BCB	Benzocyclobutene
FWHM	Full Width Half Maximum
MMI	Multimode Interference
OXCs	Optical Cross-Connects
BPM	Beam Propagation Method
MPA	Guided-Mode Propagation Analysis
ER	Extinction Ratio

CHAPTER ONE: INTRODUCTION

In the past two decades the demand for information transmission capacity has been increasing very rapidly. The main driving force has been the rapid growth of internet applications such as the world-wide-web, business and data transfers, internet banking, media downloading, voice over IP, etc. This explosive growth has been accommodated using optical fiber telecommunications because of the large bandwidth in excess of 50 THz [1] that optical fibers inherently possess. However it is technologically nearly impossible to exploit all of the available bandwidth using a single high-capacity channel. An elegant solution to this problem has been the superposition of many concurrent signals on a single fiber, each one with a different wavelength; which is known as wavelength-division multiplexing (WDM). The volume of information to be transmitted and processed is expected to increase even more rapidly in the future, with some estimations anticipating that communications and signal-processing systems will have to fulfill a throughput of 1 Tb/s or even 5 Tb/s by the year 2010 [2]. Such an improvement can only be achieved by substantial improvements in both system and device technologies.

On the system perspective different approaches have been implemented to achieve Tb/s capacity. Recently, the feasibility of a transmission throughput exceeding 1

Tb/s was experimentally demonstrated by using either time-division multiplexing (TDM) or WDM [3-5]. However, to fully deploy such systems new technologies and devices have to be developed. Among the many devices required in advanced optical networks, photonic switches are becoming key components because they can perform a variety of applications, particularly in signal routing and time-division signal processing. In these applications, the optical transparency of photonic switches modules offers simplified and higher-capacity system operation, by allowing networking function to be lowered to the optical layer. One of the major advantages of photonic switches is that it avoids the need for optical-electronic and electronic-optical (o-e-o) conversions. Such conversions not only limit the versatility and transparency of the system, but can also amount to signal deterioration and to errors being introduced. In fact, the elimination of such o-e-o conversions will result in a major decrease in the overall system cost, since the equipment associated with these conversions represents the main cost associated in today's networks.

Another critical element in future optical networks is the integration of different photonic and electronic components on a single chip, the so-called Photonic Integrated Circuits (PICs). PICs are becoming increasingly important, because this approach has the advantage that one obtains a small and compact unit in which all the components are connected by means of waveguides. This improves the robustness of the circuit, and reduces its sensitivity to the environment. Even more importantly, since packaging costs are a substantial, if not the main part of the component cost, it is more cost effective to integrate multiple components monolithically within a single package [6]. For Photonic

integrated Circuits to become more attractive, the resulting chip should be able to process both optical and electronic signal. More importantly, the development of reliable and reproducible integration techniques is critical for the fabrication of planar high-quality PICs. This includes the delineation of passive and active optical regions, as well as the integration of the required drivers for such devices. Material selection becomes a critical issue since it has to provide a suitable platform in which optical and electronic devices can be integrated.

1.1 Enabling Switching Technologies

Over the years different materials and configurations have been employed for the development of photonic switches. They can be divided by the physical switching mechanism, such as acousto-optic, thermo-optic, electro-optic, and even electro-mechanical in nature, depending on the application requirements. In the following, a brief description of some switching technologies is provided, and the advantage of using semiconductors is emphasized.

Mechanical: Micro-electro-mechanical systems (MEMS) have progressively emerged as a very mature technology. Using MEMS, large arrays of photonic switches can be produced to implement optical cross-connecting functions [7, 8]. The main advantages of MEMS is that low crosstalk (< -50 dB), low loss, and polarization independent devices can be obtained. However, their switching speed is relatively slow (~ 5 ms), which is not a major limitation for certain applications.

Thermo-Optic: The effect has been primarily used with silica-on-silicon and polymer materials. The technology is quite advanced and had been used to fabricate a variety of complex devices [9, 10]. They operate by passing current through a metallic thin film, which in turns heats the waveguide, and induces a temperature dependent index change that can be used for switching. Electrical power consumption and switching speed (~1 ms) are the most relevant issues for thermo-optic devices.

Acousto-Optic: Acousto-optic switches receive acoustically-induced pressure waves from a RF-fed piezoelectric transducer to generate a traveling phase grating in optical waveguides. The induced grating then diffracts the light to the desired port. Using this technology, optical switches in $LiNbO_3$ and GaAs with switching speeds on the order of 1 μs and crosstalk levels better than -15 dB have been demonstrated [11, 12]. These devices are also well suited for free-space switches and cross-connects.

Liquid Crystal: Liquid crystal switches can use polarization manipulation of individually addressable liquid-crystal arrays placed between polarizing filters [13, 14]. Switching matrices have been demonstrated using this technology, with the main problem being the insertion loss (> 10 dB). Single switches exhibit crosstalk better than -35 dB and switching speeds of less than 100 ms. The technology is very mature with the main concern being temperature dependence if not properly designed.

Electro-Optic: The electro-optic refractive index change can be separated into

4

electric field and carrier induced refractive index changes. The first is due to the linear (Pockels) electro-optic effect and the quadratic (Kerr) electro-optic effect. The effect is present in certain type of crystals, and has been mostly used in $LiNbO_3$ and III-V semiconductors (GaAs and InP). Furthermore by using semiconductor multiple quantum well structures, a quasi-resonant electro-optic effect that is significantly enhanced over the Pockels effect can be obtained. The crosstalk performance of electro-optic switches is highly dependent on the physical device design, but many switches exhibit crosstalk better than -20 dB. Switching speed is usually only limited by the device capacitance, but in devices of sizeable optical lengths a traveling wave electrode geometry is required. Nevertheless very fast switches have been demonstrated [15, 16]. The carrier induced index change is caused by a change in the carrier concentration which, due to the band filling, bandgap shrinkage and free-carrier plasma effect, gives rise to a negative refractive index change [17]. This can be achieved by either carrier injection or depletion, depending on the sign of the required refractive index change. By using carrier injection, semiconductor optical amplifiers (SOAs) can also be used as switches by turning the gain on and off. The only drawback when using carrier injection is that switching speed is related to the carrier recombination time, which limits the device switching time to the nanosecond range [18]. However, this is still very faster when compared to some of the other switching technologies described above.

Considering the technologies listed above, it is evident that integration of passive (transparent) and active (amplifiers, modulators, and switches) devices can be more

easily accomplished in III-V semiconductor materials. In particular, InP-based semiconductors and its alloys are very attractive because they are also well suited for the fabrication of high-speed electronic devices.

1.2 InP-Based Technology

Remarkable progress has been made in InP-based devices in recent years. Despite the presence of a competing, and more mature technology that is based on GaAs and related compounds, devices employing InP-based compounds have generated much attention. The driving force behind this technology relies on the ability to fabricate high performance photonic and electronic components for telecom applications, and the potential to monolithically integrate them on a single chip.

InP is a member of the III-V family of semiconductor materials, meaning that it is a binary crystal with one element from the metallic group III of the periodic table, and one from the non-metallic group V. The family includes InP, GaAs, GaN, InSb, and InAs. Being a semiconductor, InP has an energy bandgap which is opaque for light energy higher than the bandgap, and transparent for light energy levels that are below. It also has a direct bandgap, meaning that the energy transitions of electrons that take place when a photon is absorbed or emitted do not require any change in the momentum of carriers. This direct bandgap semiconductor supports optical gain as required for lasers, and also very high absorption, making functions such as modulation or fast photo-detectors easy to implement. However, it is the existence of a family of materials (including InGaAs and InGaAsP) sharing the same 5.87 Å lattice constant as InP, thereby

6

allowing epitaxial growth of multiple layers of such materials on top of InP substrate wafers, that makes this group of materials so important. By varying the composition of the ternary and quaternary materials a precise control of the optical bandgap is achieved. The bandgap energy of an InGaAsP quaternary alloy, for example, can be varied to cover across 1.3-1.5 μm wavelengths and still be lattice-matched to InP. This bandgap tuning may be used to provide attributes such as electrical confinement to improve laser efficiency, optical confinement to provide active (gain or absorption) and passive (transparent) waveguiding functions, and the growth of thin layers that add useful properties such as quantum effects [2, 19, 20].

One of the key advantages of InP is compact device size. Because the refractive indices of InP and its ternary and quaternary derivatives are relatively higher than for other optical materials, bends can be made much sharper and smaller. Also, if the light energy is closer to the energy bandgap, electro-optical effects are stronger than in other materials (which again translates in shorter distances and lower drive voltages). The only downside of these smaller geometries is that it becomes more difficult to couple efficiently to optical fibers. However, this problem can be overcome by means of taper structures at the interfaces, to match the optical mode size at the InP chip facets with the fiber ends. The end result is the ability to fabricate very small devices with different optical functionalities.

In the electronics arena, the benefit of using InP-based material has been widely recognized for high-speed circuitry because electrons in the InGaAs ternary compound exhibit a carrier mobility in excess of 10,000 cm^2/V·s and a high saturated drift velocity

of over 2.4×10^7 cm/s [21]. InP also has a high thermal conductivity (almost 50% greater than GaAs) as well as higher electric field breakdown characteristics than GaAs [22]. Several electronic devices have been demonstrated that exploit these properties, in particular, heterojunction bipolar transistors (HBTs) and high electron mobility transistors (HEMTs) have achieved unprecedented performance relative to other competing material systems such as GaAs and SiGe. In addition to achieving speeds in excess of 200 GHz, one of the most important advantages of InP-based HBTs is a low base-emitter turn-on voltage, which minimizes the required supply voltage, which in turn reduces circuit power consumption [2, 23].

All these characteristics make InP technology ideal for high speed applications. In the telecom market, the convergence of light emitting (and receiving) technology and very high performance electronics make InP technology the most likely candidate for the development of 40 Gb/s fiber optics networks, and the clear solution for higher optical data rates.

1.3 Outline of Thesis

In this dissertation we investigate the potential application of an area selective zinc diffusion technique for the development of integrated InP photonic switches. The dissertation starts by outlining the basic properties of multiple quantum wells, as well as their electro-optic properties, which are explained in Chapter 2. Chapter 3 is dedicated to the characterization of the processes required for the fabrication of the integrated

photonic switches. In Chapter 4, the design, fabrication, and testing of several variants of Mach-Zehnder interferometric switches is explained. The ability to fabricate isolated p-n junctions allows for effective control of insertion losses in the device.

In forward-biased devices, lateral current spreading is efficiently regulated by maintaining a tight control on the zinc diffusion depth. Two photonic switches have been experimentally investigated to illustrate this effect. In Chapter 5, an optical beam steering device that operates with very low electrical current consumption is described. This beam steering device is then used to develop an efficient 1x3 photonic switch. Chapter 6 deals with the use of multimode interference (MMI) structures as a platform to develop active photonic devices. Since the device relies on the selective perturbation of the optical properties within the multimode waveguide, current spreading control is a key factor for the operation of the devices. Several novel MMI based devices are proposed and demonstrated. Finally, Chapter 7 closes the dissertation with some conclusions.

CHAPTER TWO: OPTICAL AND ELECTRO-OPTICAL PROPERTIES OF MULTIPLE QUANTUM WELLS

Optical switching and modulation of light is generally performed by modulating the refractive index or optical absorption coefficient of key sections of the devices. In fact, these two physical parameters are not independent but are related to each other by the well known Kramers-Kronig relations [24]. In semiconductor waveguide devices, the index of refraction or the absorption can be varied by making use of several fundamental electro-optical effects. In addition, the ability to grow sophisticated layered semiconductor structures has opened offers many new opportunities in semiconductor physics and devices. One type of layered structure that has attracted a great deal of interest is the semiconductor multiple quantum wells (MQW). As a consequence of quantum confined effects, a significant change can be observed in their linear optical properties, as compared to bulk semiconductors. The relatively smooth absorption spectrum of bulk semiconductors is broken into a distinctive structure that directly reflects the effects of quantum confinement, and enhancement of the excitonic interactions. The electro-optic response of these structures at wavelengths within the range of the exciton peaks is very different from the Pockel's electro-optic effect, owing to the quantum confined Stark effect (QCSE). In this chapter, we describe some of the

important physical mechanism that impact the optical properties of semiconductor quantum wells. Electro-optical properties are emphasized primarily on the QCSE and carrier induced effects, because they provide the largest refractive index changes.

2.1 Quantum Well Structure

A semiconductor quantum well (QW) is an extremely thin layer of narrow bandgap material that is sandwiched between two layers of material with a larger bandgap, so that mobile carriers are trapped inside the resultant potential well. This is schematically shown in Fig. 2.1, where the well and barrier are formed by InGaAs and InP materials respectively. When the physical dimensions of the well are comparable to the characteristic lengths of a particle, in this case the Bohr radius of the carrier, the carriers are only free to move in the quantum well material along the plane of the layers. However, their motion in the z-direction perpendicular the layers is restricted and quantum confined size effects occur (quantization of the carrier's energy) in one of its three degrees of freedom. The energy is then restricted to certain allowed, or quantized, values just like the discrete modes of vibration of a clamped string. These quantum states can be described by solving the Schrödinger equation

$$\frac{-h^2}{2m^*}\frac{\partial^2 \phi_n}{\partial z^2} + V(z)\phi_n = E_n \phi_n, \tag{2.1}$$

where $V(z)$ is the potential energy (i.e. the quantum well potential) seen by the particle, m^* is the particle's effective mass (electron or hole), and E_n and ϕ_n are the eigen-energy and eigen-function associated with the nth solution to the equation [25-27].

11
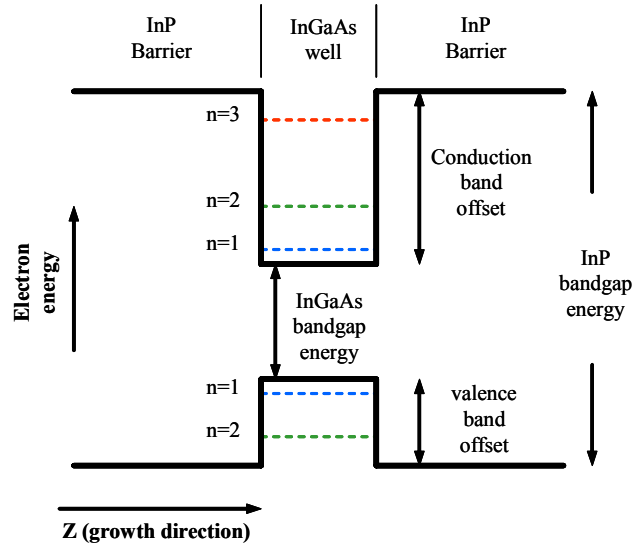
Figure 2.1 Schematic of a quantum well showing discrete energy states.

The simplest solution to Eq. 3.1 corresponds to the case of very high walls, or infinite well, in which the wavefunction must be zero at the walls of the quantum well. In this case, the wavefunctions are sinusoidal and for the associated energies we have

$$E_n = \frac{-\hbar^2}{2m^*} \left[\frac{n\pi}{L_z} \right]^2 \quad n = 1,2,...., \tag{2.2}$$

where n is a quantum number and L_z is the thickness of the well. The allowed energy levels are then spaced quadratically with increasing n, which is also shown in Fig. 2.1. The spacing is also inversely proportional to the effective mass, which is different for electron and holes. This gives rise to a "ladder" of confined states for both electron and holes. Although this situation applies quite well to the simple conduction band, for the valence band is more complicated. The quantum confinement lifts the degeneracy at the

12

zone center between light holes and heavy holes, resulting in two ladders of confined hole states.

In an actual quantum well, the walls are not infinitely high. There is in fact a specific band offset between the well and barrier. The fact that the walls are only of finite high means that the wavefunction penetrates in the barriers as an exponentially decaying function. For practical applications, multiple quantum wells are usually grown one after the other in a multi-layered structure. In those cases, the same physics applies provided that the barrier layers (walls) are thick enough to prevent coupling of the wavefunctions in adjacent quantum wells.

2.2 Optical Properties of Multiple Quantum Wells

The quantization of the electron and hole energies along the z-direction leads to step-like density of states in the conduction band and valence band and this phenomenon is easily seen in an optical absorption spectrum as shown in Fig. 2.2. We can clearly see a series of steps rather than the parabolic shape of the absorption spectrum usual for normal bulk semiconductor. The energy at which each step starts corresponds to each of the allowed transitions between quantized electron and hole states. The absorption spectrum is modified further by the existence of strong exciton absorption peaks at the edges of the steps [28]. In bulk semiconductors the excitons are usually screened by free carrier scattering and phonon scattering, especially at room temperature, and therefore bulk semiconductors do not usually exhibit excitonic absorption peaks at room temperature.

In quantum well structures, with an average well width of about 100 Å, the excitons are confined within the quantum well layer. This squeezes the exciton in one direction giving a larger binding energy than in bulk materials. Since the strength of an optical transition is generally proportional to the overlap of electron and hole, therefore a strong exciton absorption peak is observed. This effect is large enough that they can be clearly seen at room temperature. Many interesting effects are related with these exciton peaks [26, 29]. However, in this work we are only concerned with the electro-optical properties of MQW.
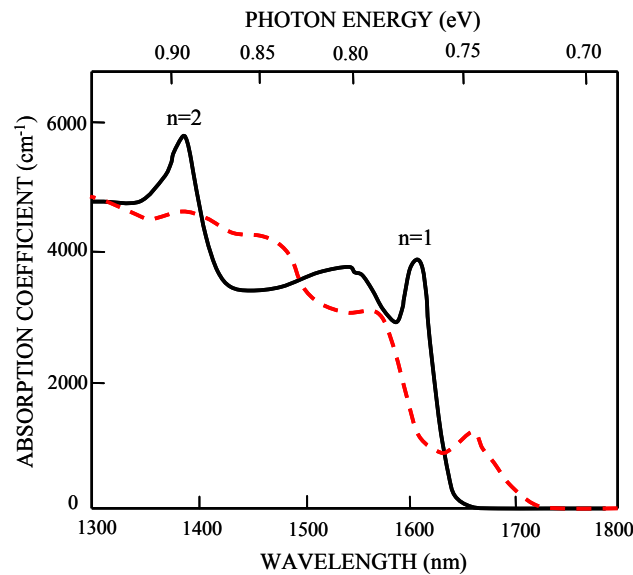
Figure 2.2 Absorption spectra of an InGaAs/InP MQW at room temperature measured at 0 V (solid line) and 30 V (dashed line) (After [26]).

2.3 Quantum Confined Stark Effect

The QCSE describes the change in the optical properties of the MQW when an electric field is applied perpendicular to the QW layers. The applied electric field tilts the

bands and causes the eigen-level for electrons to be lowered and the equivalent eigen-level for holes to be raised. The energy for the transition between these eigen-levels is consequently reduced. The principal effect in the absorption spectrum is that the steep optical absorption edge is shifted to lower energies by the application of the electric field without destroying the sharp exciton absorption peaks, as shown in Fig 2.2. This is totally different compared with the behavior of bulk material, where even with moderate fields the exciton peaks are destroyed and the remaining absorption change correspond to a broadening of the absorption edge due to photon-assisted tunneling, the so-called Franz-Keldysh effect [30]. The reason for the persistence of the exciton peaks is that the walls of the QW prevent the field ionization of the exciton. The electrons and holes are pulled to the opposites walls of the QW by the field, but they do not tunnel rapidly through these walls. The tunneling time of the individual electrons and holes is usually much longer than 1 ps and, therefore, has little effect on the exciton which is destroyed in ~ 400 fs at room temperature by phonon ionization. On the other hand, the absorption does become somewhat weaker as it shifts to lower energies because the electron/hole overlap is reduced by the electron and hole being pulled apart. Because the exciton peak is preserved we should expect a large refractive index change, or electro-refraction, if we apply the Kramers-Kronig transform on the absorption change. Both theoretical and experimental work have been done to characterize the refractive index change due to the QCSE and they show that index changes of one to two orders of magnitude larger than in bulk materials can be obtained [31-34].

Inherently some absorption losses need to be tolerated in order to access this enhanced refractive index change because the large electro-refraction is obtained in the wavelength region close to the n=1 exciton transition. For interferometric switches optical losses can adversely affect the device performance significantly. It is therefore critical that the wavelength of the exciton transition be positioned appropriately with respect to the operating wavelength range. A design criterion for integrated switches is that a detuning of 100 nm (or bigger) between the bandgap and the operating wavelength is usually enough to reduce insertion losses due to intrinsic absorption. In the case of InGaAs QW the exciton transition energies can only be tuned by varying the width of the QW layer. For operation at 1.55 μm wavelength, an InGaAs QW thickness of 8 nm can be used to obtain an exciton peak at 1.41 μm. However, it is known that the quantum confined Stark shift of the exciton is roughly proportional to the forth power of the quantum well width $\left(\Delta \xi \propto L_w^4 \right)$ and hence a wider QW would be advantageous because a larger shift of the absorption spectrum also translates into a larger index change [35]. Therefore it would be beneficial to use a material that allows us to have wider QW while maintaining the large detuning. On the other hand if a structure with very wide quantum wells is used the exciton tends to ionize and dissociate with very small applied fields and the quadratic electro-optic effect is drastically reduced. In general a quantum well width of 10nm appears to be an optimum compromise. By using quaternary QW formed from the alloy $In_x Ga_{1-x} As_y P_{1-y}$ we have an additional degree of freedom in that a combination of

16

composition and well thickness can be used to adjust the wavelength of the exciton transition. This is an important advantage for QW devices which utilize the QCSE and allows us to design a structure with our desired quantum well width.
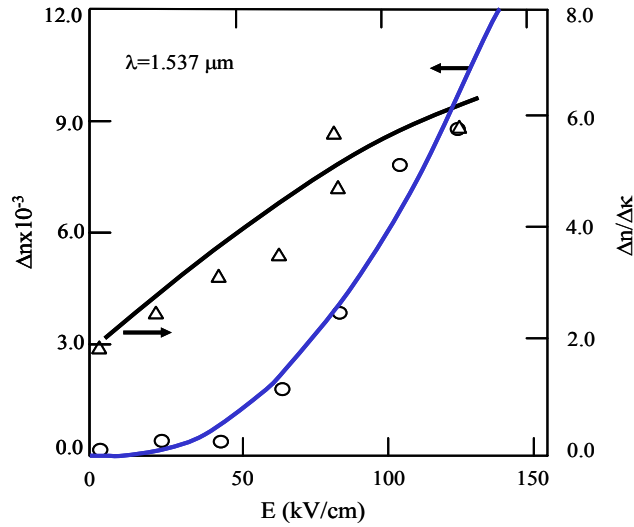
Figure 2.3 Change in refractive index Δn and figure of merit $\Delta n/\Delta k$ as a function of applied field (After [32]).

The change in refractive index (Δn) for ten periods of 85 Å InP barriers and 85 Å InGaAsP wells at different applied voltages is shown in Fig. 2.3 [34]. The ratio $\Delta n/\Delta k$, a useful figure of merit for phase modulator, is also shown in Fig. 2(b). In this ratio Δn and Δk are the real and imaginary parts of the complex refractive index change, respectively. For efficient phase modulation with low loss, a large $\Delta n/\Delta k$ ratio is required. From Fig. 2(b) we can see that large Δn and $\Delta n/\Delta k$ values are easily obtained for quaternary

InGaAsP wells. Because of this efficient electro-refraction, the wafer used in our work uses quaternary InGaAsP not only in the wells, but also for the barriers because this affords us the freedom to control the barrier height.

2.4 Carrier Induced Effects in Semiconductors

When carriers are injected into a semiconductor, either by optical excitation or electrical current injection, a change in the absorption spectrum of the material is observed. This change can be a result of different effects taking place in the semiconductor, such as the free-carrier absorption (plasma effect), band filling, and band-gap shrinkage effect (band-gap renormalization). As previously mentioned, a change in absorption is directly related to a refractive index change by direct application of the Kramers-Kronig relations. Although the relative contribution of each effect that is directly related to the injected current density is bound to be different, the refractive index change Δn is generally negative for wavelengths in the transparent region. In the following, the physical background of these effects is described together with the theoretical basis from which the combined effect on Δn can be estimated.

2.4.1 The Plasma Effect

When free carriers are present in a semiconductor, the effect is to lower the refractive index with respect to its intrinsic value. This refractive index change is a result

of intraband free carrier absorption, and has been modeled in its simple form using the
Drude model. The corresponding change in refractive index is given by [17, 36]

$$\Delta n = -\left(\frac{e^2 \lambda^2}{8\pi^2 c^2 \varepsilon_0 n}\right)\left(\frac{N}{m_e}+\frac{P}{m_h}\right), \tag{2.3}$$

where λ is the photon wavelength, n is the intrinsic semiconductor refractive index, c is
the speed of light in free space, ε_0 is the permittivity, m_e and m_h are the electron and
hole effective masses, and N and P are the electron and hole carrier densities respectively.
According to this model the sign of the plasma effect is always negative and isotropic,
regardless of the photon wavelength, and is directly proportional to the carrier
concentration. Shown in Fig. 2.4 is the refractive index change due to the plasma effect as
calculated from Eq. 2.3 for InGaAsP (E_g=1.08 eV) bulk semiconductor with equal
concentration of electrons and holes (N=P). The data used for this calculation is shown in
Table. 2.1 [17].
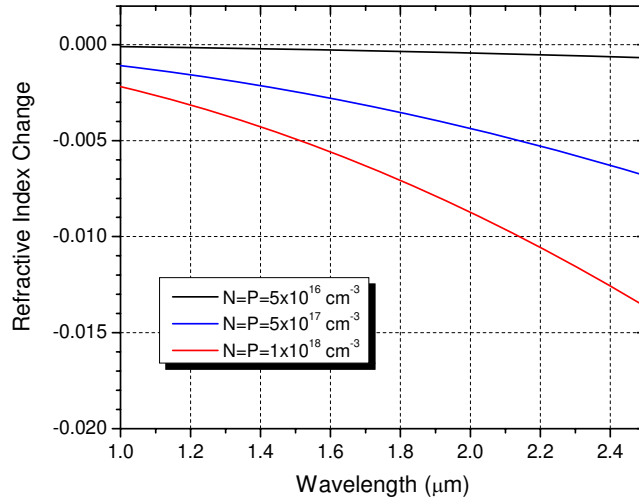
Figure 2.4 Calculated refractive index change from the plasma effect as a function of
wavelength for InGaAsP (E_g=1.08 eV) for different carrier densities.

Table 2.1 Values of semiconductor parameters for InGaAsP (E_g=1.08 eV).

InGaAsP parameters (T=300 K)	
E_g (eV)	1.08
n	3.6
ε	13.0
m_e (m_0)	0.064
m_{hh} (m_0)	0.51
m_{lh} (m_0)	0.086

We can see that carrier concentrations on the order of 1×10^{18} cm^{-3} are required to achieve a significant refractive index change. This is close to the upper limit in carrier concentration, since an even higher carrier concentration will give rise to bandgap renormalization effects, which has an opposite refractive index change.

2.4.2 The Band Filling Effect

When carriers (electrons and holes) are electrically injected into a semiconductor, the lowest states of the conduction band become very quickly occupied with electrons while the top of the valence band is quickly populated with holes. As the bottoms of the conduction band gets filled up, electrons from the valence band require energies greater than the nominal bandgap to be optically excited to the conduction band. A similar behavior is observed when the doping level of a semiconductor is increased, and is known as the Burnstein-Moss effect [30, 37]. The resulting effect is a blue shift of the absorption spectrum, which is also correlated to a refractive index change through the

20

Kramers-Kronig relations [38]. This effect is modeled by first obtaining the change in absorption due to carrier injection,

$$\Delta\alpha(N,P,E) = \alpha(N,P,E) - \alpha_0(E),$$ (2.4)

where $\alpha_0(E)$ is the intrinsic optical absorption and $\alpha(N,P,E)$ is the modified optical absorption. Once the carrier induced absorption change is calculated, the refractive index change is obtained using

$$\Delta n(N,P,E) = \frac{2c\hbar}{e^2} \oint_{0\to\infty} \frac{\Delta\alpha(N,P,E')}{E'^2 - E^2} dE.$$ (2.5)

The refractive index change is estimated following the model proposed by Bennet *et al.* [17]. For bulk InGaAsP (E_g=1.08 eV) a square root dependence on the optical absorption is assumed as suggested in [17].
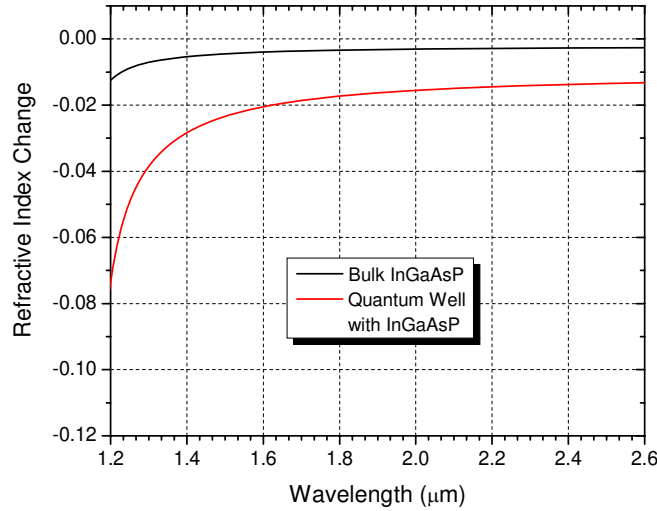
Figure 2.5 Calculated refractive index change from the band filling effect as a function of wavelength for bulk and quantum well InGaAsP (E_g=1.08 eV) for a carrier density of 5×10^{17} cm^{-3}.

In order to observe the changes introduced when the material is used as a QW, the optical absorption is modified using a staircase-like dependence on the optical absorption. The values of the quantized energy levels are calculated for the same InGaAsP semiconductor material with a thickness of 10 nm. The results are shown in Fig. 2.5 for the same value of carrier density. As can be observed, a negative refractive index change is induced for wavelengths around the transparent region of the semiconductor. The value also increases significantly as we get closer to the bandgap. An increase on the refractive index change is also observed by moving from bulk to QW. This is related to the smaller 2-D density of states, such that a larger change in refractive index is observed for the same carrier density.

2.4.3 The Bandgap Shrinkage Effect

The bandgap shrinkage effect, also know as bandgap renormalization, is significant only when the concentration is large enough, which is typically the case in semiconductor lasers. As the concentration increases, the interaction between electrons (or holes) is also increased due to the overlapping of the wavefunctions. When the average spacing of the impurity atoms approaches the approximate Bohr radius of 100 Å, due to heavy doping, the potential seen by each impurity electron (hole) is affected by the neighboring impurity atoms and impurity bands formed. The effect is similar to the formation of energy bands in a semiconductor as the lattice atoms are brought closer to

22

each other. The net effect is a narrowing of the semiconductor bandgap. Typically a carrier concentration higher than 5×10^{18} cm^{-3} is needed for the effect to become significant [39, 40]. Although there are some discrepancies on this threshold concentration, in general as the concentration is lowered the effect is minimized. Since our work is related to phase modulation, the carrier density is very low and bandgap shrinkage should be negligible.

Throughout this dissertation we will make use of both the QCSE and carrier induced effects. The choice will be highly dependent to the particular device and application.

CHAPTER THREE: MATERIAL CHARACTERIZATION

The development of optoelectronic devices involves many different fabrication steps and the choice of steps depends on the complexity of the device. In order to obtain consistent results, each step needs to be fully characterized before being implemented in the final device fabrication process. In this chapter we describe the wafer structure used in our work, as well as the relevant fabrication processes. These include the wet and dry etching of InP-based materials, the characterization of the zinc in-diffusion technique to selectively modify the electrical characteristics of the semiconductor, and the fabrication of ohmic contacts that are required for electrical bias to be applied to the devices. These processing methodologies have allowed us to fabricate a variety of devices with different functionalities.

3.1 Wafer Structure

The wafer structure used in this dissertation is shown in Fig. 3.1 (a). It was grown by metal organic chemical vapor deposition (MOCVD) on an n^+ InP substrate with a doping concentration of 3×10^{18} cm^{-3}. The whole epitaxial structure was doped n-type at 2×10^{17} cm^{-3} except for the MQW core region that was nominally undoped. The first layer was a 1 μm thick InP buffer layer, followed by the MQW region that was clad by a

1.6 µm thick InP top layer which was in turn capped by a 0.1 µm thick InGaAs layer. As explained earlier, a quantum well thickness of ~10 nm has been found to be ideal for electro-optic applications. Therefore, in our wafer the undoped MQW guiding layer consisted of 14 pairs of 100 Å thick InGaAsP (E_g = 0.816 eV) quantum wells and 100 Å thick InGaAsP (E_g = 1.08 eV) barriers. We also included a 10 nm thick InGaAsP (E_g = 1.08 eV) etch stop layer located 190 nm above the MQW to allow precise control of the InP etching during the waveguide fabrication. The position of this etching stop is calculated from the directional coupler requirements, and will be explained in more detail in chapter 4. The quantum well width and composition is selected such that an effective bandgap of 0.855eV (1.45µm) could be obtained as confirmed by the room temperature photoluminescence (PL) spectrum shown in Fig. 3.1 (b). This is designed to provide a 100 nm detuning from the operating wavelength at 1.55 µm, so as to minimize material absorption losses.
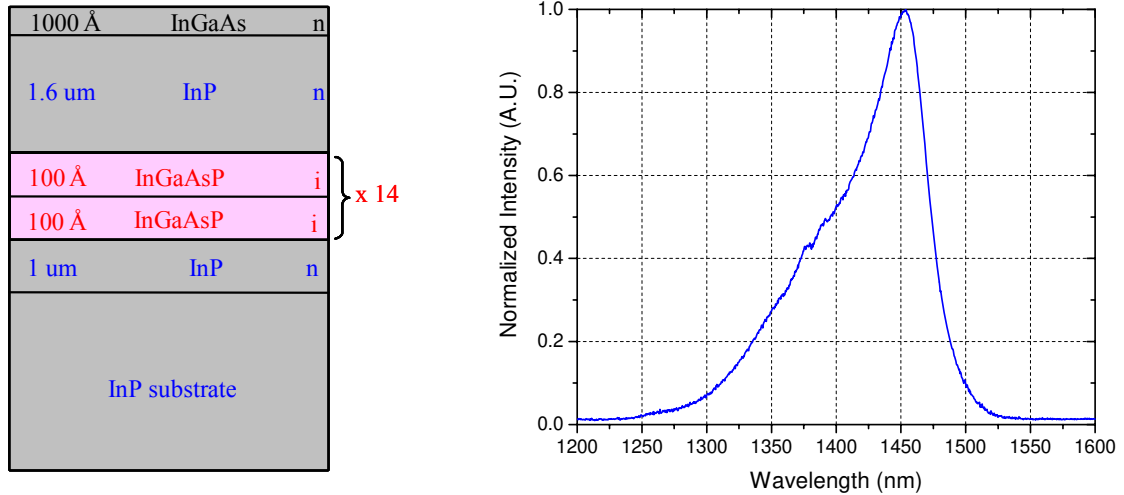
Figure 3.1 Wafer structure (left) and room temperature PL spectra (right) of the wafer.

3.2 Dielectric Films

Dielectric films made of silicon dioxide (SiO_2) and silicon nitride (Si_3N_4) are widely used for different applications in the micro-fabrication of electronic, optoelectronic and optical devices. They are used as etching masks, diffusion masks, impurity doping, and as passivation layers. The deposition and etching of these films have previously been characterized in our group, However the Si_3N_4 processing was slightly modified in order to work properly as a diffusion mask. In the following we give a brief description of the deposition and etching conditions used for each film.

3.2.1 Deposition of SiO_2 and Si_3N_4

A very reliable method for depositing dielectric films is the use of a controlled reacting chamber [41]. There are several methods of chemical vapor depositions such as atmospheric pressure (APCVD), photo-CVD, low pressure chemical vapor deposition (LPCVD), and plasma enhanced (PECVD) [42]. Among them, PECVD is highly attractive since the plasma formation allows for deposition at relatively low temperatures (250-300 °C), which is important for InP-based semiconductors. In our experiments, we used a dual chamber Plasma Therm 790 PECVD system, with one of the chambers fully dedicated for PECVD deposition. In this system, the plasma is generated by a radio-frequency (RF) voltage applied between two parallel plates at 13.56 MHz. This RF power causes electrons in the processing gases to oscillate and collide with gas molecules,

leading to a sustained plasma. The plasma can produce a large number of active species (radicals, atoms, ions, and excited species) that are readily available to interact with the exposed sample surface. Depending on the chemistry used, the reactions with the sample can be used for either deposition or etching. The processing gases used for the deposition of the films in this work were nitrogen (N_2), ammonia (NH_3), nitrous oxide (N_2O), and 2% silane (SiH_4) diluted in N_2. The processing conditions for both films are shown in Table 3.1.

Table 3.1 Deposition parameters for silicon nitride and silicon dioxide.

Parameters	Si_3N_4	SiO_2
SiH_4 (sccm)	120	400
N_2O (sccm)	----	827
NH_3 (sccm)	450	----
N_2 (sccm)	400	----
RF Power (W)	20	25
Pressure (mTorr)	900	1050
Temperature (°C)	250	250
Deposition Rate (nm/min)	10	50

The deposition rates are also shown in Table 3.1 and they are highly consistent as long as the parameters are kept constant. The Si_3N_4 film grown in this way remained in good condition after a high temperature process at 500 °C for as long as one hour. The SiO_2 can be processed at even higher temperatures.

3.2.2 Etching of SiO$_2$ and Si$_3$N$_4$

Etching of SiO$_2$ and Si$_3$N$_4$ can be accomplished by wet or dry etching methods. Dry etching is sometimes preferred because it is a clean process that is highly reproducible, and it can also be tailored to achieve a specific etching profile. Our dry etching process was carried out by reactive ion etching (RIE) using the second chamber of the Plasma Therm 790 PECVD system. During RIE, gaseous species from the plasma react with the surface atoms forming compounds or molecules. These species then leave the surface thermally, or as a result of ion bombardment. In our experiments, carbon tetrafluoride (CF$_4$) with 8% of oxygen was used as the processing gas. In principle, this fluorine based etching tends to be purely chemical. However, it is well know that lowering the chamber partial pressure (< 100 mTorr) provides a more dominant physical etching [42]. The reason is that the free mean path of ions and radicals is increased, thus allowing them to arrive at a right angle to the surface of the sample. This ion bombardment is very useful to maintain the directionality, or anisotropy, of the etching process. There are a number of ways in which the ion bombardment may be helping the etch process. For example, it may clean the surface allowing the reaction to occur more readily, and/or it may stimulate the reaction itself, and/or it may help de-sorb or de-trap the by-product molecule. The etching conditions used in our processes are shown in Table 3.2.

All the etching was carried out at room temperature. It can be observed that the etching rate of SiO$_2$ is much slower than that of Si$_3$N$_4$, even when the pressure and RF

power is increased. Although this means a more isotropic etching, we typically etch SiO_2

films on the order of 200 nm and therefore this has not been a serious issue.

Table 3.2 Dry Etching parameters for silicon nitride and silicon dioxide.

Parameters	Si_3N_4	SiO_2
CF_4 (sccm)	12	45
O_2 (sccm)	1	----
RF Power (W)	100	175
Pressure (mTorr)	75	300
Etching Rate (nm/min)	125	22

3.3 Etching of InP based materials

The etching of semiconductor materials is a critical step for the processing of

semiconductor optoelectronic devices. There are in general two types of etching: wet

etching and dry etching. Various kinds of etchants are ordinarily used for wet etching of

InP material, such as hydrochloric acid (HCl), hydrobromic acid (HBr), and Nitric acid

(HNO_3). The advantage of wet etching is that there is no physical damage and the defect

density is low because it is a relatively gentle chemical process. Dry etching process such

as reactive ion etching usually involves a combination of chemical and physical etching

mechanisms [2]. The advantage of the dry process is that the etching can be very

anisotropic, is usually highly reproducible, and is well suited for etching small features.

The main drawback is that this process produces physical damage due to the ion

bombardment that can affect the conductivity of the semiconductor. Typically a mild wet etching following the dry etching process is used to remove the affected areas. In the end, both processes can be used individually or combined depending on the specific application.

3.3.1 Wet Chemical Etching of InP

The simplest mode of chemical etching entails the dissolution of the material in a liquid reagent. In III-V compound semiconductors this involves an oxidation-reduction process with the formation of complex ions or molecules that are soluble in the etching medium. For this purpose, various acidic solutions have been successfully used for etching InP-based materials [43]. However, we are most interested in those solutions that etch preferentially InP but not its ternary InGaAs and quaternary InGaAsP compounds. This etch selectivity is achieved using HCl and HBr based solutions [43, 44]. These etchants exhibit a reaction-rate limited process, with an anisotropic or orientation dependent etching. Orientation effects have been attributed to crystallographic properties, particularly the density of surface-free bonds, with the relative etch rate increasing with the number of available free bonds. InP compound semiconductor crystallizes in the zinc-blende structure, meaning that the structure consists of two interpenetrating face centered cubic sublattices; with each sublattice containing one kind of atom. For device applications, most InP wafers are grown on the (001) surface because cleaving of {110}

surfaces are perpendicular to {001} surfaces and also to {110} surfaces themselves. This means that there are two different types of {111} surfaces that may appear upon chemical etching [2]. The outermost atom layer in each surface consists of either In or P atoms that are triple bonded to the lattice. Therefore, on the {111} surface, In atoms have no spare electrons, while on the {111} surface, P atoms have two electrons per atom available to take part in a chemical reaction. As a result, the P{111} planes are highly reactive compared to the In{111}. Although wet etching of InP have been widely investigated, the dissolution process is very complex and wet etching profiles are still difficult to predict and are highly dependent on the etching conditions. The final etching rate and shape of the etched pattern depends on the combinations of semiconductor material, mask, and etchants, and is highly dependent on the orientations in the semiconductor [45].

3.3.1.1 HBr Based Etching.

As previously explained, wet etching profiles are also dependent on the masking material. Owing to the harsh acidic nature of InP etchants, most masking materials such as photoresists and oxide films cannot survive the exposure required to etch about one µm of InP. However, InGaAs is totally resistant to InP etchants. Therefore, in order to achieve consistent results, the top 100 nm InGaAs layer was used as the mask for etching the InP cladding. In order to do this, the InGaAs has to be etched selectively from the InP. This can be easily achieved using a phosphoric acid (H_3PO_4) : hydrogen peroxide

31

(H_2O_2) : deionized water (H_2O) etching solution, see Table 3.3. The recipe shown in Table 3.3 etches InGaAs at a highly controllable rate of 125 nm/min, but the etchant is not suitable for etching InGaAsP because the process is too slow. By using sulfuric acid (H_2SO_4) instead of H_3PO_4 the etching rate of InGaAsP can be significantly increased to 135 nm/min, and still retain a high etch selectivity with InP.

The etching rates of InP and profiles in HBr solutions were characterized to determine whether the etchant was well suited for waveguide fabrication. This was done by etching waveguides along the [110] and [$\bar{1}10$] directions, and further cleaving perpendicular to the waveguide direction. In this case, HBr acid was diluted with deionized (DI) water, and the etch rates were measured for both n-type and p-type (Zn diffused) InP, see Table 3.4. A good etching rate was obtained and can easily be reduced further by increasing the DI water content. We also notice that there is a difference in the etching rate of n-type and p-type InP. This is a well known effect for HBr, and is actually used for delineation of doping profiles in semiconductor.

Table 3.3 Wet chemical etching parameters for InGaAs and InGaAsP.

Etching Solution				Etching Rate (nm/min)	
H_3PO_4	H_2SO_4	H_2O_2	H_2O	InGaAs	InGaAsP
1	----	1	30	125	15
----	1	1	10	----	135

Table 3.4 Wet chemical etching parameters for InP in HBr based solution.

Etching Solution		InP Etching Rate (nm/min)	
HBr	H$_2$O	n-type	p-type
2	1	700	400
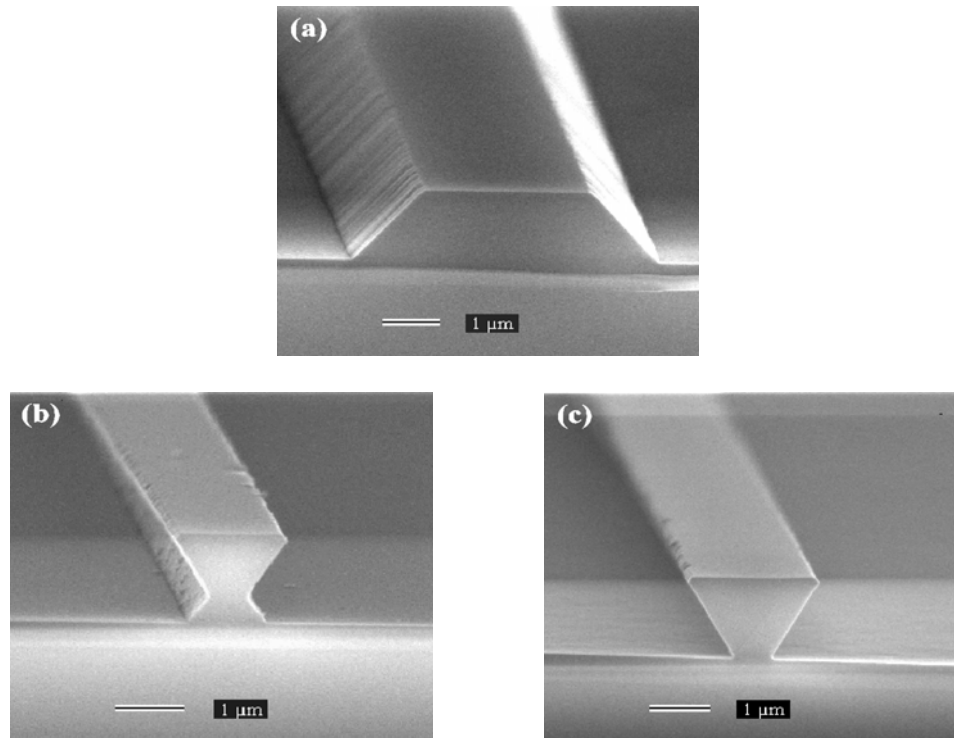
Figure 3.2 HBr based InP wet etching profiles (a) Waveguide along the [$\overline{1}$10] direction, (b) Waveguide along the [110] direction, and (c) Over-etched waveguide along [110] direction.

Scanning electron microscopy (SEM) was used to observe in detail the etching profiles and these are shown in Fig. 3.2. The etching profiles for waveguides along the

$[\overline{1}10]$ direction (Fig. 3.2a) reveals a positive slope with a 45° angle with respect to the

(001) surface. According to the published literature [43] this corresponds to the In$\{0\overline{1}1\}$ crystallographic planes. For waveguides along the [110] direction, the profile is more complicated as shown in Fig. 3.2 (b). From the corresponding angle of the negative slopes (125°) they should correspond to the In$\{\overline{1}\overline{1}1\}$ planes. A rounded bottom should be expected in this case, but this is not observed because of the presence of an etch-stop layer. If the sample is slightly over-etched, a nice reverse mesa is obtained as shown in Fig. 3.2 (c).

3.3.1.2 HCl Based Etching.

InP etching using concentrated HCl is extremely fast and is usually accompanied by the formation of micro-bubbles that affect the uniformity of the etching. Etching rate can be easily reduced by diluting with DI water. However, reduction of micro-bubbling has been attempted by diluting the HCl acid with acetic (CH_3CO_2H) or lactic acid ($CH_3CHOHCO_2H$) [44]. The etching rates of various HCl based solutions are displayed in Table 3.5. The solution using acetic acid produced a minimum amount of micro-bubbles, while maintaining a good and controllable etching rate. With lactic acid, a noticeable reduction in micro-bubbling could only be observed when large amounts of lactic acid were used which also led to a significant reduction in the etching rate. The mixtures shown in Table 3.5 were a good compromise between etching rates and micro-

34

bubble formation. Another difference between the etchant solutions is that the acetic based ones readily attack regular photoresists while the lactic based ones are milder acting on photoresists. Different etching rates are also observed for n-type and p-type InP. As we will discuss later this can be a problem, for certain specific applications.

Table 3.5 Wet chemical etching parameters for InP in HCl based solution.

Etching Solution					InP Etching Rate (nm/min)	
HCl	CH_3CO_2H	H_2O	H_3PO_4	$CH_3CHOHCO_2H$	n-type	p-type
1	6	----	----	----	1125	825
1	6	1	----	----	80	----
2	----	----	5	2	395	240

The etching profile for waveguides fabricated along the $[1\bar{1}0]$ direction is shown in Fig.3.3 (a). A similar profile as that achieved with the HBr solution was obtained. However, the angle of the planes is estimated to be 35° which is correlated with the $\{1\bar{1}\bar{2}\}$ planes. Fig. 3.3 (b) shows the profile for waveguides along the [110] direction. In this case, the etched plane is almost perpendicular to the (001) surface, which corresponds to the $\{1\bar{1}0\}$ planes. It is clear that this is very useful profile, since it resembles a perfect ridge waveguide, thus facilitating numerical simulations.

35
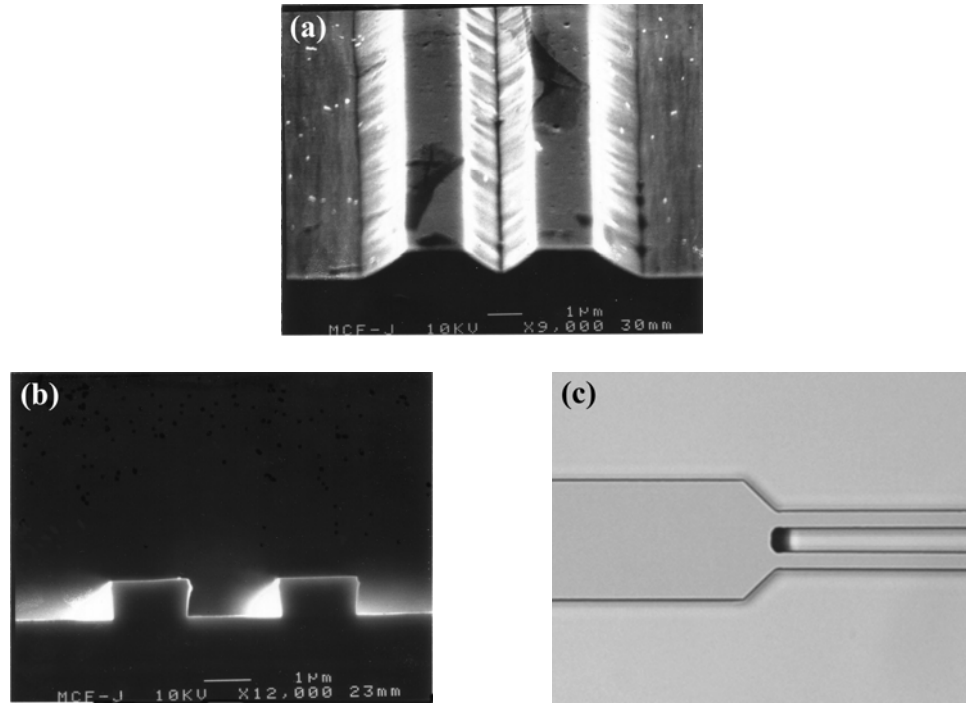
Figure 3.3 HCl based InP wet etching profiles (a) Waveguide along the $[\bar{1}10]$ direction, (b) Waveguide along the [110] direction, and (c) Top view of an etched structure with etched features along both crystal directions.

So far we have observed structures etched along either crystallographic direction. When a corner is etched, the effects of this crystallographic dependent etching are reflected in the resulting shape, as shown in Fig. 3.3 (c). The picture is a top view of a multimode waveguide with two output waveguides. We can see that the corner is etched at 45° instead of a 90° angle that was on the original mask design. This effect can be avoided by using RIE, and will be explained in the next section. Nevertheless, based on these results, waveguides oriented along the [110] direction were fabricated by wet etching using the HCl based solutions.

3.3.2 Dry Etching of InP

The main advantage of RIE is primarily the possibility of anisotropic etching. The RIE etching process for InP was performed at the University of California, San Diego, using an inductively coupled plasma RIE system (ICP/RIE) from Trion Technologies with methane and hydrogen as the active reagents. The advantage of ICP/RIE is that the plasma is generated via the magnetic field resulting from inductive coupling, which allows high density plasmas to be formed even at low pressures. This is very important because it provides good control of the anisotropy of the etching. The processing parameters are shown in Table 3.6. All the processing was done at a substrate temperature of 60 °C, which resulted in an etching rate of 230 nm/min. The dry etching profile is shown in Fig. 3.4 (a), and is found to be independent of crystallographic orientation. This is confirmed by etching the same multimode waveguide structure that was shown in fig. 3.3 (c) for the case of wet etching. As shown in Fig. 3.4 (b), the structure is transferred much more accurately to the InP as a result of the anisotropic etching. This is a critical step when fabricating more complex waveguiding structures.

Table 3.6 Dry Etching parameters for InP.

ICP/RIE Parameters					
Pressure (mTorr)	H_2 (sccm)	CH_4 (sccm)	ICP power (W)	RIE power (W)	Etch Rate (nm/min)
10	8	22	200	100	230
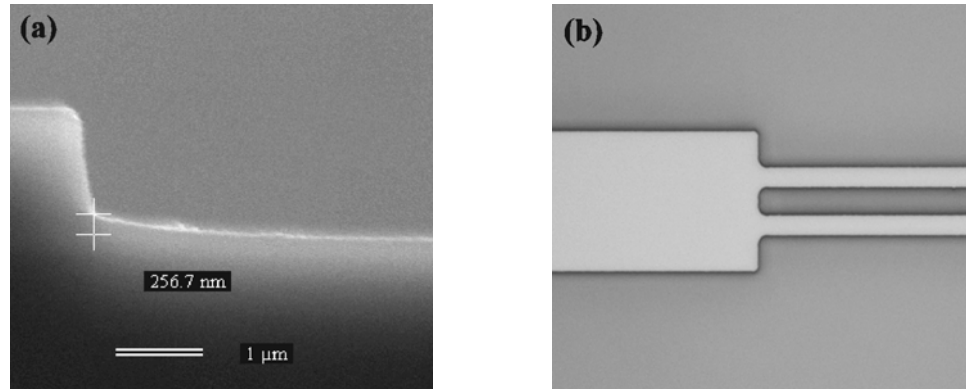
Figure 3.4 ICP/RIE InP etching (a) SEM of etching profile, and (b) Top view of an etched structure with etched features along both $[1\bar{1}0]$ and $[110]$ crystal directions.

3.4 Zinc In-Diffusion in InP

The fabrication of integrated optoelectronic devices relies on the ability to incorporate predetermined amounts of impurity dopants into precisely defined regions of a chip. This allows the formation of layers with controlled electrical properties on III-V semiconductors. The most common technologies used to modify the electrical properties in semiconductors are ion implantation and diffusion [46]. Diffusion has been the primary method of introducing impurities because is a very simple and economical process. The most common p-type diffusants for III-V compound semiconductors are zinc and cadmium. Zinc atoms occupy substitutional group III sites, behaving as acceptors and, thus, producing p-type electrical properties. Since zinc diffuses one to two orders of magnitude faster than cadmium, it is the preferred diffusant for the realization of deep p-n junctions.

38

The diffusion of Zn in InP has been extensively investigated, and it is generally accepted that the diffusion mechanism is governed by an interstitial-substitutional mechanism [47-49]. The Zn diffusion process in InP is believed to be dominated by the highly mobile Zn interstitials in chemical equilibrium with the substitutional Zn. The overall amount of the interstitial Zn is assumed negligible in comparison to the substitutional Zn. These fast diffusing Zn interstitials transport Zn atoms from high to low concentrations regions and then convert into substitutional or neutral Zn through chemical reactions with In vacancies [50], with In lattice atoms [51], or with phosphorus vacancies [48]. This diffusion mechanism leads to a concentration dependent diffusion process. The one-dimensional Zn diffusion process is therefore modeled by the diffusion equation with a concentration dependent diffusion coefficient [52],

$$\frac{\partial C_s}{\partial t} = \frac{\partial}{\partial x}\left(D_{eff}\frac{\partial C_s}{\partial x}\right),$$ (3.1)

where C_s is the concentration of substitutional ions, and D_{eff} is the concentration dependent diffusion coefficient,

$$D_{eff} = D_0 C_s^n,$$ (3.2)

with D_0 being a diffusion constant.

The equation can be solved for the case of constant surface concentration and a semi-infinite medium. Shown in Fig. 3.5 are the normalized diffusion profiles obtained from Eq. 3.1 for the cases of $n = 0, 1, 2, and \ 3$, with the depth axis normalized to $n = 1$. The case of $n=0$ corresponds to the typical complementary error function solution that is

obtained for a constant diffusion coefficient. The main feature in Fig. 3.5 is that the concentration dependent diffusion profiles exhibit a sharper diffusion front when compared to the constant diffusion case. In fact, the diffusion front turns out to be steeper as the power dependence of the diffusion coefficient is increased. This is a highly desirable profile since a sharper junction can be easily obtained. Therefore, a square or cubic dependence on the diffusion coefficient would be beneficial in our devices in order to avoid free-carrier absorption.
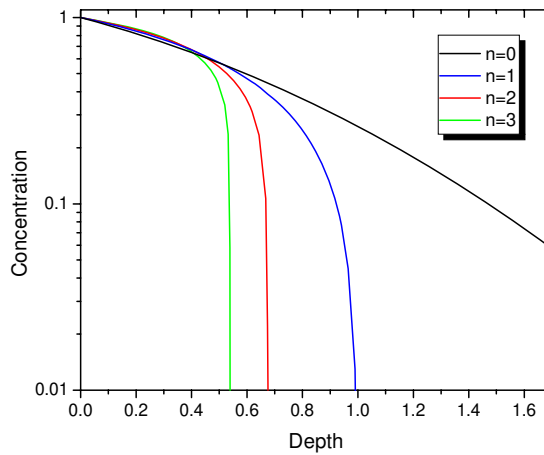
Figure 3.5 Zinc diffusion profiles for different powers of the diffusion coefficient.

The diffusion of zinc in InP is a complex process, and the concentration dependent diffusivity has been shown to be derived from the charge state of the interstitial. It has also been demonstrated that the charge of the interstitial diffusion species is highly dependent on the initial background donor concentration of the wafer, and this effectively determines the strengh of the concentration dependent diffusion

process [53]. Highly n-type doped InP wafers ($\sim 1 \times 10^{18}$ cm^{-3}) typically exhibit a cubic dependence of the diffusion constant (n=3), whereas un-doped wafers ($\sim 1 \times 10^{15}$ cm^{-3}) exhibit a linear dependence (n=1) [54]. Intermediate doping concentration on the order of 1×10^{17} will reveal a quadratic dependence (n=2) [53, 55]. This allows a simple way of controlling the diffusion front. Therefore, in our wafer, an n-type doping concentration of 2×10^{17} cm^{-3} was selected for the top InP cladding. According to previous reports, this should provide a very steep zinc diffusion profile.

3.4.1 Semi-sealed Open Tube Zinc Diffusion

Diffusion in III-V semiconductors materials has been achieved using different approaches such as sealed ampoule [55, 56], spin-on doped films [57, 58], and open-tube furnace technique [59, 60]. The open-tube technique is particularly attractive since it can be easily scaled to accommodate bigger samples making it suitable for processing large wafers. In our experiments, a semi-sealed open-tube diffusion technique was implemented because it is a relatively simple process, and the crystal quality after the diffusion is not degraded as compared to the sealed ampoule technique [61]. A schematic of the experimental diffusion setup is shown in Fig. 3.6. It consists of a conventional linear tube furnace and a graphite box that contains the sample and the Zn source. The graphite box is covered with a loose fitting graphite lid to achieve a higher Zn vapor pressure. The use of the graphite box, instead of a sealed ampoule, also provides a

consistent Zn vapor pressure for every run which translates into a more reproducible Zn

concentration and diffusion profile.
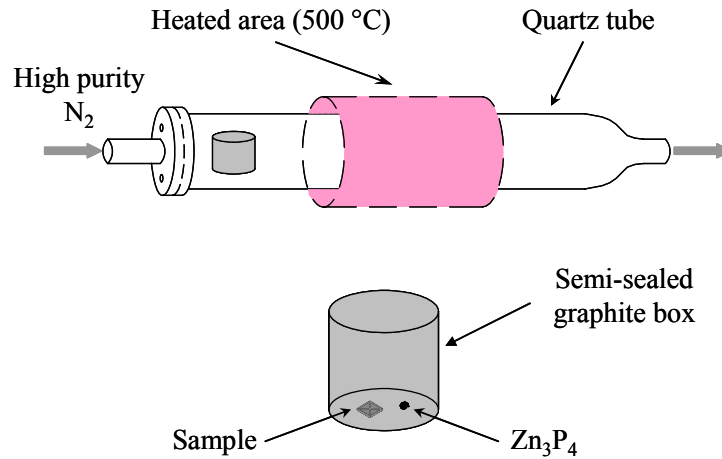
Figure 3.6 Experimental zinc diffusion setup.

During the diffusion process the boat is initially placed in the unheated zone of

the furnace as the latter is purged with high purity nitrogen for 20 min. The nitrogen flow

is then reduced to a trickle flow of 25 cm^3/s, and the furnace temperature control is set to

the required temperature. After the temperature has been fully stabilized, the boat is then

pushed into the heated zone for the required diffusion time. After the required diffusion

time, the graphite boat is pulled back to the low temperature zone and cooled down to

room temperature with the aid of external fans. Typically, a diffusion temperature higher

than 420 °C (melting point) is required to achieve enough vapor pressure and a good

diffusion rate. At this elevated temperature the vapor pressure above III-V materials is

dominated by that of the more volatile group V element, phosphorous (P) in the case of InP. Therefore, elemental zinc can not be used as the diffusion source because thermal decomposition of the wafer surface occurs due to P depletion that results in indium droplet nucleation [62]. A simple solution for this problem is the use of zinc phosphide (Zn_3P_2) as the zinc source. When the material is heated, the phosphorous component provides an over-pressure of phosphorus that prevents the surface decomposition of the InP based compounds, and allows for further processing of the wafer.

3.4.2 Experimental Zinc Diffusion Profiles

The diffusion process was carried out at a temperature of 500 $^\circ$C using 100 mg of Zn_3P_2 as the Zn source. These values were kept constant for every run, leaving the diffusion time as the only variable. After the diffusion, the depth profile of the zinc concentration that was incorporated into the sample was measured by secondary ion mass spectrometry (SIMS). The Zn profile for diffusion times of 30 and 45 min. is shown in Fig. 3.7. The phosphorous concentration is also shown in this figure as a reference, since the multiple quantum wells are clearly resolved. In both cases the zinc concentration is slightly higher than 10^{18} cm^{-3} at the surface, and decreasing only slightly as it goes deeper, reaching a point where a sharp drop to the background level of the SIMS is observed over a further 20 nm of depth. It can also be observed that by changing the diffusion time we can easily control the depth of the Zn diffusion front, with the 45 min.

diffusion corresponding to the upper limit before the Zn reaches the MQW's. From these measurements an average diffusion rate of 0.18 μm/min$^{1/2}$ was calculated, which is consistent with previous experimental results in n-type InP [55]. Also shown in Fig. 3.8 is a theoretical fitting of the experimental results. As expected, the best fit corresponds to a quadratic dependence of the diffusion coefficient which is typically observed for an acceptor concentration on the order of 10^{17} cm^{-3}.
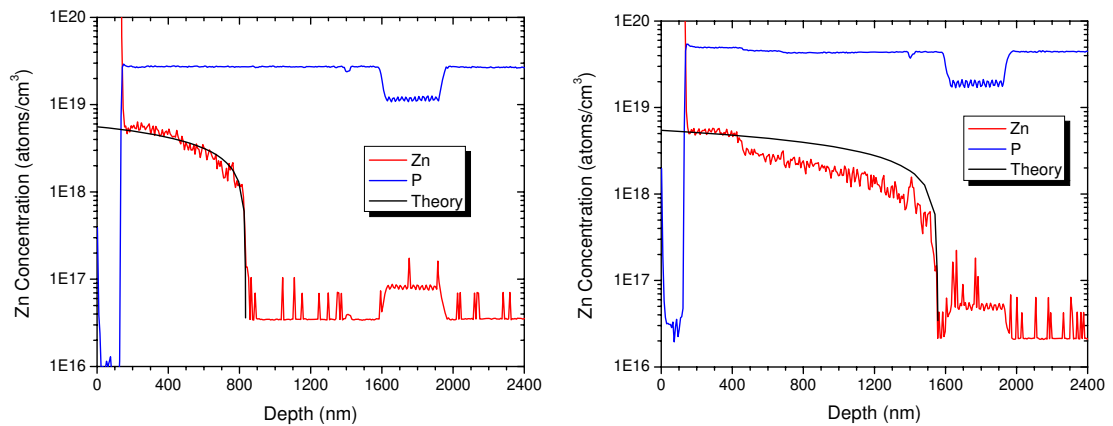
Figure 3.7 Experimental zinc diffusion profiles and theoretical fitting (n=2) for 30 min (left) and 45 min. diffusion (right).

To selectively define p-n junctions using this process, a suitable diffusion mask is required. This is achieved by depositing a 200 nm thick Si$_3$N$_4$ film using PECVD. The areas where p-n junctions will be created are defined using standard photolithography, and the Si$_3$N$_4$ is etched away using reactive ion etching (RIE). The diffusion process is then performed using the semi-sealed open tube diffusion technique. Finally, the Si$_3$N$_4$ is removed using RIE leaving the wafer ready for further processing. We found the process

to be very reliable and reproducible as long as the temperature, Zn source, and time are carefully controlled.

3.5 Ohmic Contacts

The operation of optoelectronic devices requires electrical connections to be made to the device and these are realized by using metal-semiconductor contacts. Metal-semiconductor contacts can be divided into two types, based on their current-voltage characteristics. Contacts which show rectifying characteristics are called Schottky barriers or rectifying contacts, and contacts which have linear current-voltage response are know as ohmic contacts. An ideal ohmic contact must have no effect on device performance, i.e., it must be capable of delivering the required current with minimal to no voltage drop between the semiconductor and the metal.

The equilibrium band diagram of an ideal n-type ohmic contact is shown in Fig. 3.8 [30]. In this case the work function of the semiconductor (ϕ_S) is greater than the work function of the metal (ϕ_m). When contact is made between the metal and semiconductor, the Fermi levels are aligned and there is no potential barrier. Therefore, equal currents will flow under forward and reverse bias. A similar behavior is expected for p-type, but in that case $\phi_m \rangle \phi_S$. The main limitation is that metal and semiconductor combinations with the required ϕ_m and ϕ_S values are hard to find, and ohmic contacts are difficult to fabricate in this way. In practice, a Schottky barrier is usually formed in a metal-(n-type) semiconductor contact as shown in Fig. 3.8. Here, χ_S is the electron affinity of the

45

semiconductor, $\phi_b = \phi_m - \chi_S$ is the barrier height, and the band-bending or built-in potential is equal to $V_{bi} = \phi_m - \phi_S$. In this case, ohmic contacts can be obtained by reducing the specific contact resistance of such contact.

In general, this can be done in two ways. The first is to reduce the Schottky barrier by heavily doping the substrate. As the doping in the semiconductor is increased, the depletion region becomes narrower, facilitating field emission or tunneling and giving a low contact resistance. The second way is to use a semiconductor contacting layer with an appropriate energy gap which will create a contact with a lower Schottky barrier. In real life, therefore, an ohmic contact must have a contact resistance that is as small as possible, to make it negligible in comparison to the bulk or spreading resistance of the semiconductor.
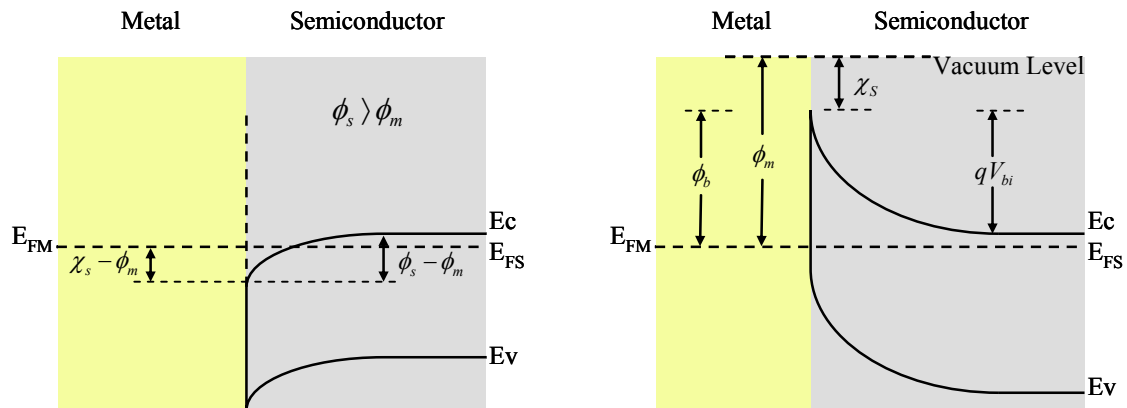
Figure 3.8 Band diagrams of an ideal n-type ohmic contact (left) and real metal-(n-type) semiconductor contact (right).

46

3.5.1 P-type Ohmic Contacts to InGaAs

P-type ohmic contacts to InP-based devices are typically made to $In_{0.53}Ga_{0.47}As$ rather than directly to InP. This is because its low band gap ($E_g \approx 0.75$ eV) relative to InP ($E_g \approx 1.35$ eV) and high dopant solubility ($\approx 10^{19}$ cm^{-3} for zinc) permit the formation of low resistance contacts [63]. The doping of this layer (~100 nm) is usually on the order of 10^{18}-10^{19} cm^{-3}, with the highest concentration providing the lowest resistance. As for the contact metals, the Gold/Platinum/Titanium (Au/Pt/Ti) combination is by far the most frequently used one [64]. The Ti layer provides good adhesion to the underlying semiconductor, while the Pt layer acts as a diffusion barrier for gold. Due to Pt high melting point (~ 1769 $^\circ$C), we were unable to evaporate this metal. Therefore, our contacts were made by using a combination of Au (200 nm)/Zn (20 nm)/Ti (7 nm). During the contact annealing, the Zn will diffuse into the region under the contact and dopes the semiconductor degenerately p-type. This is particularly important in our contacts since we are creating our p-type regions by Zn in-diffusion, and it is well know that the active Zn concentration is at least one order of magnitude less when compared to the total Zn concentration.

The specific contact resistance was measured using the transmission line method (TLM) [30]. The contact pads were deposited on a sample through which Zn had been diffused for 30 min. We also used an epitaxially grown p+ $In_{0.53}Ga_{0.47}As$ with a doping concentration of 1×10^{18} cm^{-3} as a reference for our Zn diffused contacts. The results are shown in Fig. 3.9, where the specific contact resistance is plotted against the annealing

temperature. All rapid thermal annealings (RTA) were performed for 30 seconds. As can be observed, without annealing the specific contact resistance in both cases was on the order of 10^{-3} Ωcm^2. As the annealing temperature is increased the contact resistance is decreased reaching a value of 5 x 10^{-5} Ωcm^2 for an annealing temperature of 420 $^{\circ}$C, with both samples following a similar behavior. From these results it is clear that a good ohmic contact was formed on our Zn diffused samples, with comparable results to the ohmic contact formed on an as-grown p+ In$_{0.53}$Ga$_{0.47}$As semiconductor.
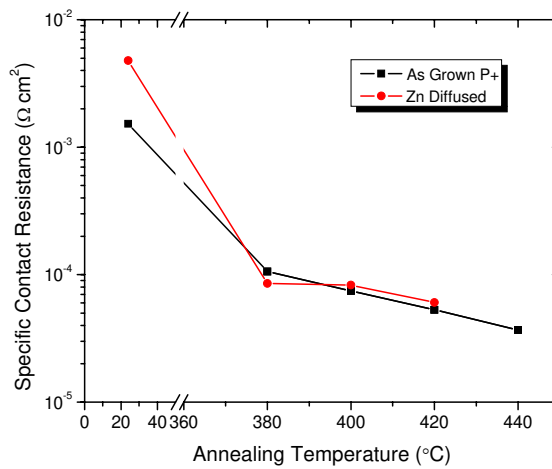
Figure 3.9 Specific contact resistance as a function of processing temperature for p-type contacts.

3.5.2 N-type Contacts to InP

The most employed recipe for fabricating n-type contacts consist of a combination of Gold/Germanium/Nickel (Au/Ge/Ni) [65, 66]. In this case, the Ni layer

provides adhesion to the semiconductor, while the Ge will diffuse into the region under the contact during the annealing providing a degenerately doped n-type semiconductor. Our n-type contact will be formed at the bottom of the sample, and therefore the initial doping of the semiconductor is 3×10^{18} cm^{-3}. Our contacts consisted of thermal evaporation of Au (200 nm)/Ge (20 nm)/Ni (4 nm) followed by annealing at different temperatures for a duration of 30 seconds. The results are shown in Fig. 3.10. In this case, even without any annealing, a specific contact resistance of 7 x 10^{-5} Ωcm^2 is obtained. Annealing the sample at 420ºC decreases this value slightly to 3 x 10^{-5} Ωcm^2.
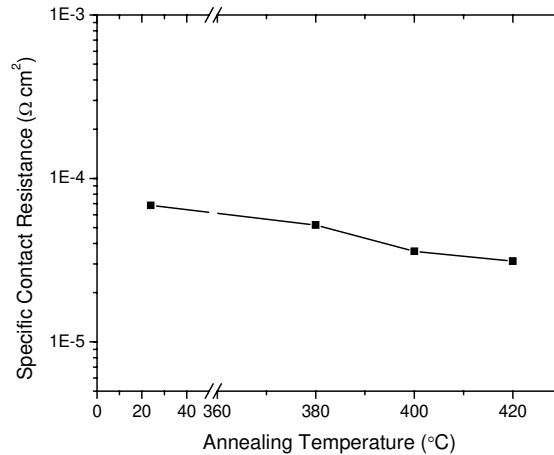
Figure 3.10 Specific contact resistance as a function of processing temperature for n-type contacts.

3.6 Current-Voltage Characteristics of P-N Junctions

The electrical characteristics of the Zn diffused p-n junction were characterized by measuring their current-voltage (I-V) response. Measurements were performed in a

fully completed Mach-Zehnder switch, with isolated p-type regions formed by diffusing Zn for a duration of 29 min. A cross section of the semiconductor doping and contact configuration is shown in Fig. 3.11 (a). In this case, the electrical biasing can be applied either through the top contacts only, or top to bottom contacts. When the bias is applied top to top we have a back-to-back diode configuration. On this configuration, regardless of polarity of the applied voltage, one of the p-n junctions will be reverse biased. Therefore, the current is always limited and we should expect a reverse bias like behavior under positive and negative voltage bias.

As shown in Fig. 3.11 (b), the breakdown voltage on both regimes is $\sim \pm 10$ V, meaning that the junction in both arms are very similar. This allows us to apply up to $\pm$ 10 V to either arm, while drawing a negligible current of 2 µA. When biasing top to bottom through either one of the top contacts, the typical p-n diode characteristic is obtained. The I-V responses for reverse and forward bias are shown in Fig. 3.11 (c) and (d), respectively. As expected, in this case the reverse bias draws a minimal amount of current, whereas the forward bias allows for efficient current injection. From these results is clear that good p-n junctions are obtained with our Zn diffusion process. The advantage of the process is that it allows selective definition of the junctions at any location on the wafer.
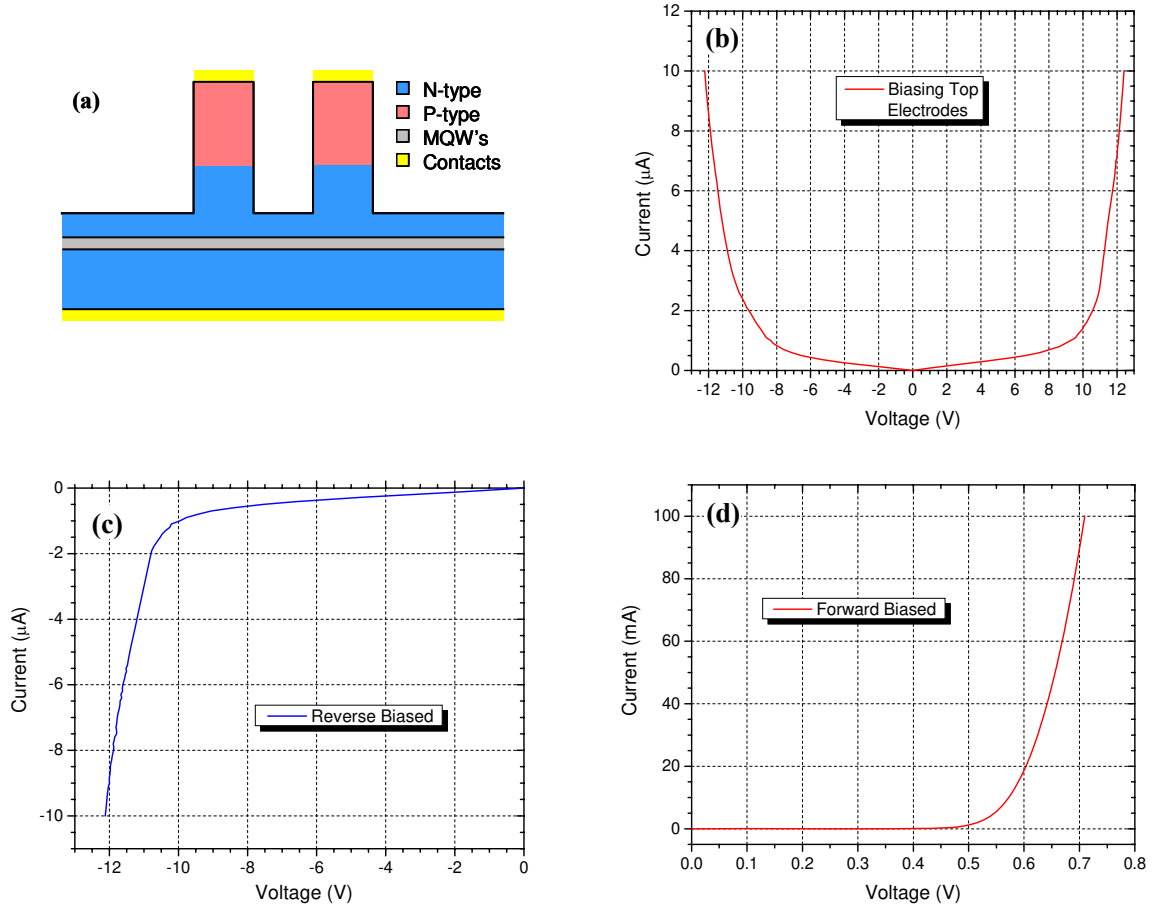
Figure 3.11 (a) Schematic of semiconductor structure used for I-V characterization, (b) I-V curve for biasing through top electrodes, (c) I-V curve for reverse biased top to bottom, and (d) I-V curve for forward biased top to bottom.

In this dissertation we describe different integrated photonic devices that were made using the fabrication techniques described above. The Zn in-diffusion process is proven to be a key device processing technique for achieving highly functional devices. In the following chapters the design, fabrication, and testing of such devices will be explained in detail.

CHAPTER 4: MACH-ZEHNDER INTERFEROMETER SWITCH

Among the different configurations used for integrated switches/modulators, the Mach-Zehnder interferometer (MZI) has been the most successful structure. MZI switches have been successfully fabricated employing different platforms [67-74]. However, InP-based MZI are very attractive because of their compact size, low driving voltage, and compatibility of integration with other devices [71-76]. Although most of the MZI applications are related to digital modulation, analog modulation is also very important due to the development of novel modulation schemes. In order to provide direct analog modulation without the use of any electronic signal conversion, isolated p-n regions are required across the device. This can be achieved by etching trenches along the waveguiding structures. However, this approach introduces significant additional losses to the device of ~2.8 dB per trench (~5.6 dB per arm) [73, 77]. A better technique is the use of zinc in-diffusion in order to generate those isolated junctions. In this case losses arise as a result of free-carrier absorption, and can be regulated by controlling the diffusion depth. In this chapter we demonstrate different configurations of integrated MZI switch/modulator using the zinc in-diffusion process that we previously described [78, 79].

4.1 1x2 Mach-Zehnder Switch with Directional Coupler

In this section the design and operation of the waveguiding structure of the MZI device is described. Shown in Fig. 4.1 is a schematic layout of the MZI switch.
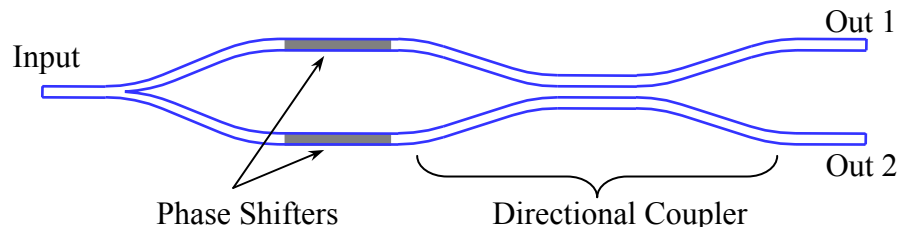
Figure 4.1 Schematic of 1x2 Mach-Zehnder switch with directional coupler.

The operation principle is as follows: The input light is divided by a Y-junction into two light beams of equal amplitude and phase. The two light beams then follow different paths, and they enter the separate arms of the 3-dB directional coupler. With no electric field applied the optical fields that enter the arms of the directional coupler are in phase. Therefore the output ports of the device share equal power. When an electric field is applied to one arm of the interferometer, and a relative phase change of $\pi/2$ is introduced, the light is switched completely to the output that is connected to that arm. Depending on which arm is phase shifted, we can switch the light from one output port to the other. In general two requirements need to be met in order for the switch to work properly. First, we need to be able to induce a $\pi/2$ phase shift on each arm of the MZI without inducing any loss of optical power. This can be easily achieved because, in

53

principle, the QCSE allows us to induce large index changes with minimum losses. The second critical requirement is that an exact 3-dB directional coupler is needed. Assuming that these requirements are met, the MZI can be modeled using the equation describing a directional coupler with two inputs [80],

$$E_1(z) = E_1(z=0)\cos(\kappa z)\exp(j\beta_1 z) + jE_2(z=0)\sin(\kappa z)\exp(j\beta_2 z)$$

$$E_2(z) = jE_1(z=0)\sin(\kappa z)\exp(j\beta_1 z) + E_2(z=0)\cos(\kappa z)\exp(j\beta_2 z)$$

$$(4.1)$$

with $L_c = \dfrac{\pi}{2\kappa}$ and $\beta = \dfrac{2\pi n_0}{\lambda}$, where L_c is the critical coupling length, κ is the coupling coefficient, and n_0 is the effective refractive index. In addition propagation losses need to be minimized to obtain low insertion losses. In our device losses are mostly related to free carrier absorption that can result from the Zn in-diffusion process and scattering of the guided mode at the waveguide bends.

4.1.1 Free Carrier Absorption

Free carrier absorption is related to the absorption of photons by free carriers in elevating their potential energies within the conduction band or the valence band. The momentum change that is required by the process is readily provided by either optical or acoustic phonons or by impurity scattering. The free carrier absorption coefficient is directly related to the free carrier concentration by an empirical formula that includes a weighted sum of the three processes [30]. The absorption losses were characterized by

fabricating 1 mm long and 2 µm wide straight waveguides that pass through 500 µm length of zinc diffused material. The diffusion was carried out for several different durations, and each batch contained control waveguides that were protected from the Zn in-diffusion. This allowed us to extract the waveguide losses that are directly caused by the intrinsic free carrier absorption. The losses were measured using the scanning Fabry-Perot resonances technique [81], and the results are shown in Fig. 4.2.
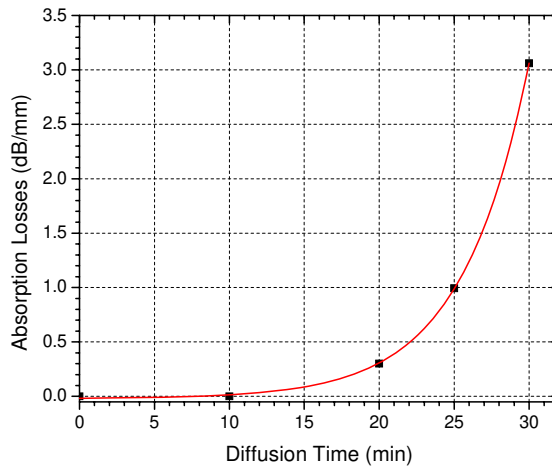
Figure 4.2 Measured free carrier absorption losses as a function of diffusion time.

As shown in Fig. 4.2, the waveguiding loss increases almost exponentially as the Zn depth is increased. This is explained by a larger spatial overlap between the Zn dopant impurities and the optical mode profiles. Therefore, the extent of the Zn depth has to be carefully controlled to minimize total insertion loss. However, for shallower diffusion depths, the junction will be farther away from the MQW's and the voltage that is required for switching will then be increased. As will be observed in the following sections, there

is a fine trade-off between the level of absorption that can be tolerated and still maintaining a low applied bias requirement.

4.1.2 Directional Coupler Design

The directional coupler is the most critical part in our MZI. The splitting ratio can be easily modified by changing its length, width of the waveguides, and confinement factor. Therefore, some variables were fixed in order to determine the appropriate coupler dimensions, and also the location of our etch-stop layer which controls the confinement factor of our waveguides. As shown in Fig. 4.3 (Left) the separation between the waveguides in the active phase control region is set to 30 µm. Also shown in Fig. 4.3 (Right), is a cross section of the directional coupler along a-a'. All the waveguides are 2 µm wide and designed to support single mode operation, and they are separated by a gap of 2 µm along the straight portion of the coupler section.
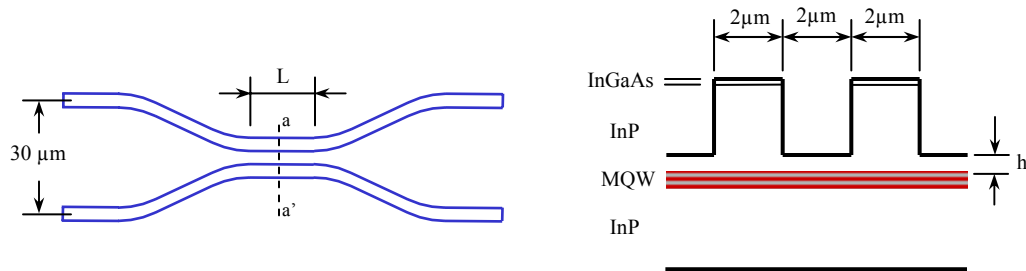
Figure 4.3 Initial dimensions employed in designing the directional coupler.

The only variables left are the radius of curvature of the bending regions and the

thickness of the cladding left after the etching (h). Both variables affect the ultimate length of the coupler (L). The minimum radius of curvature as a function of h was obtained using a finite-difference beam propagation method (FD-BPM), and was taken as the value at which the transmitted intensity dropped to 95%. As shown in Fig. 4.4 (a), the radius of curvature can be significantly reduced as h is decreased, which can provide a shorter device. However, because of the crystallographic etching dependence of InP discussed in chapter 3, a sharp curve could lead to distorted waveguides and losses could be significantly higher that the calculated values.
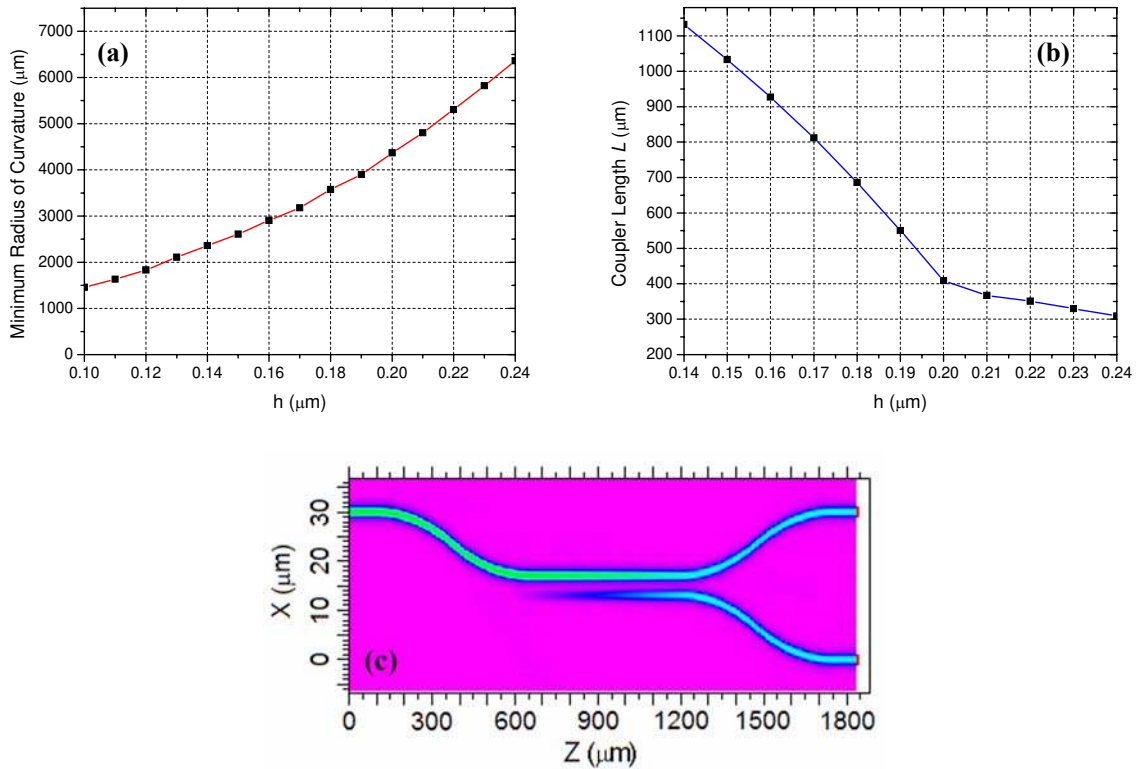
Figure 4.4 (a) Minimum radius if curvature as a function of parameter h, (b) Coupler length (L) as a function of parameter h, and (c) Beam propagation characteristics of final directional coupler.

A radius of curvature of 6,000 µm was chosen for the waveguide bends so that the devices should be realizable using wet etching process and still not suffer any significant radiation losses. Once the curvature has been selected we focus our attention to the length of the coupler (*L*). There is usually a trade-off between coupler length and fabrication tolerances. A short coupler is good since total device length is reduced, but becomes very sensitive to fabrication errors, and vice-versa. Typically, a coupler length between 450-500 µm has provided a good compromise between coupler length and fabrication tolerances [82, 83]. The FD-BPM was used to characterize the coupler length *L* as a function of *h*, and is shown in Fig. 4.4 (b). We selected a value of *h*=0.19 µm which provides a value of *L*=550 µm. The beam propagation characteristics of a properly designed 3-dB coupler are shown in Fig. 4.4 (c).

The beam propagation characteristics of the full device are shown in Fig. 4.5. As can be observed in Fig. 4.5 (a), during the off-state the incoming light is split equally to both outputs. When a π/2 phase change is applied to one of the arms, light is switched to that particular arm as shown in Figs. 4.5 (b) and (c). Also shown is the response of the MZI as a function of phase change which is obtained using Eq. 4.1. It is clear that efficient switching/modulation can be achieved if the required phase change and coupler requirements are met.
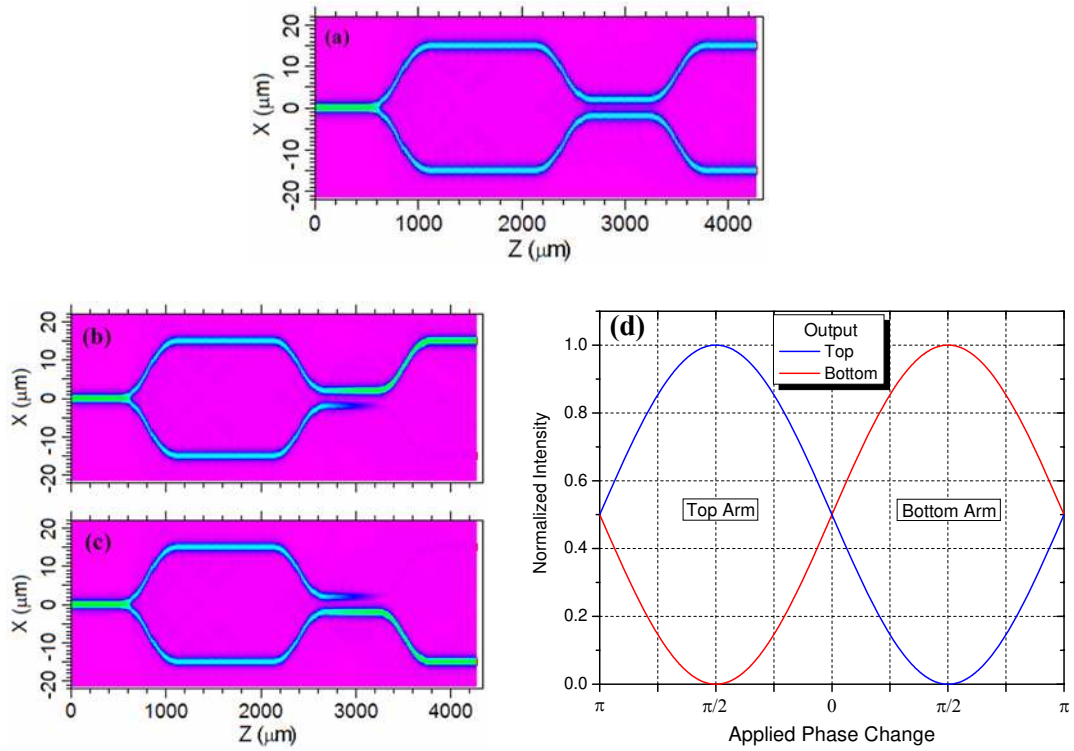
Figure 4.5 Beam propagation characteristics of MZI at (a) Off-state, and with $\pi/2$ phase shift applied to (b) upper arm, and (c) lower arm. (d) MZI response versus phase change as obtained from Eq. 4.1.

4.1.3 Device Fabrication

Prior to fabricating the full device, the directional coupler section was fabricated and tested. The device fabrication was started by first depositing a 200 nm thick Si_3N_4 film. Standard photolithography followed by dry etching of Si_3N_4 was used to transfer the directional coupler structure to the Si_3N_4 film. The structure was then transferred to the semiconductor using the selective InGaAs and InP wet chemical etching that ended at the

InGaAsP etch-stop layer. The etch-stop layer was also removed by wet etching and finally the sample was lapped down, polished, and cleaved for testing.

The device was tested by launching light at a wavelength of 1.55 µm into the upper arm and measuring the output intensity at the upper and lower output waveguides. Three different coupler lengths were used (500, 550, and 600 µm). As shown in Fig. 4.6, all couplers lengths were severely over-coupled. This response could be caused by slight variations in the dimensions of the fabricated waveguides, but this possibility was disregarded because the results were consistently found with several different samples. We believe that this issue is related to the difference between the actual values of refractive indexes and the ones that were used in the simulations.
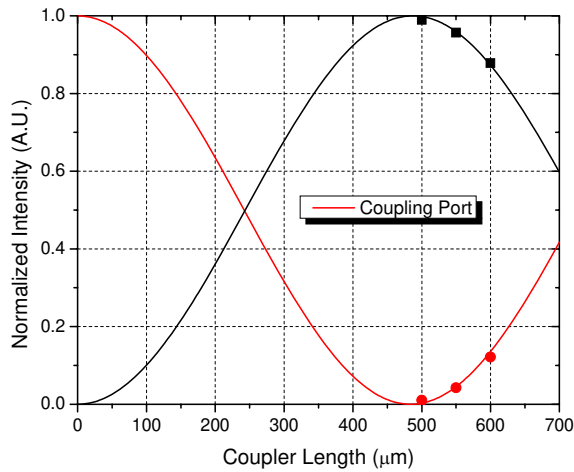
Figure 4.6 Experimental directional coupler response.

Regardless of the source, the coupler has to be re-designed with corrected dimensions for the MZI device to operate properly, and this can be achieved in two ways.

60

1. By taking advantage of the selective wet etching, the remaining InP can be etched deeper. This allows us to further reduce the value of h, which as shown in Fig. 4.4 (b) increases the length required to obtain a 3-dB coupler. By removing ~ 40 nm of InP beyond the InGaAsP etch-stop layer (h=0.15 µm), the coupler response was very close to an ideal 3-dB coupler as shown in Fig. 4.7. Although a very slow etching rate of 80 nm/min can be achieved using $HCl:CH_3CO_2H:H_2O$ (1:6:1), obtaining consistent etching of such small thickness in every sample was difficult.
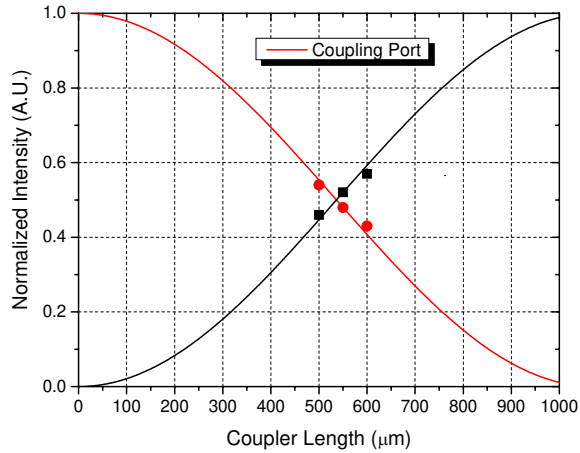
Figure 4.7 Experimental directional coupler response after uniformly removing ~ 40 nm of InP beyond the etching stop (h=0.15 µm).

2. The second approach is shown in Fig. 4.8 (a), in which the coupler is divided in two sections. The cross section dimensions a-a' of the un-shadowed portion has similar dimensions as showed in Fig. 4.3 (Right) with h=0.19 µm. In the shadowed portion, the InP is completely etched away (the InP etching will

61

eventually stop at the quaternary MQW's composition) thus giving a value of $h=0$ as shown in Fig. 4.8 (b). This completely eliminates the coupling in this portion of the coupler, and effectively reduces the coupler length from L to a new length L_{eff}. As shown in Fig. 4.8 (c), a 3-dB coupler is obtained with a $L_{eff}=170$ μm. More importantly is that the results were more consistent due to the etching stop provided by the MQW's, and therefore this process was employed to trim our coupler during the full device fabrication.
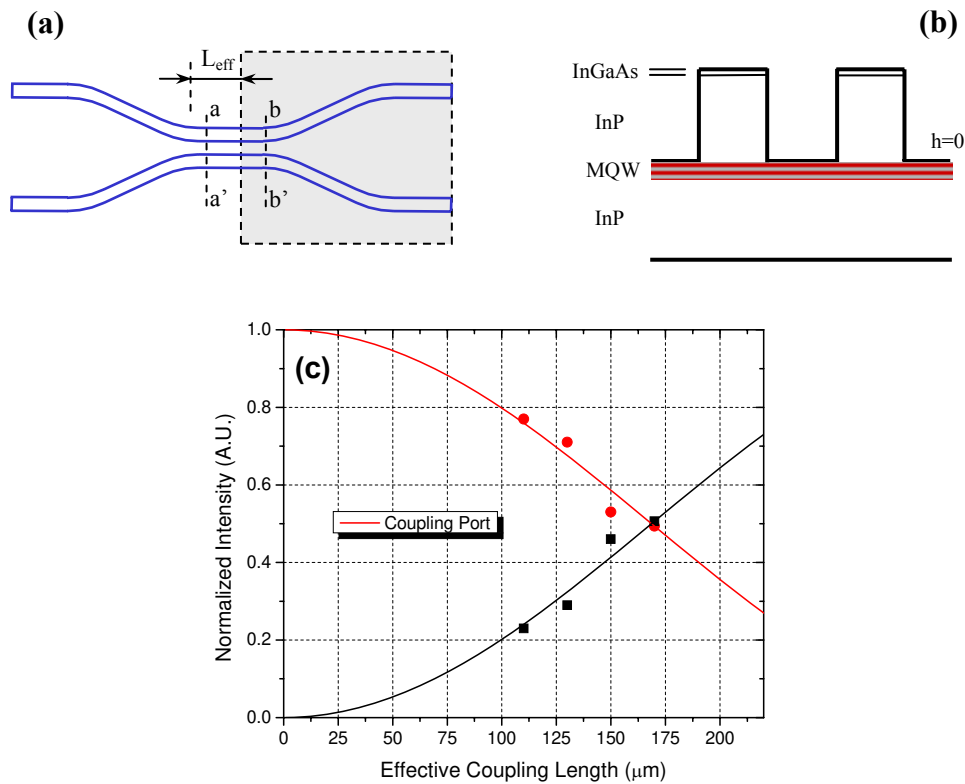
Figure 4.8 (a) Schematic of new concept for trimming the directional coupler response, (b) Cross section b-b' of shadowed region showing $h=0$, and (c) Experimental directional coupler response after trimming process.

Fabrication of the full MZI started with a thorough cleaning of the sample with buffered oxide etchant (BOE) for 2 min. to remove any native oxide, followed by a thorough rinsing with DI water. After the sample cleaning, a 200 nm thick Si_3N_4 film was deposited using PECVD, Fig. 4.9 (a). Conventional photolithography using Futurrex negative resist NR7-500P followed by a CF_4 plasma etching was used to define two 20 μm × 500 μm windows, Fig. 4.9 (b). The Si_3N_4 film was used as a mask for the Zn diffusion process. Zinc was then diffused into the sample for a duration of 29 min. using the semi-sealed open tube diffusion process described in the previous chapter, Fig. 4.9 (c). After the diffusion process, the sample was immersed for 10 sec in $H_3PO_4:H_2O_2:H_2O$ (1:1:30) mixture to etch off approximately 15 nm of InGaAs, followed by complete removal of the Si_3N_4 film using plasma etching. This procedure rendered the diffusion windows and the alignment marks visible after removal of the Si_3N_4 film, Fig. 4.9 (d). The sample was then covered with a fresh Si_3N_4 film and the Mach-Zehnder switch was then patterned by photolithography (Shipley 1805 positive resist), followed by plasma etching of the Si_3N_4 film, and wet chemical etching of the InGaAs top layer using a $H_3PO_4:H_2O_2:H_2O$ (1:1:30) mixture. The patterned InGaAs layer was then used as the mask to transfer the pattern to the underlying InP to a depth of 1.4 μm using a selective etchant of $HCl:CH_3CO_2H$ (1:6) mixture, Fig. 4.9 (e). Trimming of the coupler was performed by standard photolithography using Shipley 1813 resist, followed by wet etching of the InGaAsP etching stop using $H_3PO_4:H_2O_2:H_2O$ (1:1:30) mixture. The remaining InP was wet etched with an $HCl:CH_3CO_2H:H_2O$ (1:6:1) mixture, Fig. 4.9 (f).

(a) Deposition of silicon nitride diffusion mask

(d) Light etching of InGaAs cap to reveal the Zn diffused areas

(b) Opening diffusion windows

(e) Delineation of the waveguide MZI structure

(c) Zn in-diffusion

High purity N$_2$

Heated area (500 °C)

Quartz tube

Semi-sealed graphite box

Sample

Zn$_3$P$_4$

(f) Trimming of the 3-dB coupler

(g) BCB planarization and laying ohmic metal contacts

Figure 4.9 Device fabrication steps for 1x2 MZI with directional coupler.

The sample was then planarized using a spin-on benzocyclobutene (BCB) planarization film. Ti/Zn/Au p-type contacts (500 μm long) were patterned on top of the zinc diffused areas using a lift-off technique with Futurrex NR7-1000PY resist. After annealing at 420°C for 30 sec, the contacts were then used as the mask for removal of the uncovered BCB film by RIE using an oxygen plasma with a 30% mixture of CF_4, Fig. 4.9 (g). Finally, after the wafer was lapped to a thickness of 150 μm and polished to a mirror finish, the sample was cleaved and mounted on a copper header in preparation for device testing.

A photograph of the top view of a fabricated batch of MZI devices is shown in Fig. 4.10. Also shown are close-up pictures of the Y-junction, contacts, and directional coupler at the trimming interface.
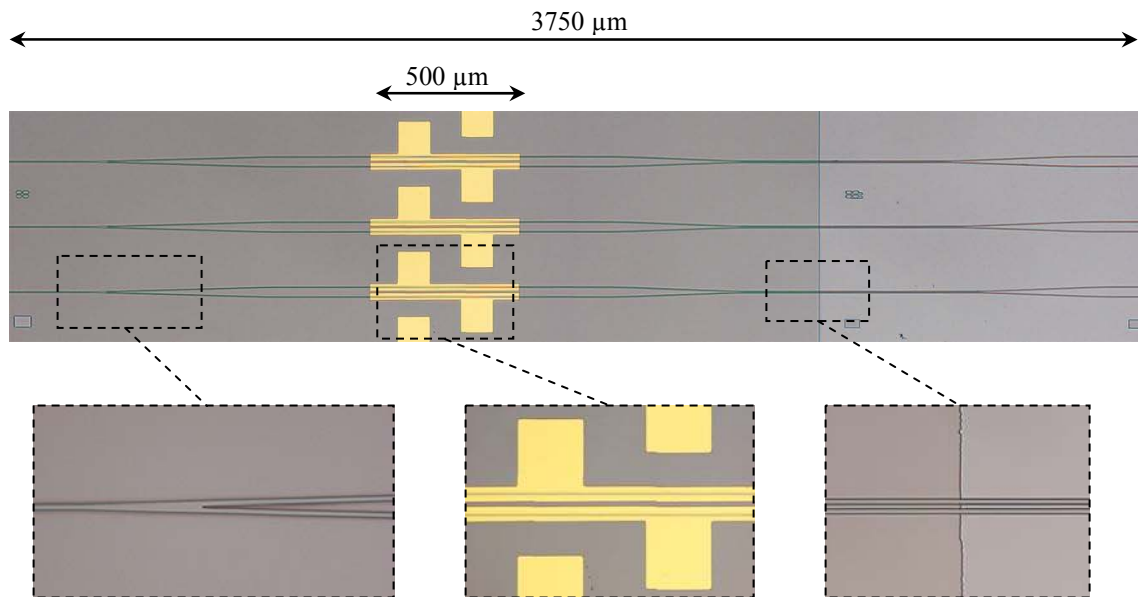
Figure 4.10 Pictures of fabricated 1x2 MZI devices (Top view).

4.1.4 Experimental Results

The device characteristics were tested using the setup shown in Fig. 4.11. Light from a tunable laser (Agilent 8164A Lightwave Measurement System) was coupled into the input waveguide using a 40x microscope objective lens. The light from the output waveguides of the switch was collected using a 25x microscope objective lens. A beam splitter was used to split the light so as to allow monitoring of the output facet using an infrared camera (MicronViewer 7290A from Electrophysics) and measuring the output powers in the two output ports of the switch using an InGaAs photo-detector (Thorlabs PDA255). The input beam was modulated by a mechanical chopper and the detected output beam intensity was measured using a lock-in amplifier. The bias voltage was applied using a Keithley 2400 Sourcemeter to one arm of the interferometer while the other arm was grounded. The setup was computer controlled using LabVIEW software.
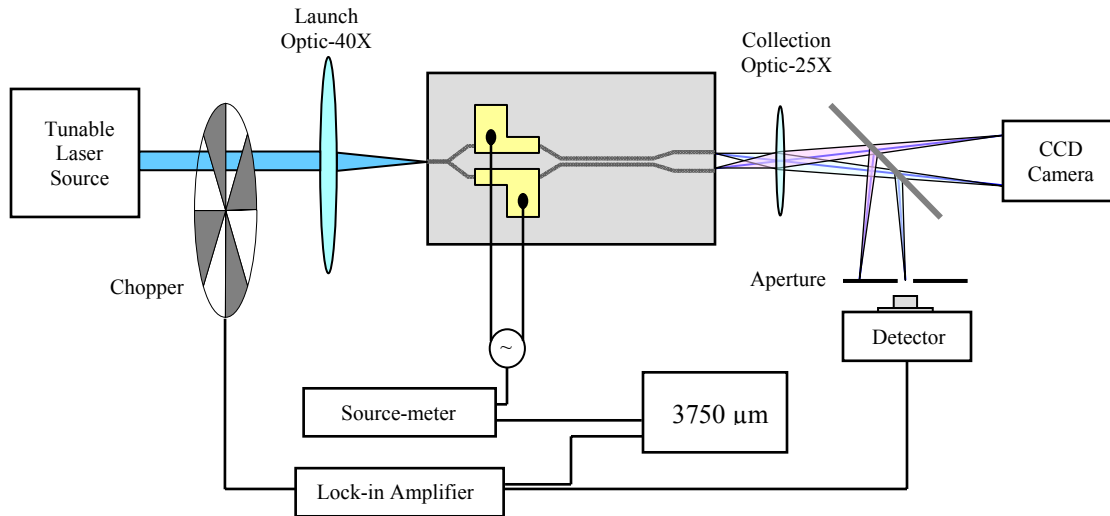
Figure 4.11 Experimental setup for testing MZI devices.

The experimental results of the 1x2 MZI are shown in Fig. 4.12 for TE polarization. Without any bias applied to the device, it is clear from Fig. 4.12 (a), that the splitting ratio is significantly off from the expected 50:50. However, when the bias is changed from -1.9 to +1.4 volts, light is switched from the left to the right output waveguides.
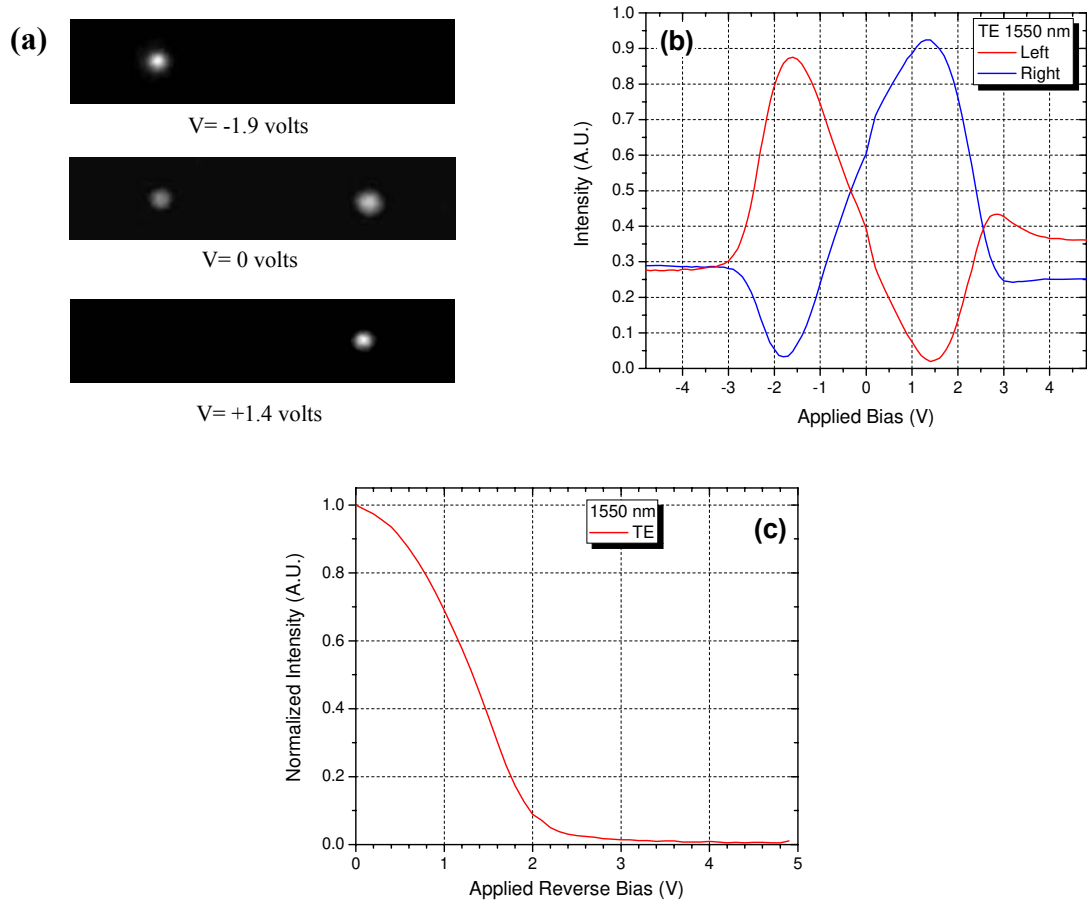
Figure 4.12 1x2 MZI response at 1550 nm (a) Near field pictures at different applied bias, (b) Device response as a function of applied bias, and (c) Electro-absorption measurements for TE polarization.

The switch response at 1550 nm wavelength as a function of applied bias is shown in Fig. 4.12 (b). The oddities that are observed in this graph can be explained using the electro-absorption behavior of the device as shown in Fig. 4.12 (c). With zero bias the shift from the 50:50 splitting ratio can be caused by any of the following cases:

1. An initial phase difference between the incoming signals at the coupler.

2. If the amplitude of the incoming signals is different.

As shown in the electro-absorption measurements for TE polarization, at and beyond -4 and +4 volts, light propagating through the arm that is reverse-biased is completely absorbed through QCSE as shown in Fig. 4.12(c). Therefore, at this bias voltage the output signals shown in Fig. 4.12 (b) correspond to the response of the output directional coupler for light traveling through the unbiased arm. The first observation is that the coupler response is asymmetric, since a different splitting ratio is obtained for applied biases lower than -4V and higher than +4V, which correspond to light being launched into the directional coupler through one input port (right) or the other (left) input port respectively. Additionally, the sum of the output signals at -4 volts corresponds to the light passing to the coupler through the right arm, and at +4 volts, the sum of the output signals corresponds to the light passing through the left arm. From Fig. 4.12(b), it is apparent that the signal passing through the left arm is higher than that passing though the right arm, which indicates that there is non-uniform attenuation losses in the device structure and these lead to a non-symmetric overall response. We attribute this to the different etching rates experienced by the p-type and n-type regions. The combination of these two effects results in a shift on our switch response. The difference in the maximum

intensity obtained when switching between channels, is a direct consequence of this initial shift. Because a larger voltage is needed to reach the phase induced shift, electro-absorption prevents the power coupled to the left output port from rising as high as in the right output port.
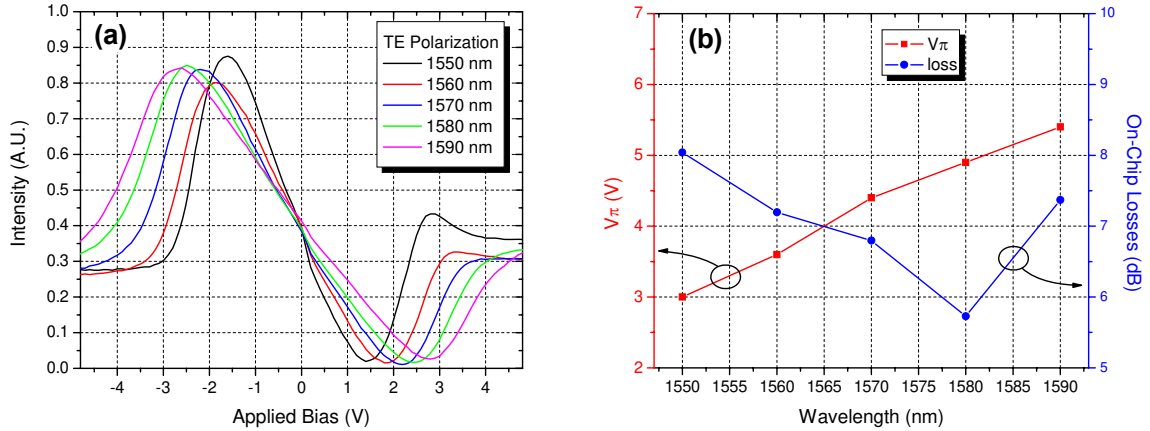
Figure 4.13 (a) Wavelength response of the device, and (b) V_π voltage and on-chip losses as a function of wavelength.

The wavelength dependence of the switch is shown in Fig. 4.13 (a). The modulator's response curves for all wavelengths are very similar, with the device only requiring a higher voltage for the longer wavelengths. Fig. 4.13 (b) shows a plot of the required switching voltage V_π as a function of wavelength. These results are typically expected in this type of MQW based modulator because as we move to longer wavelengths away from the resonant absorption peak the refractive index change gets progressively weaker. Also shown in Fig. 4.13 (b) is a graph of the on-chip losses as a

function of wavelength. The highest on-chip insertion loss is on the order of 8 dB, which is lower than the typical insertion losses encountered in the literature [71, 84].
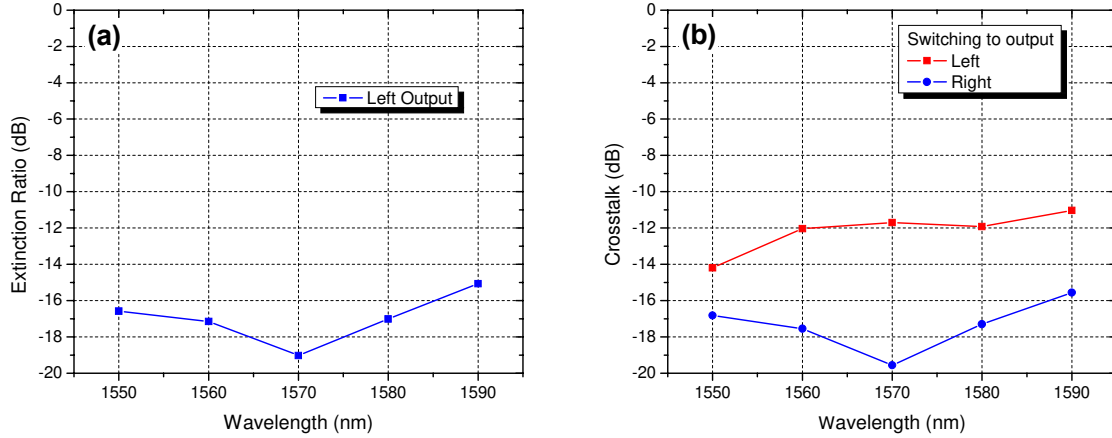
Figure 4.14 (a) Extinction ratio and (b) Crosstalk as a function of wavelength.

When the device is used as a modulator, the main parameter is the extinction ratio of the device. The extinction ratio of the left channel as a function of wavelength is shown in Fig. 4.14 (a). It can be observed that an extinction ratio of at least -15 dB is achieved over a 40 nm range, between 1550 and 1590 nm. For switching applications, the relevant parameter is the crosstalk between channels. As shown in Fig. 4.14 (b), crosstalk levels lower than -16 dB are observed when the light is switched to the right output. However, the level is on the order of -11 dB for the left output. This is also related to the higher electro-absorption which not only limits the maximum intensity at this point, but also the minimum achievable value.

The device response is seriously deteriorated under TM polarization because the

coupler becomes over-coupled due to the weaker waveguide confinement factor for the TM guided mode. Given this polarization dependence and fabrication issues, a better alternative for the 3-dB coupler is required. Multimode interference (MMI) couplers seem to be a better option since they require much lower fabrication tolerances, they possess a wide workable spectral bandwidth, and are relatively polarization independent [85, 86].

4.2 1x2 Mach-Zehnder Interferometer with MMI Couplers

The operation of a MMI device relies on a multimode waveguide that supports several modes (≥ 3). As the modes propagate along the MMI waveguide, the interference between them gives rise to the formation of self-images of the input field, see Fig. 4.15 (Left). By selecting the proper input field position and MMI length, accurate couplers and splitters can be designed. These devices have attracted a great deal of interest because they are very compact, have low polarization sensitivity, possess large optical bandwidths, and offer the advantage of relaxed fabrication tolerances [85, 86].
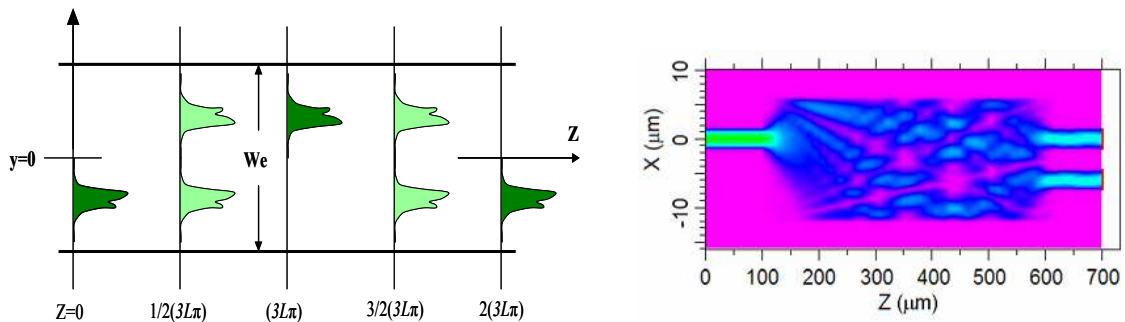
Figure 4.15 (Left) General MMI operation, and (Right) MMI 3-dB coupler.

The 3-dB MMI coupler is designed using restricted paired interference operation (section 6.1.2), since the length is reduced by one third compared to the general interference case. As shown in Fig. 4.15 (Right) a 3-dB splitter is obtained with a length of 484 μm. The width of the MMI region is 18 μm, and the input waveguides are 3 μm wide separated by a 3 μm gap.

Since an etch-stop is incorporated in the wafer design, and a further etch-stop at the MQW layer also exists, it was felt that etch depth control during the device fabrication was not an issue. We focused our attention to the fabrication tolerances of the MMI device in terms of lateral dimension errors (waveguide width) during the photolithography and etching, and compared them to the same effects on the waveguide directional coupler. As shown in Fig. 4.16 (a), as soon as the waveguide width of a directional coupler is varied from its optimum designed value (2 μm), a 3-dB splitting ratio is no longer maintained. In fact the split ratio is seriously modified when the width of the waveguide is increased by 0.5μm. In the case of the MMI device, the value in both output channels remains virtually equal for changes in the width of the MMI on the order of 0.5μm, as shown in Fig. 4.16. The only change is a significant increase in the total coupling losses when the width of the device does not correspond to the design parameter. As shown in the inset of Fig. 4.16 (b), is very easy to achieve close to a 3-dB splitting ratio.
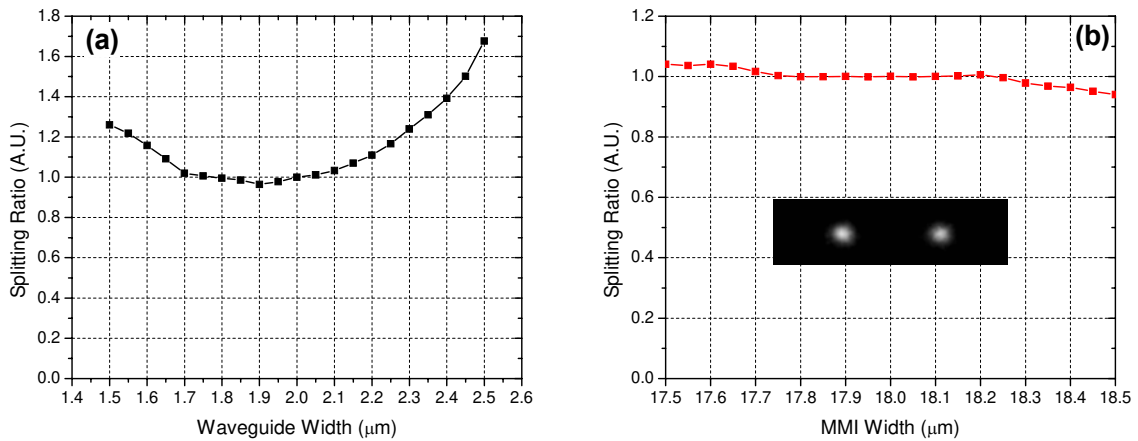
Figure 4.16 (a) Directional coupler and (b) MMI coupler splitting ratio as a function of waveguide (MMI) width.

Similarly, we have designed a MMI 1x2 splitter for replacing the input Y-junction of the MZI modulator. In this case the input waveguide is aligned at the center of the MMI, and therefore the device operates in the regime of restricted symmetric interference (section 6.1.1). The device length and width were 163 and 12 μm respectively, and the input and output waveguides were 3 μm. The output waveguides are also separated by 3 μm as with the MMI coupler. The response of the MMI splitter to slight MMI width modifications was similar to the MMI coupler. The new 1x2 MZI structure is shown In Fig. 4.17. The operation is exactly the same as the MZI with directional coupler. In the actual device, the output waveguides have a slight tilt angle such that at the output facet there is a gap of 6 μm between them.
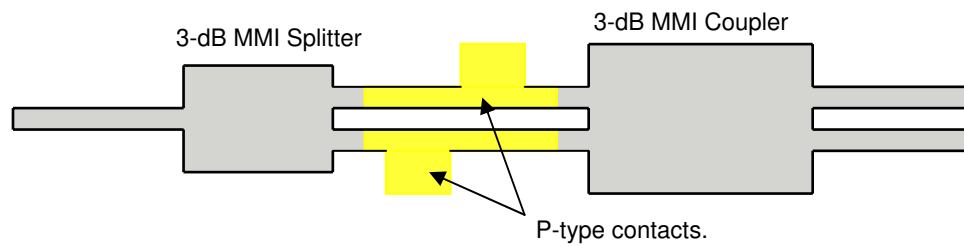
Figure 4.17 Schematic of 1x2 MZI switch with MMI coupler.

4.2.1 Experimental Results

The fabrication of the device follows the same processing steps as with the MZI modulator containing the directional coupler as shown previously in Fig. 4.9. The only differences are that the top cladding is etched further down to the top of the MQW's along the whole structure, and the diffusion time is reduced to 28 min. The reduction in diffusion depth is required because the effect of free-carrier absorption is increased due to the increased mode confinement. A photograph of the fabricated device is shown in Fig. 4.18. Three different batches of devices have been fabricated. Each batch contains five different MMI lengths, with the center one corresponding to the length obtained from numerical simulations. In each batch also, three different electrode lengths corresponding to 300, 500, and 700 μm have been made. As shown in the close-up of Fig. 4.18 the effects of crystallographic dependent etching are present on the corners of the MMI splitter and coupler. The detrimental effects of these angled corners will become evident

on the device response. In particular, it is expected that if the corners are not etched symmetrically then the self imaging conditions could be modified such that the split ratio is no longer equal.
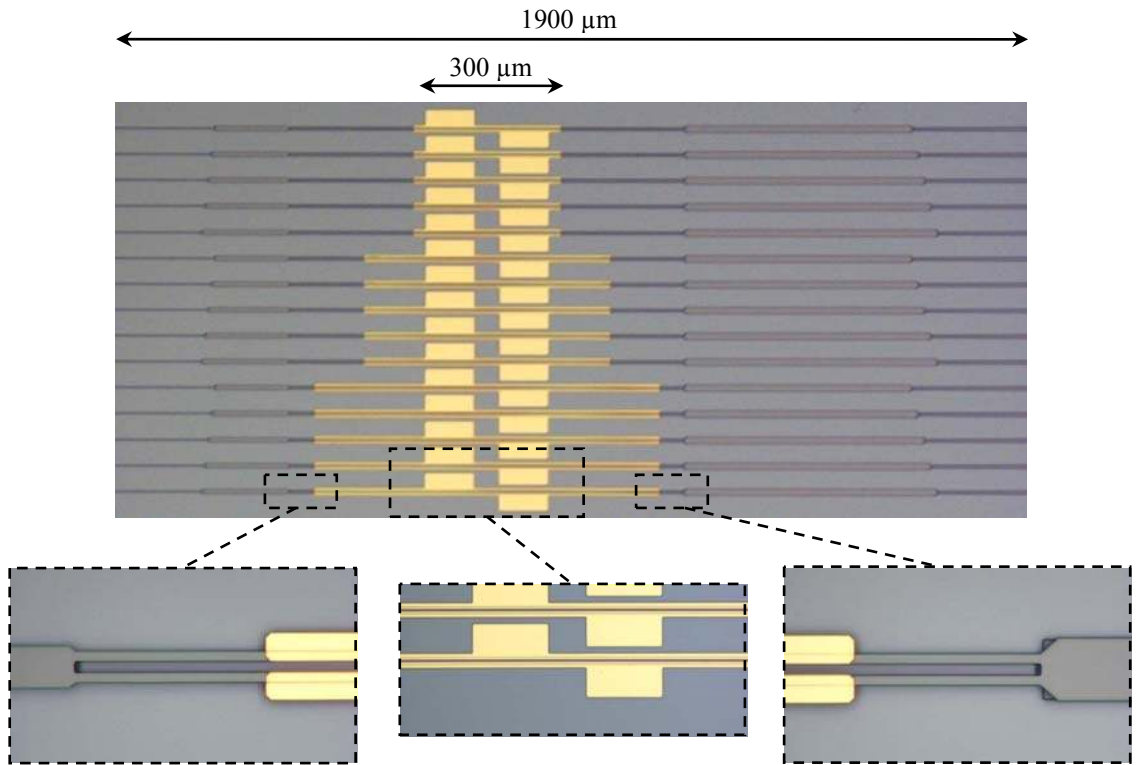
Figure 4.18 Pictures of fabricated 1x2 MZI with MMI coupler (wet chemical etching).

Owing to the shorter Zn diffusion time that was employed in the fabrication of these devices, a larger electric field is required to produce the same refractive index change. In order to compensate for this drawback, it was found that the devices with electrode lengths of 700μm performed best. The device response as a function of applied bias is shown in Fig. 4.19 (a) for TE and (b) for TM polarizations. The main observation

is that the TM response is very similar to the TE characteristics. In both cases, there is a small offset from the zero bias position, but it is smaller for the TE case. However the ratio of the optical intensities passing through the output arms is almost the same for both polarizations when the applied bias is varied from -4V to +4V.
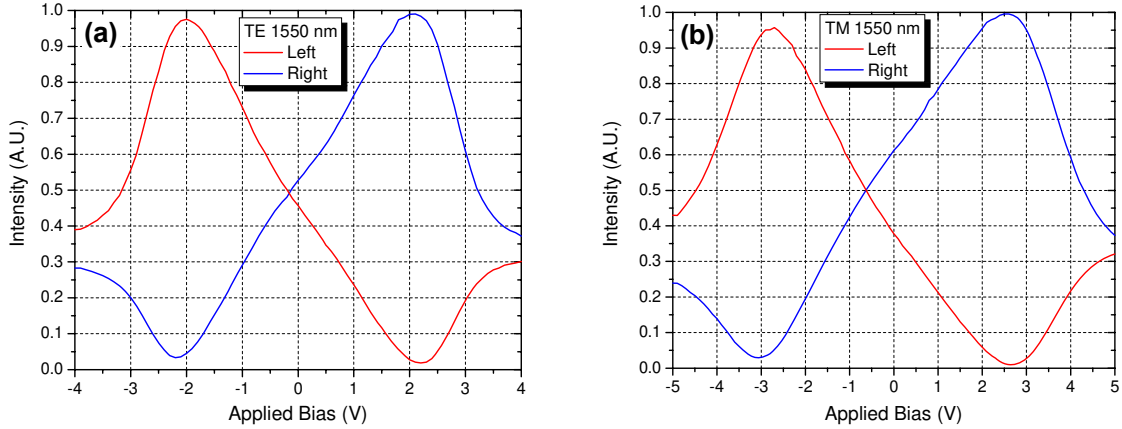
Figure 4.19 Device response as a function of applied bias for (a) TE, and (b) TM polarization.

The main difference between the responses to the different polarizations is that a higher voltage is required for full switching of the TM polarized light. This is expected because the heavy-hole exciton peak is not allowed for TM polarization and hence the refractive index change resulting from a QCSE shift of the absorption spectrum is significantly weaker than for TE polarization where the heavy exciton peak is very prominent. Fig. 4.20 (a) depicts a plot of V_π as a function of wavelength which clearly shows the higher sensitivity for TE polarizations. Fig. 4.20 (b) shows the on-chip losses as a function of wavelength. The highest on chip losses are 4 and 5 dB for TE and TM

respectively. These values are significantly lower than the on-chip losses measured for the previous MZI device formed with directional couplers and are a result of a combination of shallower zinc diffusion depth, wider waveguides (3 µm instead of 2µm), and the absence of waveguide bends. It can also be noticed that the spectral dependence of the TE losses are shaped by the MMI wavelength response, with the lowest value between 1550 and 1560 nm. The MMI response for the TM signal is shifted to shorter wavelengths, which explains the higher on-chip losses.
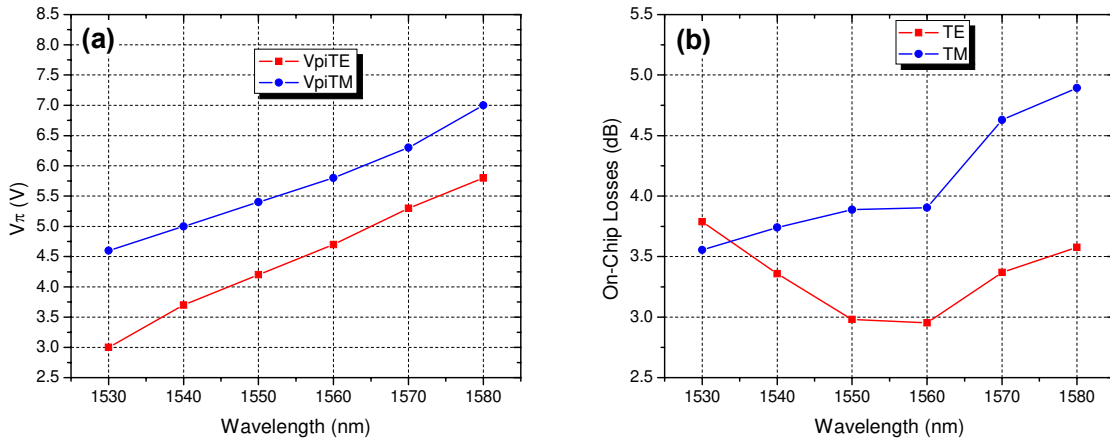
Figure 4.20 (a) V_π voltage, and (b) On-chip losses as a function of wavelength.

Fig. 4.21 (a) shows the extinction ratios of the device for the TE and TM polarizations signal. Although the device performance for the TE mode is basically similar to the one obtained for the previous device shown in Fig. 4.14 (a), the extinction ratio for TM polarization is significantly improved at around -20 dB. Crosstalk measurements were also performed and are shown in Fig. 4.21 (b) indicate that the TM

polarization actually gave a better device performance owing to the smaller offset and less electro-absorption.
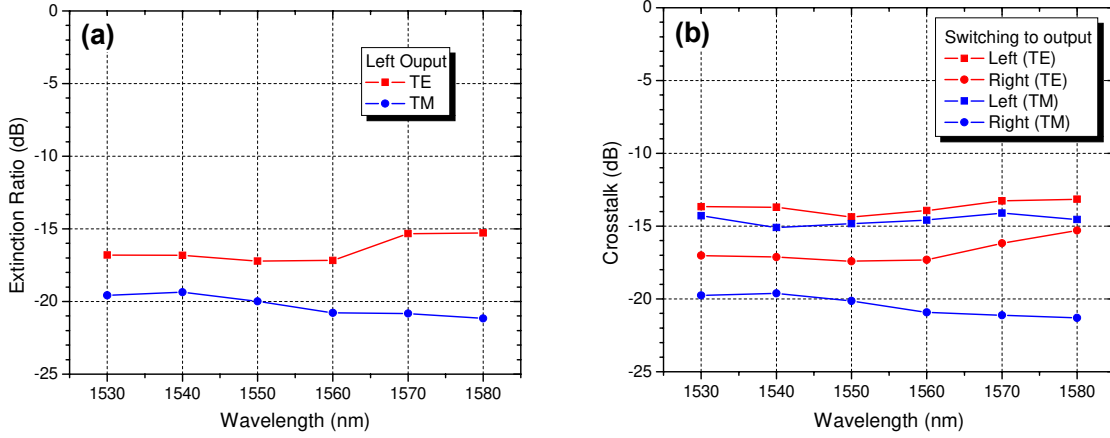
Figure 4.21 (a) Extinction ratio, and (b) Crosstalk as a function of wavelength.

In this particular device the limiting factor appears to be caused by the deviation from a 50:50 power split by the MMI device. This is most likely due to the non-right-angled corners of the MMI splitter and coupler resulting from the wet chemical etching of the InP. The main issue in our current structure is that we are operating in the most sensitive part of the MZI characteristic curve, and the device becomes very susceptible to small departures in symmetry. If the device is operated at the bottom or top of the sinusoidal response curve, the device should in principle be even more robust and tolerant to fabrication issues.

4.3 2x2 Mach-Zehnder Interferometer

By replacing the first 1x2 MMI splitter with another 2x2 MMI coupler the structure is modified into a 2x2 MZI switch. The new structure is shown in Fig. 4.22. In this configuration light launched into the upper port will exit at the lower port, and vice-versa. When a π phase shift is applied to either arm of the interferometer, the light is switched to the opposite port. Thus the device can be operated as a 2x2 switch, or as a digital modulator.

3-dB MMI Coupler   3-dB MMI Coupler

P-type contacts.
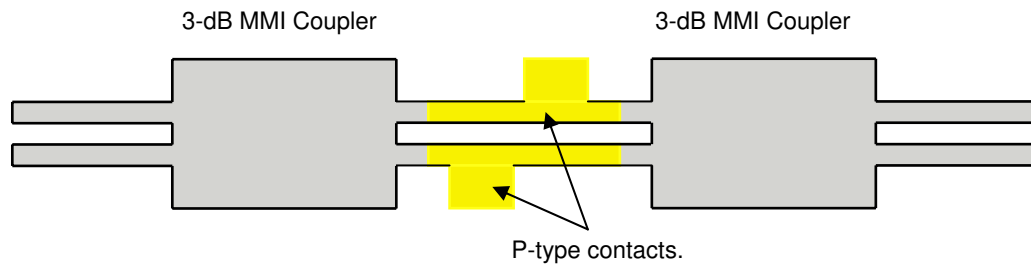
Figure 4.22 Schematic of 2x2 MZI switch with MMI couplers.

A photograph of the fabricated 2x2 MZI switch is shown in Fig. 4.23. The fabrication process is identical as with the previous device, and the diffusion time was also 27 min. The only difference is that the semiconductor waveguide structure was dry etched. As it can be seen in the close-ups photographs, the input and output MMI couplers are identical, and the 90º corners are well defined as a result of the dry etching.
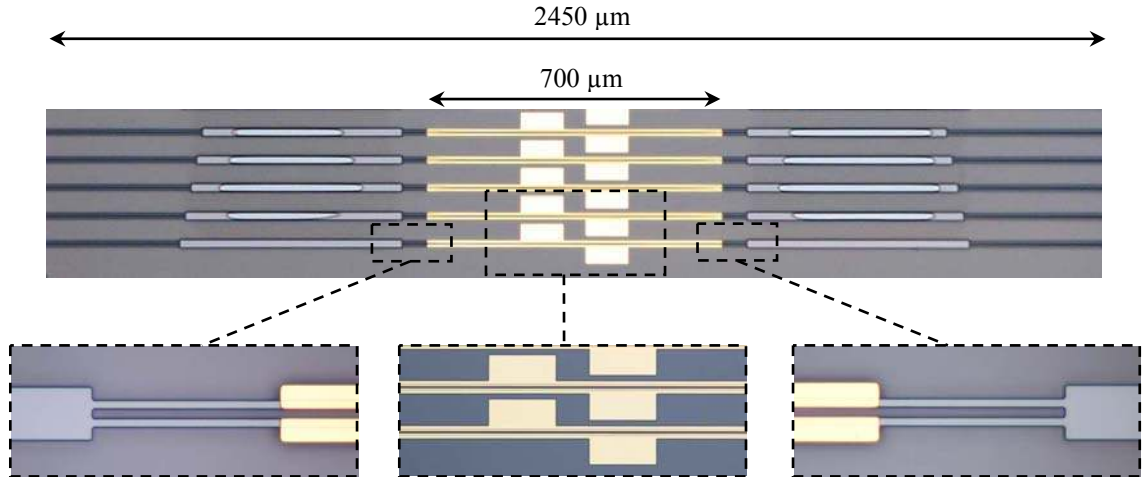
Figure 4.23 Pictures of fabricated 2x2 MZI with MMI couplers (dry etching)

4.3.1 Experimental Results

Fig. 4.24 (a) shows photographs of the output facet of the 2x2 MMI-MZI device with light initially launched into the right input channel. The top picture with no bias applied to the device clearly shows that the light is fully transferred to the left channel, with the crosstalk being only -20 dB. When the right arm is reverse-biased, the light is switched back to the right channel. Unfortunately, as shown in Fig. 4.24(b), the optical power transferred to the right channel does rise significantly above 50% transmission. This is attributable to the electro-absorption effects that become quite significant at about the 3V bias that is required to induce a π phase shift for complete switching. As a result, crosstalk in the on-state is significant, and the device cannot be used as a voltage controlled switch.
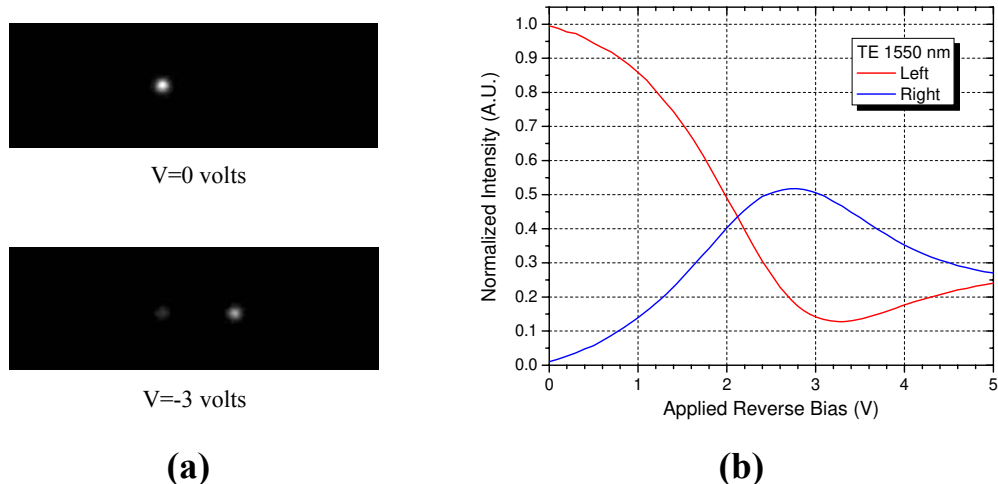
Figure 4.24 Near field pictures at different applied bias (Left), and Device response as a function of applied reverse bias (Right).

Nevertheless, for modulation purposes, we can take advantage of the low crosstalk exhibited during the off-state and only monitor the modulated signal going through the right output channel. An average extinction ratio of 15 dB is obtained from 1530 nm to 1560 nm as shown in Fig. 4.25. This value is achieved at an applied reverse bias of 2.5 volts for both TE and TM polarizations. We should note that operating in this mode imposes an additional 3-dB of insertion loss since the output power does not rise well above 50% transmission. On the other hand, the extinction ratio, and switching contrast can be further improved if the required phase shift could be achieved with minimum increase in absorption. Carrier induced refractive index changes typically are not accompanied by significant changes in absorption and therefore that mechanism is ideally suited for this application In order to confirm our theory, the device was operated

81

by current injection using a current driver instead of the voltage driver, and the results are shown in Fig. 4.26. Full switching is achieved in this case with a current level of only 8 mA, and crosstalk levels of -20 dB were obtained during on and off states.
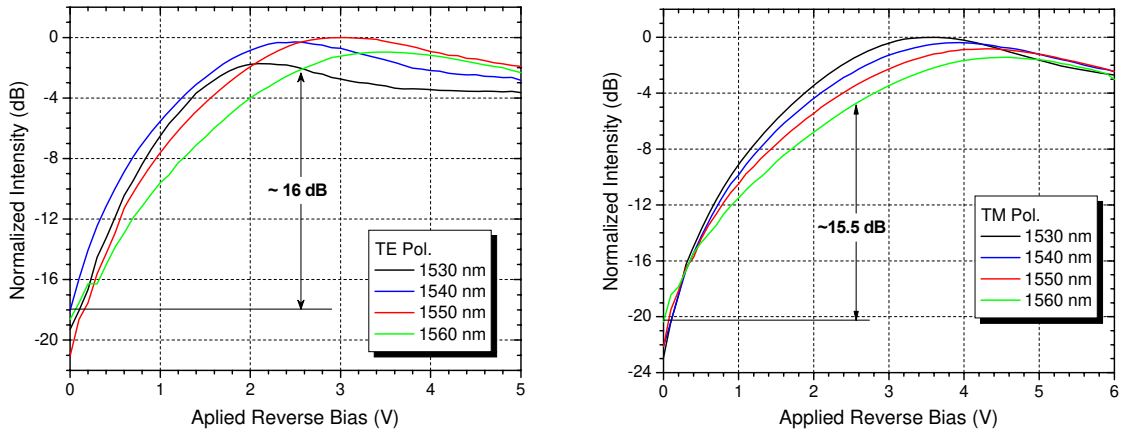
Figure 4.25 Normalized output intensity of right channel as a function of applied reverse bias for TE and TM polarization.
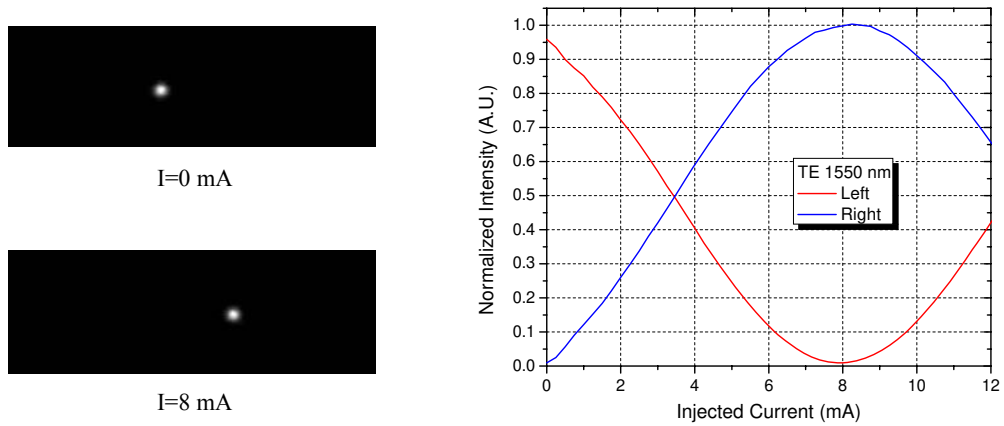
Figure 4.26 Near field pictures at different applied bias (Left), and Device response as a function of applied reverse bias (Right)

These results demonstrate that the MZI structure containing MMIs is indeed more tolerant to fabrication errors and is virtually polarization independent. Furthermore the results show that dry etching process more faithfully reproduces the designed structure and therefore leads to more accurate imaging in the MMI waveguide to produce perfectly symmetric device response . Therefore, by implementing a similar fabrication process, we could expect significant improvements on the 1x2 MZI switch. Nevertheless, the diffusion process allowed us to fully integrate the MZI devices and at the same time losses were significantly reduced by simply controlling the zinc depth.

CHAPTER 5: BEAM STEERING DEVICES

Optical beam steering devices are becoming very important because they have a wide range of applications, such as signal processing, laser scanning, and optical switches. A variety of methods have been used to achieve beam steering and they can be separated into free-space and integrated applications. MEMS devices are very well suited for free-space applications [87]. In fact, due to the maturity of MEMS technology, very efficient optical cross-connects based on MEMS beam steering are now commercially available [7, 88]. The majority of integrated beam steering devices have been demonstrated employing phase-arrayed waveguides [89-91]. A drawback of this method is that it requires the presence of a large number of phase shifting elements that must be addressed individually. Recently, a novel beam steering concept was implemented by our group using GaAs-AlGaAs material [92]. The device is very simple in comparison to phase arrayed devices, but its use was limited only to pulsed applications due to the high electrical current levels required to operate the device. When a considerable amount of current is used, thermal effects degrade the performance of the device and eventually cause the device to fail. In this chapter we demonstrate the use of our area-selective zinc in-diffusion technique to significantly reduce the current consumption of the device by optimizing the spreading of the applied current. In addition, since InGaAsP MQW are

84

used in the waveguide core, a stronger carrier-induced index change should be expected that will further reduce the electrical current required. Our experimental results show that up to a 20-fold reduction in drive current can be achieved in our device with localized Zn in-diffused p-n junctions as compared to the original planar p-i-n device. The low operating current makes it possible to drive the device continuously using d.c. currents [93-96].

5.1 Beam Steering Structure

A three dimensional view of the beam steering device is shown in Fig. 5.1. The device can be divided on two sections. The first section consists of a 2-μm wide by 500-μm long single-mode input waveguide to ensure that the laser beam is launched exactly centered between the two contact stripes. The second section is a slab waveguide region where two parallel contact stripes are used to inject electrical currents into the device. The stripes are each 800 μm long by 10 μm wide and are separated by a 21 μm gap.
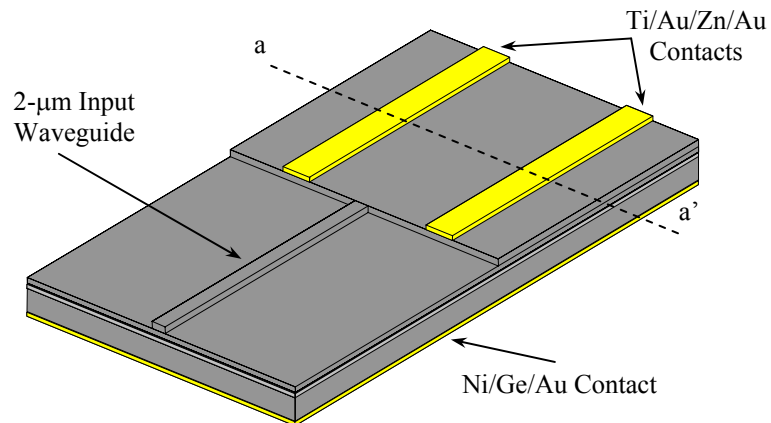
Figure 5.1 Three dimensional view of beam steering device.

The operational principle of the device is relatively simple. With no current applied to the contact stripes, a 1.55 μm wavelength laser beam that is launched into the input waveguide expands into a slab mode after propagating between the parallel electrodes. However, when electrical currents are applied through the two contact stripes, the optical properties of the slab waveguide are modified due to the carrier-induced index change. Since current injection is required, the original structure employed a p-i-n hetero-structure as shown in Fig. 5.2, which corresponds to the cross section along a-a' in Fig. 5.1.
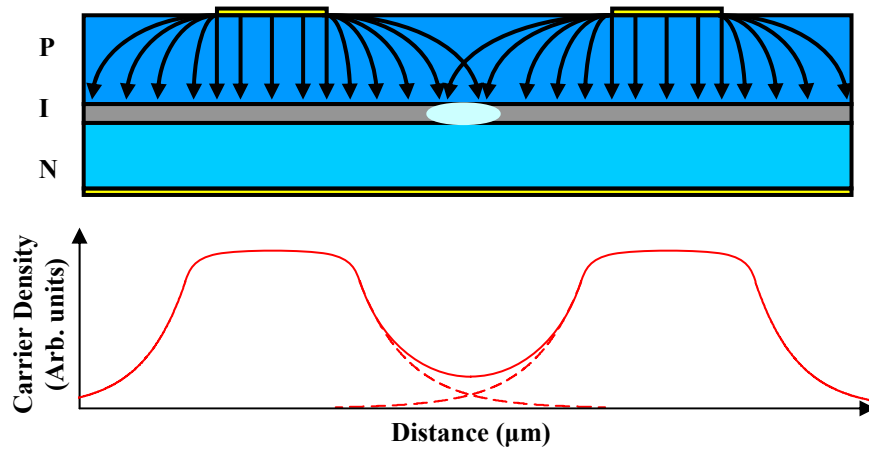
Figure 5.2 Schematic diagram of p-i-n structure under current injection.

During current injection, some lateral current spreading takes place in the resistive region lying between the contact and the MQW layer as a result of the finite conductivity of the semiconductor. The injected electrons accumulate in the MQW layer and spread sideways by diffusion. The density of injected electrons is highest in the MQW regions

directly underneath the contacts and decreases with lateral distance. The regions that are saturated with electrons experience a decrease in refractive index through the carrier-induced refractive index change. Owing to the lateral distribution of the free carriers, the portion of the MQW layer between the contact stripes will form a graded-index waveguide. With equal currents, the highest refractive index is exactly centered between the contact stripes. The lateral position of the graded-index channel waveguide follows the changes in the currents injected through the stripes. When more current is applied to the right stripe than to the left stripe, the electrons underneath the right stripe spread out more, moving the induced waveguide to the left, and vice versa. By carefully controlling the ratio of the injected currents, the induced waveguide can be shifted across the entire available range, thereby steering the guided laser beam. In the case of a regular p-i-n structure in which the whole top cladding layer is doped p-type, at very low current levels, the carriers spread out uniformly in the vicinity of the contact stripes. As the current level in each stripe is gradually increased, the finite conductivity of the p-type layer starts limiting the current spreading and causes a higher carrier density to be injected into the MQW region that is closest to the contact pads. If equal currents are injected through the two pads, the carrier density in the MQW layer between the two contacts will be lowest at the geometric center. In order for the carrier distribution to have a sufficiently sharp gradient with which to confine a waveguide mode, relatively high current injection levels (several kA/cm^2) are required [92]. Therefore, in order for the waveguiding effect to be efficient and for the device to operate with a low current density, the regions where the electrons are injected need to be set more accurately.

One way of controlling the current spreading is to diffuse zinc selectively into an n-doped cladding layer [97], in the regions beneath the contact stripes, to obtain a low resistance current conductive window in the structure, as shown in Fig. 5.3. These low resistance current conductive windows in the structure act as a channel for the injected current. Therefore, by controlling the depth of the p-doped regions, the directional flow of the current can be adequately managed and the degree of current spreading can be regulated, so as to optimize the use of the injected carriers.
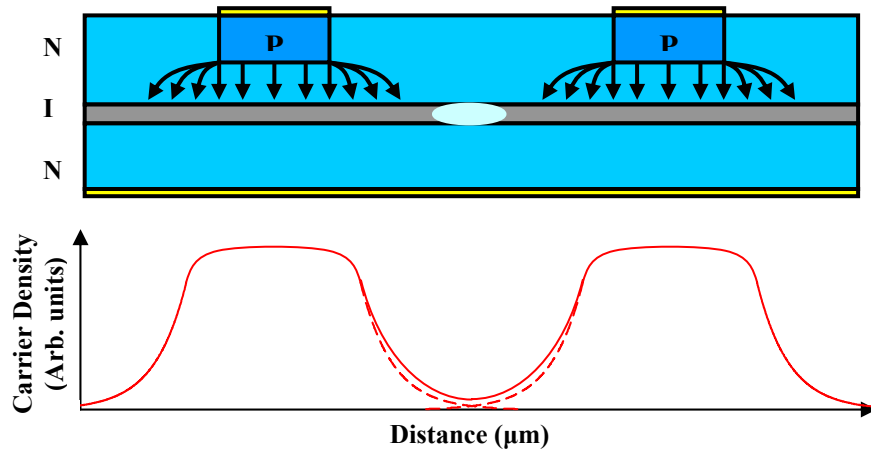
Figure 5.3 Schematic diagram of n-i-n structure (with selective zinc in-diffusion) under current injection.

5.1.1 Current Spreading Control via Zinc Diffusion

The issue of lateral current spreading and diffusion has been studied before [97-

88

99]. There are two factors that determine the final carrier density along the semiconductor waveguide structure:

1. The lateral current spreading in the resistive layer lying between the contact and the waveguiding region.

2. The lateral diffusion of carriers in the waveguiding region.

The analysis of current spreading is then realized by solving the following Laplace and carrier diffusion equations [97]:

$$-\nabla[\sigma(x,y)\nabla V(x,y)] = 0, \tag{5.1}$$

$$D\frac{d^2 n(x)}{d x^2} - B n^2(x) - \frac{n(x)}{\tau} = -\frac{J(x, y=0)}{et} \tag{5.2}$$

where σ is the conductivity, D is the ambipolar diffusion coefficient, B is the bimolecular radiative recombination, τ is the carrier lifetime, e is the electronic charge, and t is the thickness of the waveguide layer. Here $V(x,y)$ describes the potential within the semiconductor structure, and $J(x,y=0)$ represents the magnitude of the injected current density at waveguide-top cladding interface

$$J(x, y=0) = \sigma_w \frac{\partial V}{\partial y}. \tag{5.3}$$

In order to obtain an insight on the effects of zinc diffusion on the final carrier density distribution, both configurations as shown in Fig. 5.2 and 5.3 were studied. The material parameters are similar to the ones used in [97].
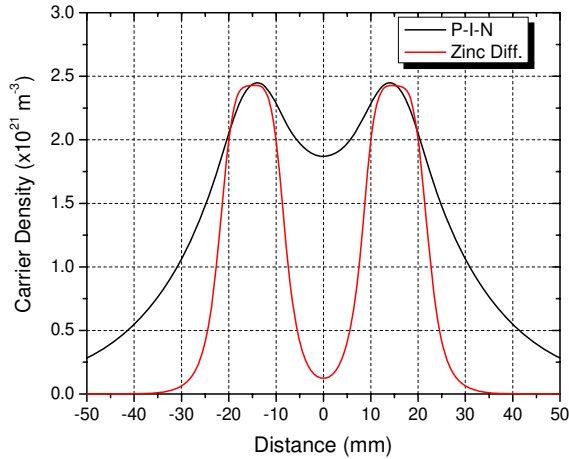
Figure 5.4 Current spreading in beam steering structure as a function of zinc depth.

The current spreading for the p-i-n structure was obtained for a current injection of 10 mA. As shown in Fig. 5.4, the p-i-n structure shows severe current spreading and the carrier density between the contacts is significant. When the zinc diffused sample is simulated (zinc depth of 0.85 µm), it is observed that the current spreading is effectively regulated. In fact, in order to obtain equal maximum carrier densities in both cases, the injected current in the zinc diffused structure has to be lowered to 3 mA. The key point is that the carrier density between the contacts in minimal, thus requiring less current to effectively form a waveguide.

5.2 Beam Steering Device Fabrication

The device was fabricated by first cleaning the sample with BOE for 2 min. to remove any native oxide, and rinsing thoroughly with DI water. A 200 nm thick Si_3N_4

film was then deposited using PECVD, Fig. 5.5(a). Conventional photolithography using Futurrex negative resist NR7-500P, followed by a CF_4 plasma etching was used to define 10 μm × 800 μm windows, Fig. 5.5(b). The Si_3N_4 film is used as a mask for the zinc in-diffusion process. The zinc in-diffusion process was then performed for the required time, Fig. 5.3(c). After the diffusion process, 15 nm of InGaAs were etched on the alignment marks using a $H_3PO_4:H_2O_2:H_2O$ (1:1:30) mixture for 10 sec. This allowed us to achieve further alignment of the following patterns on the wafer. The Si_3N_4 was then completely removed using plasma etching, Fig. 5.55(d). Ti/Au/Zn/Au p-type contacts were then patterned on the zinc diffused areas by evaporation and lift-off technique using Futurrex NR7-1000PY resist, Fig. 5.5(e). The input waveguide was then patterned by photolithography (Shipley 1805 positive resist), followed by selective wet chemical etching of the InGaAs top layer with an $H_3PO_4 : H_2O_2 :$ DI water (1:1:38) mixture. The InGaAs layer was then used as a mask for the selective wet etching of InP with an HCl : $H_3PO_4 : CH_3CHOHCOOH$ (2:5:1) mixture, Fig. 5.5(f). The etch-stop layer provided a precise control on the etch-depth, resulting in constant height InP ridges as well as a smooth etched surface. The wafer substrate was then lapped to a thickness of 150 μm and polished to a mirror finish. The n-type contact, consisting of a mixture of Ge/Ni/Au, was then deposited by thermal evaporation and annealed-in at 420 °C for 30 sec. At this point the sample was finally cleaved and mounted for the device testing. A photograph of a batch of fabricated devices is shown in Fig. 5.6.
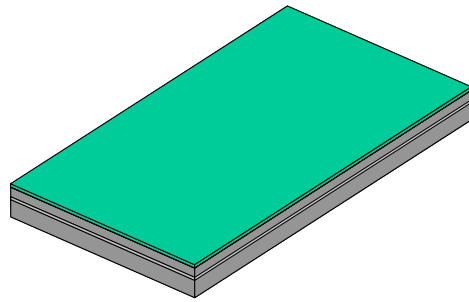
(a) Deposition of silicon nitride mask
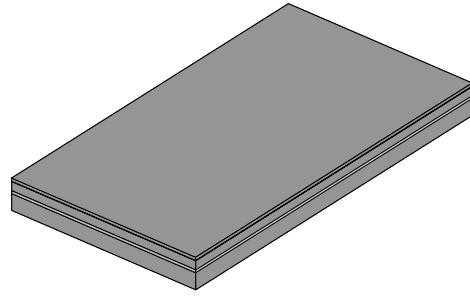
(d) Removal of silicon nitride
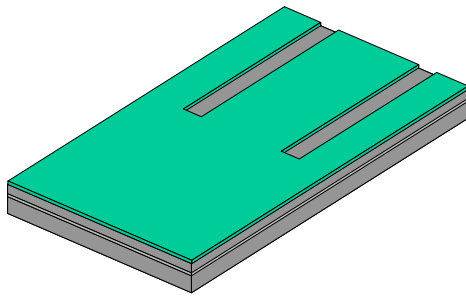
(b) Opening diffusion windows
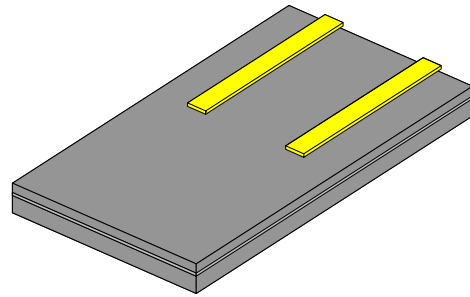
(e) P-type contact evaporation and lif-off

Heated area (500 °C)   Quartz tube

High purity
N$_2$

Semi-sealed
graphite box

Sample   Zn$_3$P$_4$
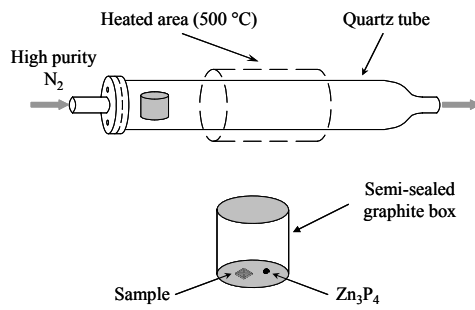
(c) Zn in-diffusion
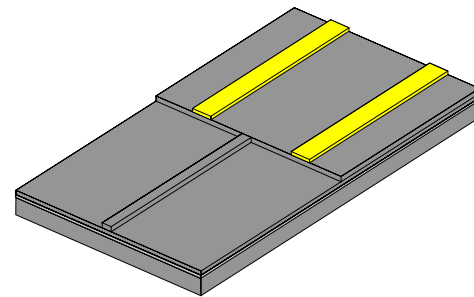
(f) Delineation of input waveguide
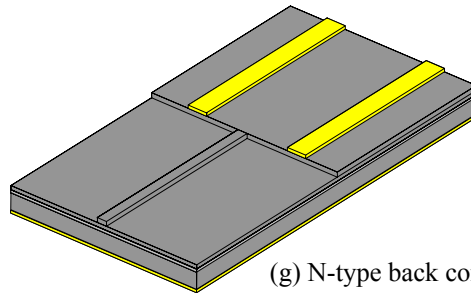
(g) N-type back contact evaporation

Figure 5.5 Device fabrication steps for beam steering device.

140 μm
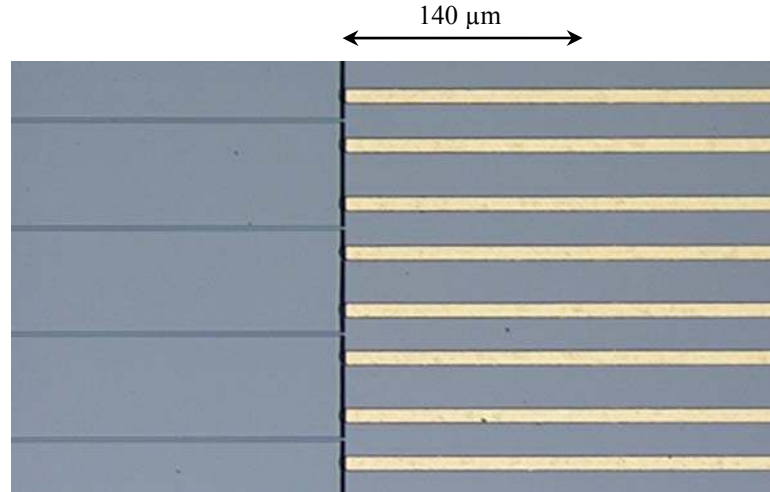
Figure 5.6 Top view picture of fabricated beam steering device.

5.3 Experimental Results

The device was tested using the experimental setup shown in Fig. 5.7. Light from a fiber pigtailed tunable laser (Agilent 8164A Lightwave Measurement System) is sent through a Mach-Zehnder modulator, and then collimated using a fiber collimator. The light is end-fired coupled to the input waveguide using a 40x microscope objective, and the output facet was imaged using a 40x microscope. A beam splitter was used to split the light so as to allow monitoring of the output facet using an infrared camera (MicronViewer 7290A from Electrophysics) and measuring the transmitted output powers using an InGaAs photo-detector (Thorlabs PDA255). Two separate laser diode drivers were used to supply the currents to the two contact stripes. Both diode drivers and the modulator can be synchronized using a pulse generator. This allowed us to test the devices under d.c. and pulsed operation.

93
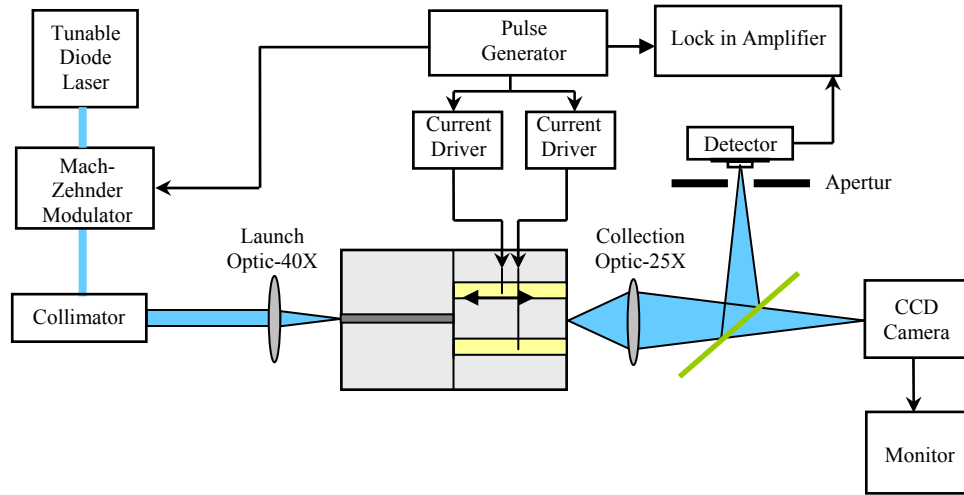
Figure 5.7 Experimental setup used for testing beam steering devices.

5.3.1 Beam Steering Without Selective Zn Diffusion

Two variants of the device were fabricated in order to appreciate the advantage of the proposed devices. In the first device zinc was diffused through the whole surface such that a p-n structure is formed at a depth of 0.8 μm. For this device, fabrication steps (a) and (b) are not considered, and fabrication stars at step (c). The optical beam steering device was characterized by first applying equal currents to the stripes in order to confine the laser beam to the center of the gap. Then the current in the left stripe was lowered while the current in the right stripe was increased, until the confined laser beam was pushed as far as possible from the center and to the left of the gap. By reversing these current values, the beam was then pushed to the right side of the gap. Finally, the currents

were adjusted to place the beam at the intermediate positions between the center and edges of the beam steering region. The electrical currents were calibrated to obtain the highest confined mode while using the lowest possible current. In order to preclude thermal effects, the device was initially tested by modulating the incoming light to produce optical pulses of 0.7 µs duration at a repetition time of 20 µs. The electrical currents that were supplied to the contact stripes were also modulated at the same frequency but with a pulse duration of 2.5 µs. The optical and electrical pulses were temporally synchronized so that the free carrier distributions were fully stabilized when the optical pulses passed through.

The device exhibited significant lateral confinement and waveguiding when the peak current through each stripe was ~190 mA. As shown in Fig. 5.8, the position of the guided spot which followed the wake of the guiding channel was easily controlled by varying the level of electrical currents through the two stripes. By passing more current to the left electrode, the waveguide was pushed to the right and consequently the output spot was guided to the right. The output spot moved to the left when more current was passed through the right electrode. The output spot could be steered through the whole 21 µm spacing between the stripes. In order to test whether thermal effects were a problem the pulse-widths of both the current pulses and the laser modulation were increased in small steps. It was observed that thermal effects started to become a problem when the current pulse-width exceeded 10 µs preventing the device from operating in d.c. mode.
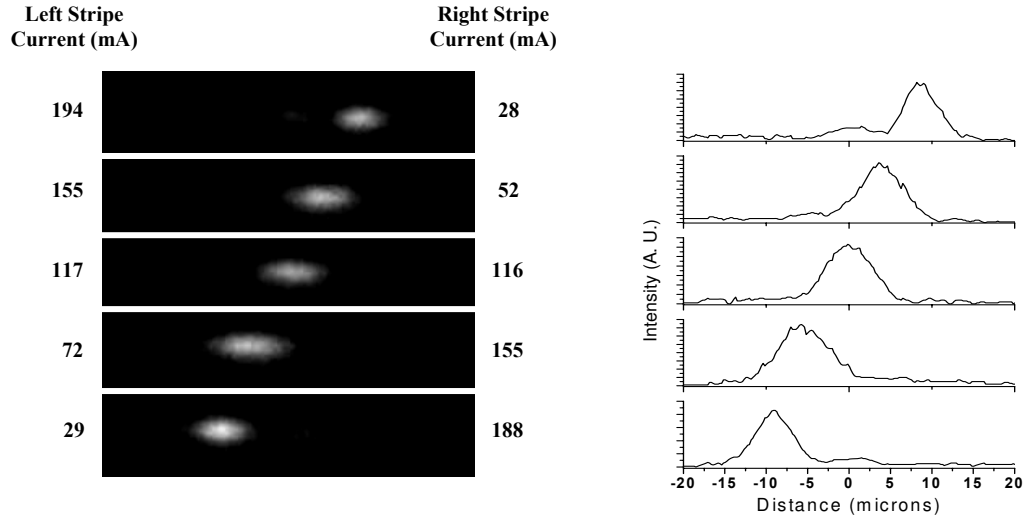
Figure 5.8 Pictures of the near-field output beams and the corresponding intensity profiles for beam steering device with zinc diffused trough the whole capping layer.

The results shown in Fig. 5.8 were taken at a wavelength of 1510 nm, which correspond to shortest wavelength that could be transmitted through without being fully attenuated by intrinsic material absorption, and also to highest carrier-induced refractive index change. The device could be operated at longer wavelengths, but the injected current increased to even higher levels. It can also be noticed that the spots are no well resolved, which can be problematic for switching applications.

5.3.2 Beam Steering With Selective Zn Diffusion

In the second configuration, zinc was selectively diffused on the position of the contact stripes. In order to determine the optimum diffusion depth, several samples with

different diffusion times ranging from 20 to 40 min in 5 min increment were fabricated. The fabrication followed exactly the process described in section 5.2.
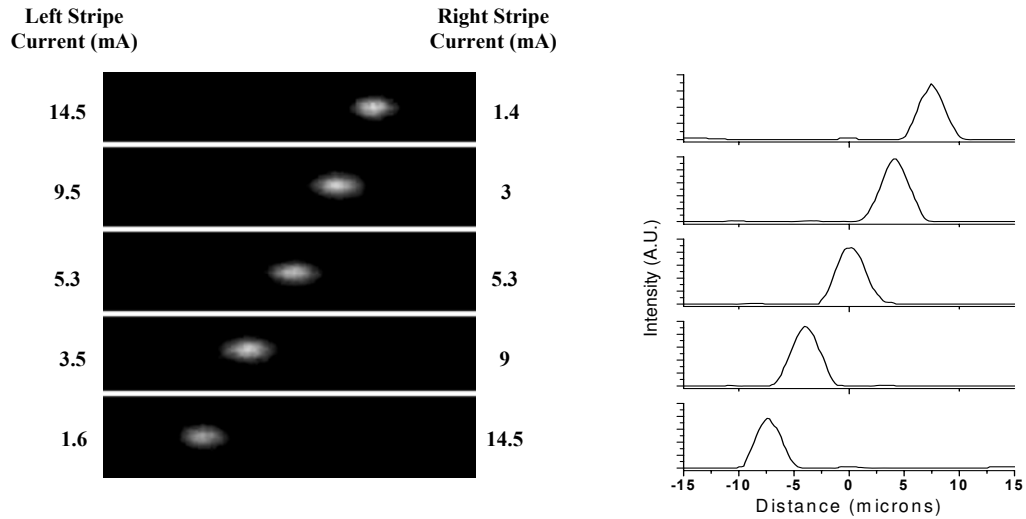
Figure 5.9 Pictures of the near-field output beams and the corresponding intensity profiles for beam steering device with zinc diffused trough the whole capping layer.

The best performance was obtained for a diffusion time of 30 min., which correspond to a zinc depth of 0.8 μm. As the laser was tuned from 1510 nm to 1625 nm, it was observed that the electrical current needed to perform the beam guiding and steering increased progressively, requiring 12.5 mA at 1510 nm and reaching 26.9 mA at 1625 nm wavelength. The beam steering results shown in Fig. 5.9 were obtained at a wavelength of 1530 nm and illustrate that, at this wavelength, the highest current needed to steer the beam to the furthest off-center position was only 14.5 mA. This represents a 17-fold reduction as compared to the previously reported work [92], and a 20-fold

reduction if the device is operated at 1510 nm wavelength. The reduction in operating current is in part due to the use of localized zinc diffusion beneath the contact stripes to control the current spreading. Additionally, the present device employs MQW in the active steering region and therefore a lower carrier density is needed to produce the same change in refractive index as compared to a bulk semiconductor counterpart. Ultimately, however, there is a minimum carrier density required to form a guided mode and to shift the induced waveguide to the edge of the steering region. This is what limits further current reduction given our present device configuration. At such low current levels, thermal effects were negligible and the device was successfully operated uncooled under d.c. current injection. This confirmed that by applying the area-selective zinc in-diffusion the current injection can be localized more accurately and the carrier spreading is only present where needed, making the device much more efficient. The results shown in Fig. 5.9 were obtained under d.c. operation. We also observed that in this device, the guided laser beam has a narrower diameter indicating that the free carrier induced waveguide is confining the light more effectively.

The wavelength dependence of the device can be better observed by fixing the injected currents for a specific wavelength, and doing a wavelength scan without modifying the applied currents. Optimum current was applied to set the output spots at the center and edge position at 1530 nm wavelength, and the wavelength was scanned up to 1590 nm. Peak position and full width half maximum (FWHM) of the spots at each wavelength were measured. As shown in Fig. 5.10 (a), the wavelength dependence of the center position is very low for both peak position and FWHM, at least for the first 40 nm

(1570 nm wavelength). Beyond 1570 nm, although the peak position barely changes, the FWHM increases almost 1 μm.
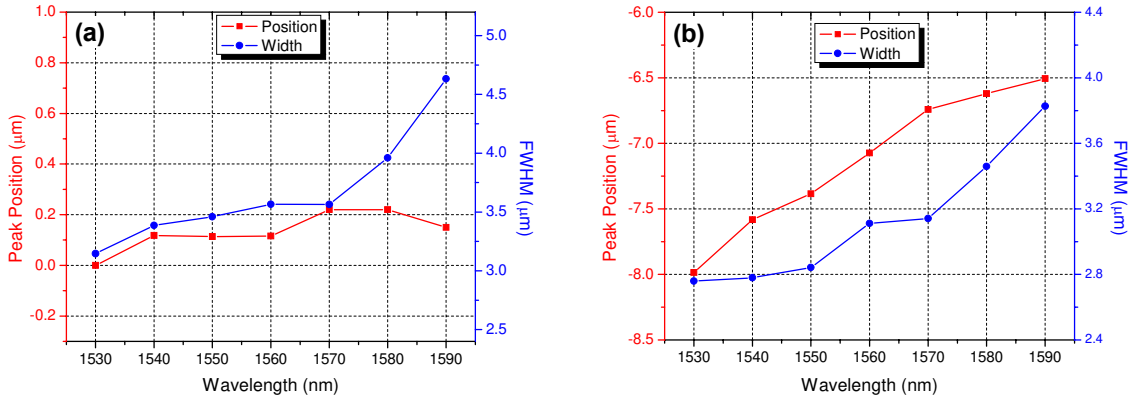
Figure 5.10 Wavelength dependence of beam steering device for output spot at (a) center and (b) edge positions with injected current optimized at 1530 nm wavelength
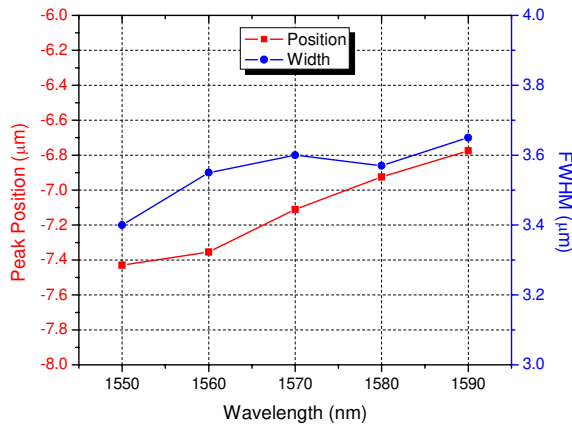
Figure 5.11 Wavelength dependence of beam steering device for output spot at edge position with injected current optimized at 1570 nm wavelength.

At the edge position the situation is completely different with both peak position and FWHM increasing almost immediately as the wavelength is changed. Since an ideal wavelength independent device requires the same bias for any given wavelength, this can be minimized by setting the optimum injected currents at the middle of required wavelength range. A range of 40 nm was selected, with the center wavelength at 1570 nm. As shown in Fig. 5.11, there is slight wavelength dependence, but the value is decreased as compared to the previous results for both peak postion and FWHM.

Although there might different potential applications for this beam steering device (recently it was used in an integrated tuning laser configuration [100]), our main goal is the realization of photonic switches. In the following section, a 1x3 photonic switch is implemented based on our beam steering configuration.

5.4 Reconfigurable 1x3 Switch

Optical cross-connects (OXCs) are important components for future optical networks because they can provide efficient routing functionalities. Several OXCs have been demonstrated using different platforms. In fact, OXCs based on MEMS devices are now commercially available [88, 101]. In the case of planar lightwave circuits, OXCs are most commonly implemented by interconnecting a large number of photonic switches [102-104]. A more promising approach is to cascade several 1xN photonic switches in order to achieve NxN operation, since a device with a smaller footprint can be obtained in this manner [105, 106]. The realization of a versatile and compact 1xN switch becomes critical in this case, as it will ultimately determine the complexity and size of the OXCs.

In this section we demonstrate a versatile 1x3 photonic switch based on our beam steering device.
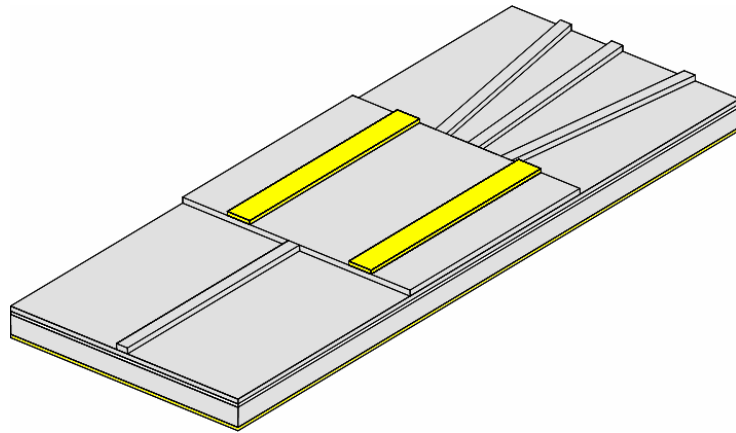
Figure 5.12 Schematic of 1x3 photonic switch.

The proposed 1x3 switch is shown in Fig. 5.12. It can be sub-divided into the beam steering section and the output waveguide ensemble. The beam steering section is similar to the one previously described. The three output waveguides constitute the second section and are each 3-μm wide by 500-μm long. Initially each output waveguide is separated by 3-μm, with the separation increasing to 6-μm at the output facet. The operation is really simple, and switching is accomplished by steering the launched optical beam and redirecting it to any one of the three output waveguides. The device is fabricated following the same procedure as for the beam steering device. The only difference is that the output waveguides are fabricated at the same time when the input waveguide is etched, Fig. 5.5 (f). A photograph of the fabricated 1x3 photonic switch is shown in Fig. 5.13. Also shown are close-ups of the input and output waveguides.
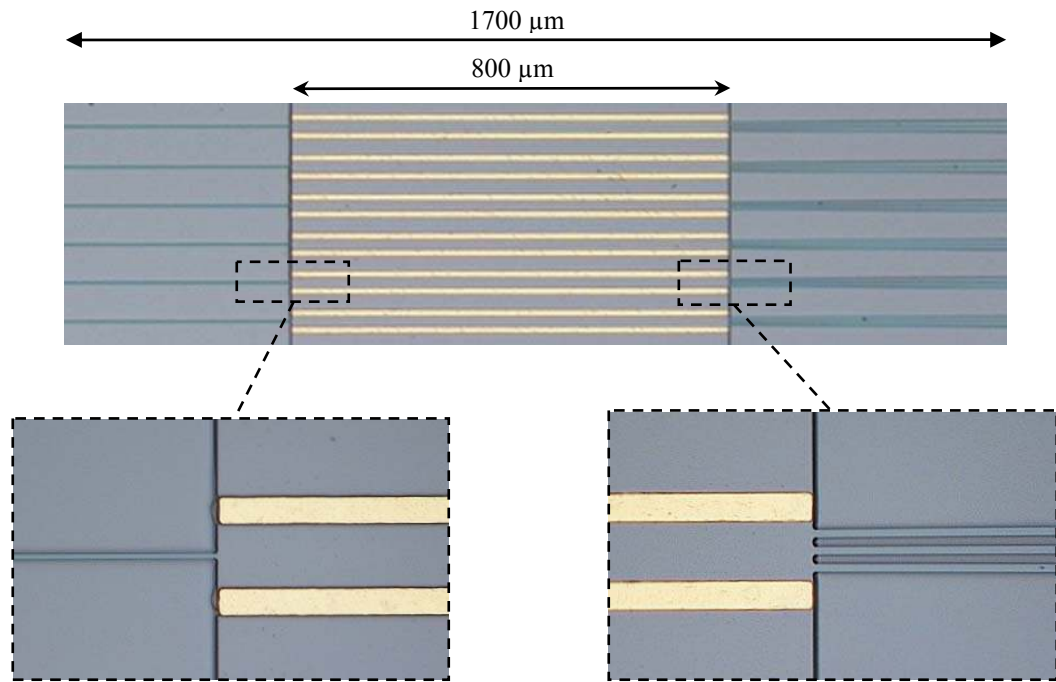
Figure 5.13 Pictures of fabricated 1x3 photonic switch.

The device was tested using the same experimental setup for testing the beam steering devices (Fig. 5.7). The only variant was the use of a 40x microscope objective, instead of the 25x, to facilitate measuring the crosstalk between the output channels. As shown in Fig. 5.14, when only 3.8 mA and 3.9 mA of current were applied to the contacts respectively, the light is equally split to the three output waveguides. By properly unbalancing the applied currents, the light can be easily switched to any of the output waveguides. The results in Fig. 5.14 were taken at a wavelength of 1565 nm, which will be the center wavelength of the operating wavelength range. Since the maximum required

current was on the order of 21 mA, we were able to operate the device without the need for any cooling mechanism.
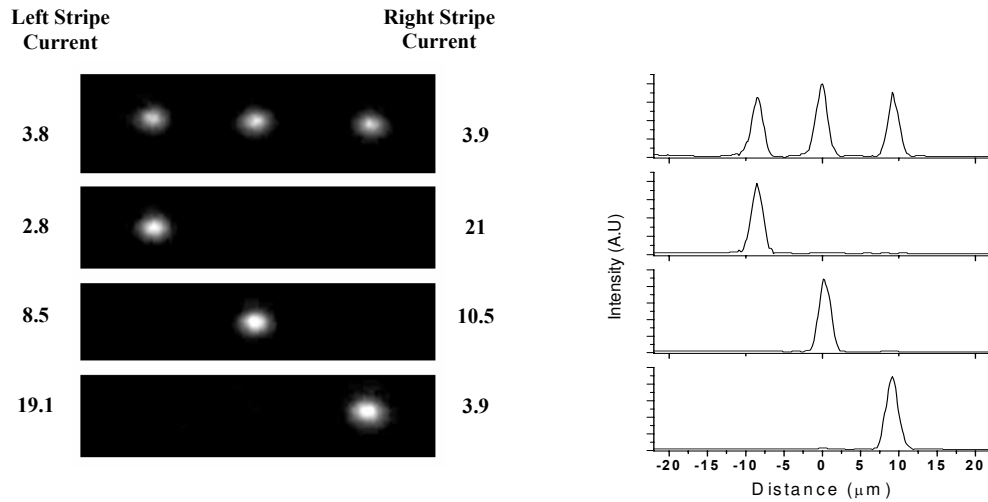
Figure 5.14 Pictures of the near-field output beams and the corresponding intensity profiles for the 1x3 photonic switch.

As shown in Fig. 5.14, the applied current values required to direct the laser beam into the various output waveguides of the 1×3 photonic switch were higher than those used for the beam steering subunit. These higher currents are attributed to the fact that the beam steering section was optimized to achieve maximum steering with the lowest possible currents, not to achieve any predetermined confinement specification. In contrast, the current values selected for directing the laser beam to the individual output waveguides of the 1×3 switch were optimized to reduce the crosstalk. Therefore, higher currents were necessary in order to achieve a more confined mode. The approach employed in measuring the crosstalk required determining the current values needed to direct the laser beam to each of the three output waveguides, which are shown in Fig.

5.14. Then the photo-detector was positioned at the first output waveguide and the light intensity was measured when the light was switched to each one of the three output channels. The measurement was performed for different wavelengths within the selected wavelength range. The photo-detector was moved to the next output waveguide and the process repeated until all three channels had been likewise evaluated.
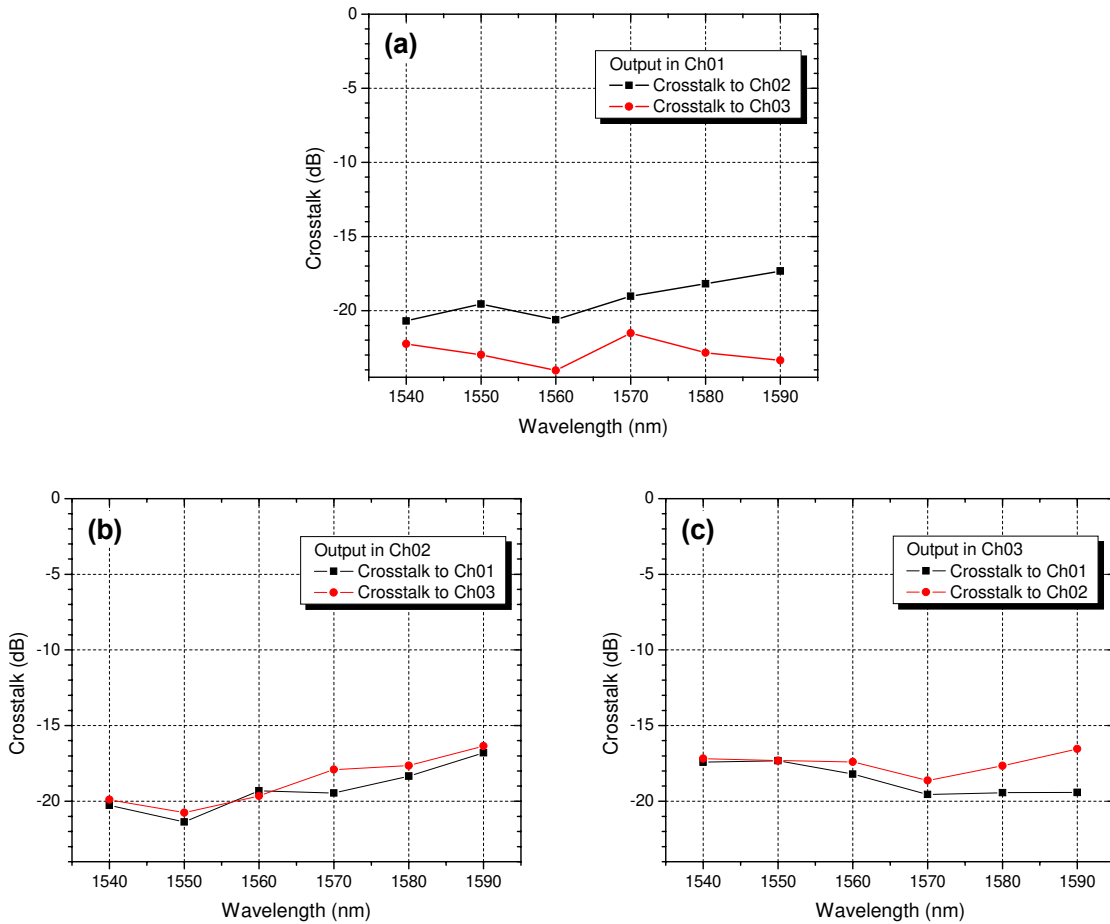
Figure 5.15 Crosstalk between channels as a function of wavelength.

As shown in Fig. 5.15, crosstalk levels better than -17 dB could be obtained over a range of 50 nm, with a center wavelength of 1565 nm. This crosstalk level is easily obtained for light switched to either channel. If the wavelength range is decreased, it is possible to further reduce the crosstalk, and also the required current is reduced. The on-chip insertion loss of the device was measured for both center and edge steering position. The average insertion loss at the center was 3.299 dB, increasing only to 3.682 dB when the light is steered to the edge position.

5.5 1x4 Photonic Switch

A 1x4 switch was also fabricated, as shown in Fig. 5.16, by simply adding an additional output waveguide.
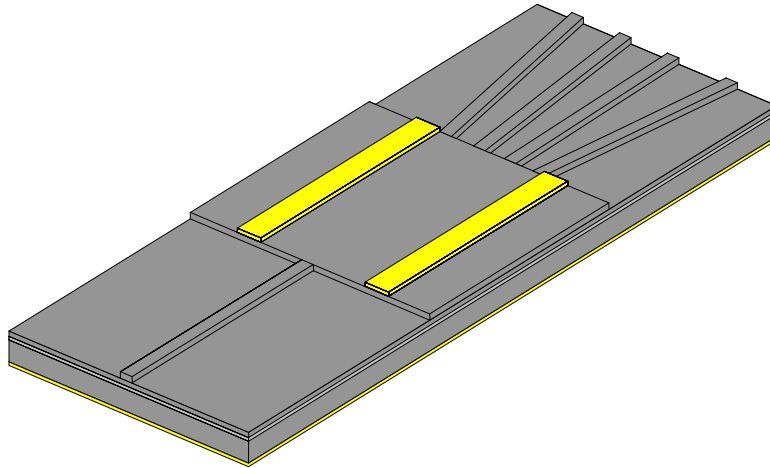
Figure 5.16 Schematic of 1x4 photonic switch.

In this structure, the separation between contacts was 22 μm as measured from the

inner edge of each stripe. Each one of the output waveguides is 4 μm wide and has a length of 500 μm. Initially each output waveguide is separated by 2 μm, but as they spread out from the beam steering region, this value increases to 5 μm at the output facet. Fabrication process is similar to the 1x3 switch.

Experimental results are shown in Fig. 5.17. As can be seen the applied current values required to direct the laser beam into the various output waveguides of the 1×4 optical switch are slightly higher than those used for the 1x3 switch. These higher currents are attributed to the fact that the outer output waveguides were placed beside the contacts stripes. Therefore, even with a minimum amount of current the light was pushed away from the waveguide, and higher current was required from the other contact pad to keep the light on the output waveguide. A crosstalk between channels of −10 dB was initially measured for this device.
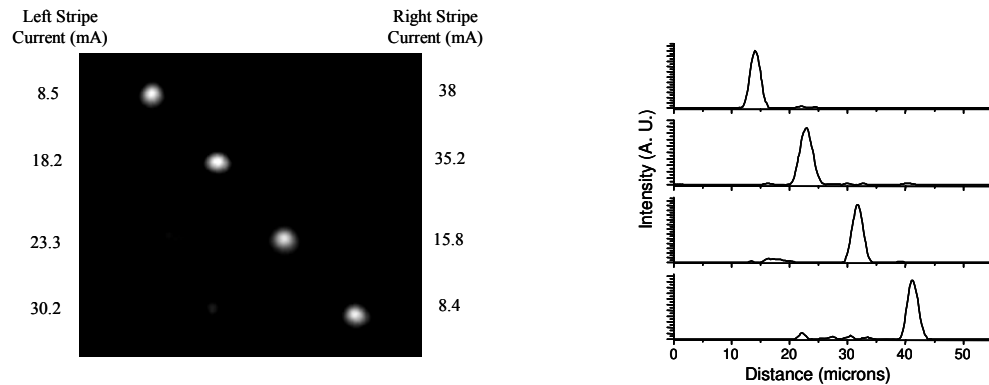
Figure 5.17 Pictures of the near-field output beams and the corresponding intensity profiles for the 1x4 photonic switch.

106

When the crosstalk is measured only for the inner two outputs, the crosstalk is better than -19 dB. We believe that further optimization of the device design and better control of the fabrication process will lead to significance improvement in the crosstalk. Nevertheless, the results demonstrate the versatiliy of the beam steering device. Furthermore, since the device was developed on an InP semiconductor platform, integration with other photonic and electronic devices is a very attractive option to implement not only OXC's, but signal processing applications.

CHAPTER 6: MULTIMODE INTERFERENCE DEVICES

Owing to the low fabrication tolerances encountered in directional couplers, new device structures have been investigated for this purpose. An elegant solution to this problem is the use of MMI effects. The operation of a MMI device relies on a multimode waveguide that supports several modes (≥ 3). As the modes propagate along the MMI waveguide, the interference between them gives rise to the formation of self-images of the input field. By selecting the proper input field position and MMI length, devices with different functionalities can be designed. They have attracted a great deal of interest because they offer several advantages, such as very compact devices, low polarization sensitivity, large optical bandwidths, and relaxed fabrication tolerances [85, 86]. Using this structure a variety of passive devices has been proposed and demonstrated on different substrates [107-111]. Only recently their use has been expanded from passive to active devices, and several photonic switches have been proposed using MMI effects [112-116].

In this chapter the properties of MMI structures will be explained, as well as special cases in which the MMI length can be further reduced. We also explain how active MMI devices can be designed, and we propose and fabricate novel active MMI devices using these effects [117-121].

6.1 Theory of MMI Devices

The analysis of MMI devices has been has been approached using different methods such as ray optics [122], BPM [123], and guided-mode propagation analysis (MPA) [85]. We follow the MPA method as explained by Soldano *et al.* [85] since it provides a better insight of the mechanism behind the MMI functionality. In general, self-imaging can be observed in three dimensional multimode structures, such as multimode fibers [124]. In the case of semiconductor waveguide structures, the transverse direction is usually single mode, and the problem is reduced to two dimensions (lateral and longitudinal).

In this method, the input field $\Psi(y,0)$ at z=0 (Fig. 6.1) is decomposed into all the guided modal field distributions $\psi_\nu(y)$ that are supported within the MMI waveguide,

$$\Psi(y,0) = \sum_{\nu=0}^{m-1} c_\nu \psi_\nu(y),$$ (6.1)

where the coefficient c_ν is estimated by obtaining the overlap integral for each mode,

$$c_\nu = \frac{\int \Psi(y,0)\,\psi_\nu(y)dy}{\sqrt{\int \psi_\nu^2(y)dy}}.$$ (6.2)

After propagating a distance *z*, the resulting field profile can be obtained by multiplying each mode in Eq. 6.1 by the proper phase term $\exp[j(\omega t - \beta_\nu z)]$. If the phase of the fundamental mode is extracted out of the sum and assuming that $\exp(j\omega t)$ is implicit hereafter, then the field at $\Psi(y,z)$ is

$$\Psi(y,z) = \sum_{v=0}^{m-1} c_v \psi_v(y) \exp[j(\beta_0 - \beta_v)z]. \qquad (6.3)$$

The difference between the propagation constants $(\beta_0 - \beta_v)$ can be approximated as [85],

$$(\beta_0 - \beta_v) \cong \frac{v(v+2)\pi}{3L_\pi}, \qquad (6.4)$$

with L_π is defined as the beat length between the two lowest-order modes

$$L_\pi = \frac{\pi}{\beta_0 - \beta_1} \cong \frac{4n_0 W_e^2}{3\lambda_0}$$

where W_e is the effective multimode waveguide width, n_0 is the effective refractive index, and λ_0 is the vacuum wavelength.

Therefore, using Eq. 6.3 and 6.4 the propagated field at $z=L$ is expressed as,

$$\Psi(y,L) = \sum_{v=0}^{m-1} c_v \psi_v(y) \exp\left[j\frac{v(v+2)\pi}{3L_\pi} L \right]. \qquad (6.5)$$

It is clear that the phase factor plays a key role for self-imaging formation. If $\Psi(y,L)$ will be a image of $\Psi(y,0)$ then the phase factor has to be

$$\exp\left[j\frac{v(v+2)\pi}{3L_\pi} L \right] = 1 \qquad \text{or} \qquad (-1)^v. \qquad (6.6)$$

This imposes two conditions for the formation of *single self-images*. The first one requires that all the modes should experience a 2π phase shift after propagating along L, thus producing a direct replica of the input field. The second is that the phase differences between the modes must alternate in even and odd multiples of π, with the even and odd

110

modes in phase and antiphase respectively. Therefore, the self-image will be mirrored with respect to $y = 0$, which should not be a concern for symmetric input fields as in the case of single mode waveguides. Both conditions are satisfied at distances given by

$$L = p(3L_\pi) \qquad with \qquad p = 0,1,2,....$$ (6.7)

which is shown in Fig. 6.1. Along the way between the input and the single self-images, *multiple images* are also formed at distances determined by

$$L = \frac{p}{N}(3L_\pi),$$ (6.8)

where $p \geq 0$ *and* $N \geq 1$ are integers with no common divisor [125]. An important aspect of these multiple images is that they have a relative phase difference, and this phase relationship needs to be kept constant for proper formation of the following set of images.
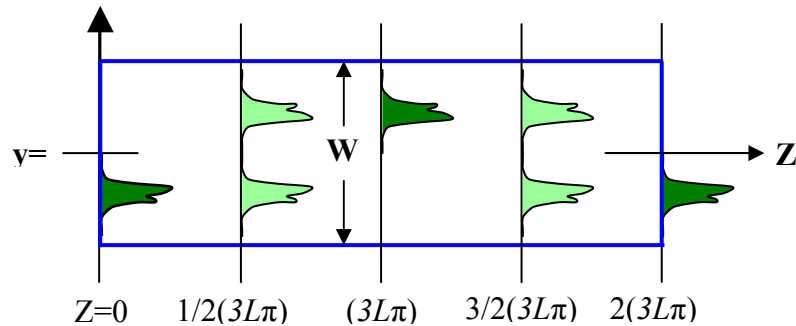
Figure 6.1 Schematic of a multimode waveguide showing the formation of mirrored single images and two-fold images and two-fold images.

Using these simple expressions very short devices can be designed. However, in integrated optics there is always a need for smaller devices. If we can selectively excite

111

certain modes within the MMI waveguide, the MMI length can be reduced. This is limited to two special situations, but important for some applications as we will find later on.

6.1.1 Restricted Symmetric Interference

The simplest case is obtained when a symmetric input field (fundamental mode) is launched exactly at the center of the MMI waveguide. In this case, only the even modes will be excited, and the resulting self-images will be a linear combination of the even modes. The resulting single images in this case will be formed at one fourth of the distance calculated in Eq. 6.7 [110], with a more general expression of N-fold images given by

$$L = \frac{p}{N}\left(\frac{3L_\pi}{4}\right).$$
(6.9)

Due to the symmetry of the interfering fields, the position of the resulting images along the y-axis will be also symmetric with equal spacing of W_e/N.

6.1.2 Restricted Paired Interference

If a symmetric input field is launched at $y = \pm W_e/6$, at this position the modes $\nu = 2,5,8,...$ present a zero with odd symmetry with respect to this point. Therefore, the

overlap integral between the input field and these modes will vanish. As a result, only the first two of every three modes are excited, and the length of the self-images is reduced by one third [126]. Single images are found at $L = p(L_\pi)$, with a more general expression for N-fold images given by

$$L = \frac{p}{N}(L_\pi).$$ (6.10)

Although this situation can only be used for two positions, it is very useful for the design of 2x2 MMI devices.

6.2 Active MMI Devices

The main application of MMI structures has been as passive devices in various integrated optical circuits for the splitting or combining of optical signals. There is great interes in developing active MMI devices, in particular photonic switches, because they can be very robust devices. In general, active MMI devices can be obtained by perturbing the conditions required for self-images to occur at the predicted locations, such as changing the phase relation between the multiples images and selective mode perturbation.

6.2.1 Phase Relation of Multiple Images

As previously explained, the phase of each set of multiples images has to stay constant for the next set to be properly formed. If we selectively modify the phases in a

113

particular set, then the phases and lateral positions of the following sets of images will be modified. With the right parameters this effect can be used to develop photonic switches. To develop an NxN switch, the N phases formed at the middle of the MMI have to be known. At this length, we basically have an NxN splitter as shown in Fig. 6.2.
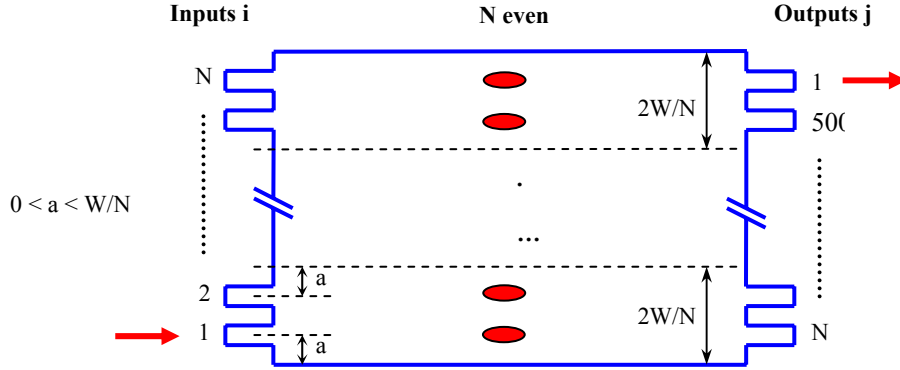
Figure 6.2 MMI coupler illustrating NxN operation for the case of N even inputs.

In this case, light launched into any of the N inputs will be equally splitted into N images, but the relative phases of these N images will be different for each input waveguide. The expressions for calculating the phases of the N images are [125],

$$i + j \ even, \ \varphi_{ij} = \pi + \frac{\pi}{4N} * (j - i)(2N - j + i) \tag{6.11a}$$

$$i + j \ odd, \ \varphi_{ij} = \frac{\pi}{4N} * (j + i - 1)(2N - j - i + 1). \tag{6.11b}$$

Knowing the phase value of each of the N images for each input, light coupled to any given input can be switched to any output by properly modifying these N phases. For example, light launched to input one will exit at output one, with the N images having a

114

specific phase relation. If this phase relation is modified such that it replicates the phase relation obtained when light is launched at input N, then the light will be switched to output N.

6.2.2 Selective Mode Perturbation

In a general MMI the phase shift between symmetric and antisymmetric modes is an odd multiple of π and the image will be inverted as shown in Fig. 6.1. If a phase shift $\Delta\phi = \pi$ is introduced between the symmetric and antisymmetric modes, the image experience a further inversion and the image will be formed at the other side of the ouput plane.
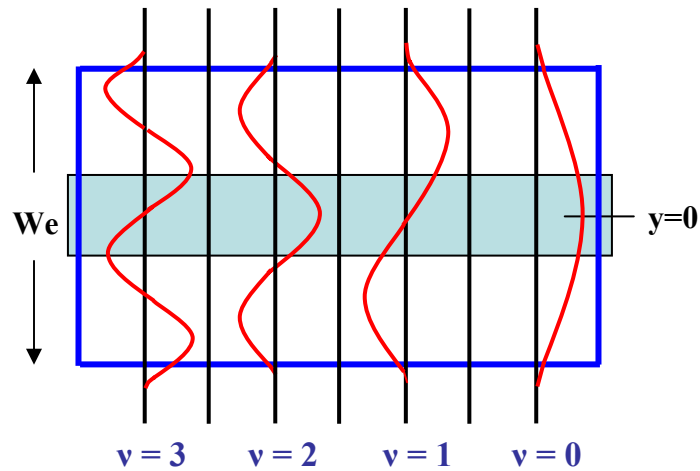
Figure 6.3 Schematic demonstrating selective mode perturbation.

This phase shift can be induced by modifying the refractive index as shown in

Fig. 6.3. The even modes experience a stronger index change because they have a maximum at this location. In contrast, the odd modes have a zero which reduces the overlap with the perturbed zone. This effect was recently used to propose a 2x2 photonics switch [114].

6.3 Compact MMI Modulator

As we explained in chapter 4, one of the issues related to MZI modulator is that the extinction ratio can be increased due to imbalance between the intensity of the arms. In MQW devices this effect is related to electroabsorption due to the QCSE. Here we propose an ultra-compact MMI-based InGaAsP MQW optical modulator which is very tolerant to electroabsorption issues. The device operates by restricting the coupling of the light to a single mode waveguide as in the MZI. However, rather than interfering two different beams, the device relies in mode conversion of the modes within the MMI, which relaxes the effects of electroabsorption.

6.3.1 MMI Modulator Structure

A schematic of the proposed MMI modulator is shown in Fig. 6.4 (a). The device consists of 2 μm wide, single mode, input and output waveguides. The width and length of the MMI waveguide are 12 μm wide and 350 μm long, respectively. This case correspond to symmetric interference, and the dimensions are calculated using the same

116

MQW wafer with n_0 =3.2425 and λ=1.55 μm. The shaded area, denoted by n_1 in Fig. 6.4

(a), indicates the index modulated region with a width of 3.5 μm and shifted by a distance

of 1.8 μm, measured from the center of symmetry of the device to the center of symmetry

of the index modulated region. The operational principle of the device is very similar to

the Y-branch MZ modulator shown in Fig 6.4 (b). In the MZ modulator, light injected

into the single mode input waveguide is divided into two beams. If no phase shift is

applied, the beams recombine with the same phase and the light is coupled into the single

mode output waveguide. However, when a π phase shift is applied to one of the arms of

the MZ interferometer, the beams are recombined out-of-phase. Therefore, the electric

field distribution becomes a higher-order mode and light is not coupled into the single

mode output waveguide, effectively modulating the injected light.
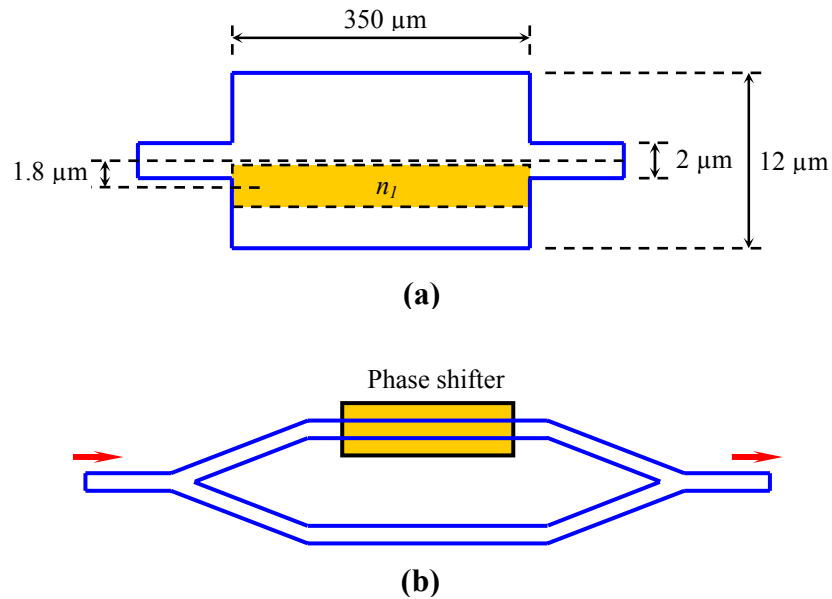
Figure 6.4 (a) MMI modulator design, and (b) Y-branch MZ intensity modulator.

In our device, modulation is also achieved by restricting the coupling of the light into the output waveguide, but in a much simpler way. Since the MMI modulator is operating under the condition of restricted symmetric interference, only the even modes are excited within the MMI waveguide. This is achieved by center-feeding the MMI region with a symmetric mode using a single mode input waveguide. This also results in a shorter device, since the distance at which the first image will be formed is reduced by a factor of four. When the index modulated region is not perturbed, there is no mode conversion, and therefore an exact replica of the input beam is produced at the end of the MMI region, and coupled into the single mode output waveguide. However, when a π phase shift is induced, as shown by the shaded region in Fig. 6.4 (a), the phase of the propagating modes is asymmetrically modified such that all the even modes are converted to odd modes. Since the output is a single mode waveguide, neither an individual mode nor any combination of the modes will be coupled, effectively modulating the propagating beam.

6.3.2 MMI Modulator Performance

The characteristics of the MMI modulator were analyzed by the FD-BPM method. The modeled structure is the one described in section 3.1. The propagation characteristics without index modulation are shown in Fig. 6.5 (a). As previously explained, the input beam propagates through the MMI region, and an exact replica of the input beam is

118

formed at the end that couples to the output waveguide. From the symmetry of the interference pattern, it is clear that only the even modes are propagating within the MMI structure. If coupling losses are not considered, a 0.3 dB insertion loss is calculated as a result of the imaging properties of the MMI waveguide.
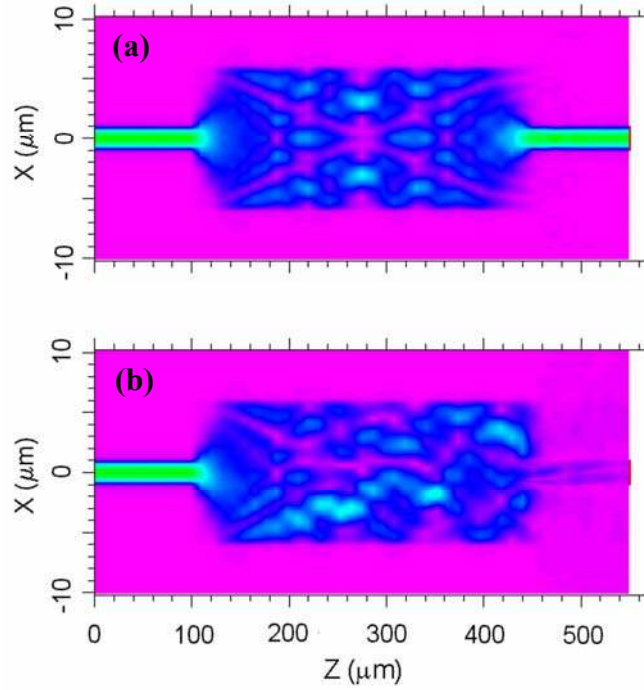
Figure 6.5 Beam propagation characteristics (a) Without index modulation, and (b) With an index modulation of $\Delta n = 1 \times 10^{-2}$.

For the case where the index is modulated, a maximum refractive index change of $\Delta n = 1 \times 10^{-2}$ is assumed in the MQW due to the QCSE [34]. In order to find the optimum width and lateral position of the index modulated region, different widths were simulated, and the lateral position was scanned from the center to the edge of the MMI waveguide.

119

From our simulations, a width of 3.5 µm and an offset of 1.8 µm, measured from the center of symmetry of the MMI waveguide to the center of symmetry of the index modulated region, provided the lowest extinction ratio (ER). The propagation characteristics when this amount of index change is induced are shown in Fig. 6.5 (b). In this case, as expected, the light is not coupled to the output waveguide and the beam is fully attenuated.

Electro-absorption effects are modeled using the ratio $\rho = \Delta n/\Delta\kappa$, where Δn and $\Delta\kappa$ are the real and imaginary parts of the complex refractive index change, respectively. This is a useful figure of merit for phase modulators because it relates the amount of index change to the induced losses. The modulator response as a function of the refractive index change (using the optimum width and offset of the index modulating region as previously calculated) when zero absorption is considered ($\rho = \alpha$) is shown in Fig. 6.6. It can be observed that an ER as low as -37 dB can be easily obtained when electro-absorption effects are not included in the simulations. As suggested by Earnshaw and Allsopp [114], values of $\rho = 50$ and $\rho = 10$, corresponding to the cases of low and high absorption modulation, respectively, were used to model the effects of electro-absorption. By using these values, a direct comparison of our device performance with other electro-refractive modulators can be obtained, since these values correspond to the upper and lower limits typically found in modulators operating by the QCSE [127].

120
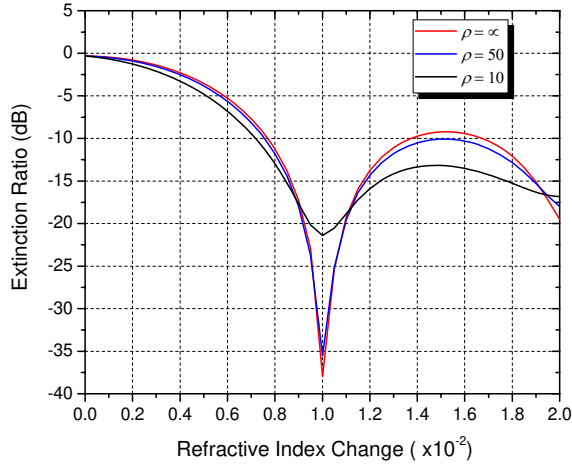
Figure 6.6 MMI modulator performance as a function of the induced refractive index change for different values of $\rho = \Delta n/\Delta \kappa$.

The characteristics of the modulator when a value of $\rho = 10$ is assumed, for the case of high absorption modulation, are also shown in Fig. 6.6. In this case, the ER is increased to -21 dB, which is still better when compared to typical MZ modulators operating under the same value of absorption modulation [114]. However, when $\rho = 50$ is used in the simulations, which is a more realistic value for the case of low electro-absorption, the change in contrast ratio is almost negligible. The modulator response for this case is also shown in Fig. 6.6, and it can be observed that the ER is only increased to -35 dB, as compared to -37 dB for the case of zero absorption. This minor change in ER is a result of both, device operation and MMI structure. The fundamental feature is to restrict the MMI structure to the regime of symmetric interference where only the even modes are excited. This allows to efficiently converting all the even modes to odd modes,

121

and therefore neither an individual mode nor any combination of the modes will be coupled into the single mode output waveguide. Since the device does not operates by modal interference, slight changes in the relative amplitude between the modes have a small effect on the modulator response.
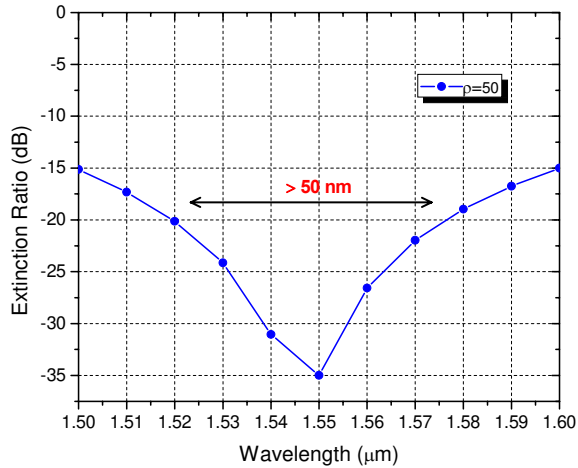
Figure 6.7 Wavelength dependence of MMI modulator for TE polarization.

The wavelength response of the modulator was also investigated. In this case, the wavelength was scanned from 1.50 to 1.60 μm for TE polarization, and the ER was obtained. As shown in Fig. 6.7, an extinction ratio of -20 dB is easily maintained over a 50 nm window. When the modulator is evaluated for TM polarization the response is significantly reduced as compared to TE polarization. This is related to the polarization dependence resulting from the waveguide structure, which provides a different overlap between the guided modes and the index modulated region for different polarizations. This can be solved by modifying our waveguide structure. Nevertheless, this

demonstrates that an ultra-compact and high contrast ratio MMI modulator is feasible using the proposed structure. The structure also requires the index modulated area to be isolated and well defined, which can be easily achieved through our zinc in-diffusion process.

6.4 2x2 MMI Switch

A different way to fabricate active MMI devices is by modifying the refractive index at specific areas within the MMI waveguide, which are collocated with the occurrence of multiple self-images. This change in the refractive index effectively alters the phase relation between the self-images, which leads to a modified output image and switches the light between the output waveguides. Using this principle several photonic switches have been proposed using MMI effects [113, 115, 116]. These configurations are of great interest, since, in principle, very efficient switching can be achieved. However, in order to have access to the large refractive index change required for switching ($\Delta n = 3 \times 10^{-2}$), the devices must rely on the principle of carrier induced refractive index change in semiconductors. Therefore, electrical current injection is required for the device operation, and this requirement imposes some restrictions on the device design. Since the index change is assumed to occur at a very precise region within the MMI waveguide, any excessive current spreading could seriously deteriorate the switching performance [115]. It is then necessary to electrically isolate the index modulated regions from the rest of the MMI waveguide. Zinc in-diffusion is particularly

attractive since it has been widely used for the fabrication of optoelectronic devices. We have also demonstrated that current spreading can be regulated by carefully controlling the zinc diffusion depth [93]. In order to restrict the current spreading as much as possible, the zinc has to diffuse to a depth that is very close to the guiding layer. The only drawback to using this approach is that, even in the absence of an injected current, an effective refractive index change is induced beneath the zinc diffused areas. This could modify the imaging conditions of the MMI waveguide, which in turn would deteriorate the crosstalk of the device. A similar effect has also been observed when using proton implantation, due to the difference in the built-in electric field between implanted and un-implanted sections [128]. Ideally, the contacts used for current injection should have the same dimensions as the index modulated regions. However, a small amount of current leakage can be expected regardless of the isolation technique. Therefore, the width of the index modulated region will always be wider than that of the contact. Consequently, the term 'contact' hereafter refers to the region that was electrically isolated, and 'index modulated region' refers to the area defined by the injected current.

Interestingly, no analysis has been previously carried out regarding the device performance as a function of the deviation from the optimum dimensions of the index modulated regions. In fact, contact width reduction might be required in order to isolate adjacent contacts, and also to achieve better definition of the index modulated regions. This, however, will create finite sections within the MMI waveguide that possess an effective index change, which can lead to deterioration of the switch crosstalk. Moreover, during device fabrication, we often have to deal with offset errors resulting from the

124

misalignment between different masking layers. Such a displacement of the index modulated regions, with respect to the optimum positioning, is potentially a very serious issue. This offset error may lead to an imbalance in the phase of the adjacent self-images, thereby making it impossible to achieve the phase difference required for switching. An error of this type would manifest as an increase in the switching crosstalk. It is therefore very important to address these issues during the design of an MMI-based switch.

In this section we propose a highly robust 2x2 MMI-based photonic switch. We demonstrate that the device is very tolerant to material modifications and typical fabrication errors. This is a result of the MMI design and the high symmetry of the switch. The waveguide structure was also modified from our original MQW structure in order to demonstrate polarization independence operation.

6.4.1 2x2 MMI Switch Design

The proposed switch is shown in Fig. 6.8. The main change to the modeled structure is that the waveguiding layer is 1 μm thick InGaAsP guiding layer ($\lambda_g = 1.3\,\mu$m) which helps to achieve polarization independence for shallow etching. If deep etching is used, this thickness can be easly reduced to ~ 500 nm [75]. The top cladding layer is a 1.5 μm thick InP top cladding layer. The refractive indices of the layers are 3.41 and 3.17 respectively. The device consists of a MMI waveguide with a width of W=18 μm and a length of L= 998 μm. Light is launched using 3 μm wide input

and output waveguides that are separated by 3 µm. The shaded zones correspond to the index modulated regions. The dimensions of the MMI switch were calculated using the well known relations for paired restricted interference in MMI waveguides. The length is then set to $L\pi$ (where $L\pi$ corresponds to the beat length) such that light coupled to the upper input waveguide will be imaged into the lower output waveguide during the off-state, as shown in Fig. 6.9 (a).
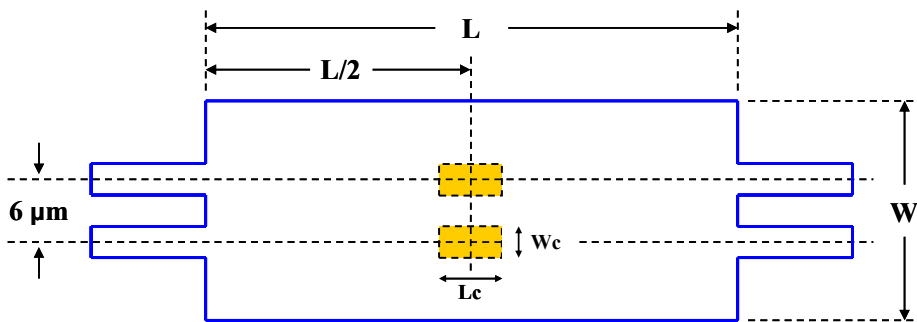
Figure 6.8 Schematic of the 2x2 photonic switch and design parameters.

The key parameter for the operation of the device is that the input light forms a pair of well defined self-images exactly at the middle of the switch, and along the central axis of both access waveguides, as shown in Fig. 6.9 (a) and (b). The index modulated regions precisely overlap the positions where these two self-images are formed. By creating identical features at these locations, any refractive index change induced in the material as a result of electrical isolation will be reflected in both self-images, and therefore the off-state output will not be altered. In the same way, offset and dimension

errors are reflected symmetrically on both self-images and the imaging is not seriously affected. It is important to note that, in the on-state, only one of the index modulated regions will be active.
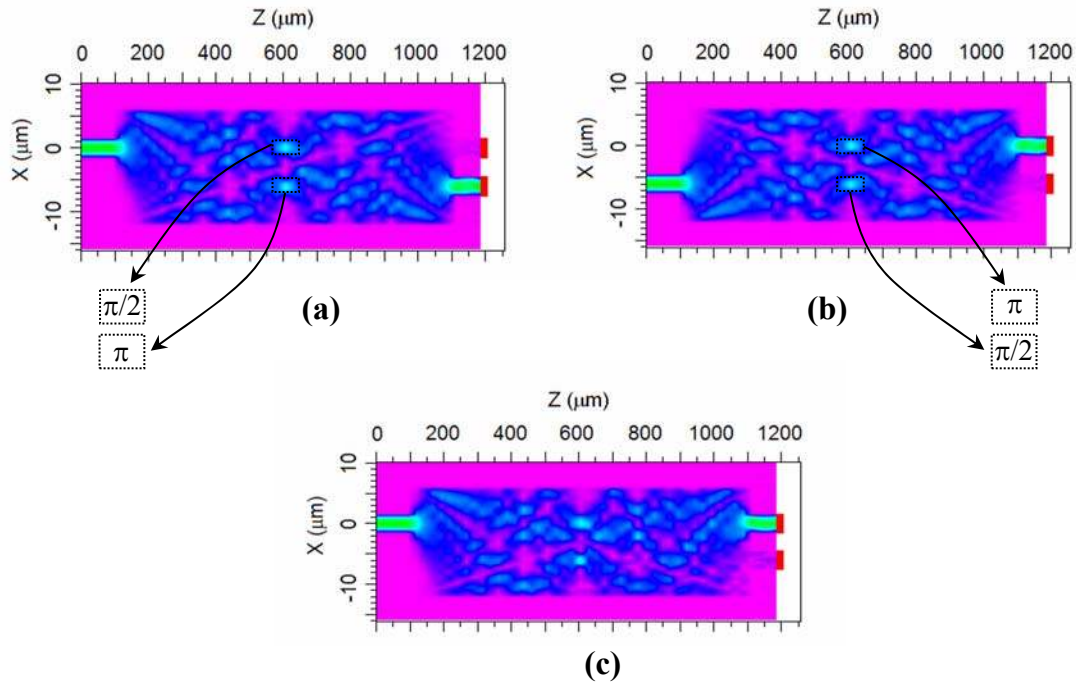
Figure 6.9 Beam propagation characteristics (a) and (b) Without index modulation, and (c) With π phase shift applied to lower index modulated region.

The operation of the switch is as follows. In the absence of an applied current, light coupled to the upper input waveguide is transferred to the lower output waveguide (and vice-versa) as shown in Fig. 6.9 (a) and (b). Also shown are the phases of the pair of images as calculated from Eq. 6.11. We can notice that in both cases there is a $\pi/2$ phase difference between the images, but the relation is inverted. Therefore, if we want to

switch the light from the lower to the upper output in the case shown in Fig. 6.9 (a), the phases have to be modified such that they replicate the phase relation shown in Fig. 6.9 (b). This is achieved by applying a π phase shift to the lower image in Fig. 6.9 (a), which results in the upper image leading the lower image by a $\pi/2$ phase difference. When this is done, light launched into the upper input waveguide will be imaged onto the upper output waveguide, as shown in Fig. 6.9 (c). A similar performance is achieved for light launched into the lower input waveguide. A maximum refractive index change of 1% was assumed as a result of current injection. This amount of index change has been theoretically and experimentally demonstrated in bulk InGaAsP semiconductors [17, 112], with an even stronger effect when multiple quantum wells are employed [129]. The dimensions of the index modulated regions were selected so as to obtain the lowest possible crosstalk for both TE and TM polarizations at a wavelength of 1.55 μm. In this case, an optimum width and length of Wc=3.5 and Lc=28 μm were calculated, respectively.

6.4.2 MMI Switch Analysis

The performance of the switch has been investigated using the FD-BPM method. In the following simulations, an induced refractive index change of $\Delta n_1 = 1 \times 10^{-2}$ was assumed for both contacts as a results of contact isolation [128]. This value is slightly higher than what we could normally expect, but it helps to demonstrate that the device is

exceedingly tolerant to such effects. We also included in the simulations the intrinsic propagation loss of 5 cm^{-1}, as well as an increase in the absorption losses for the index modulated areas due to carrier injection [112]. The analysis considered a combination of effects that can lead to deterioration of the optimum crosstalk for each switching state. Here we define the switch crosstalk as the ratio of the residual optical power on the adjacent waveguide relative to the power on the desired waveguide, expressed in decibels (dB).

During the off-state, we were mainly concerned about modifications to the imaging due to Δn_1 variance induced through contact isolation. As we explained before, reduction of the contact size might be a necessary step in keeping the injected current within the optimum calculated value for the index modulated region. However, this reduces the area that is affected by Δn_1, which could have a detrimental effect during the off-state operation. The contact width (*Wc*) was then modified from 1.5 to 3.5 μm, and the off-state crosstalk was calculated for each case. As shown in Fig. 6.10 (a), as the contact width is reduced, the induced perturbation Δn_1 stays entirely within the image, and has a negligible effect on the off-state crosstalk. In addition, we included lateral offset errors that are typically encountered during device fabrication. Currently, this value can be easily controlled within +/- 0.5 μm. Shown in Fig. 6.10 (b) is the off-state crosstalk for different contact widths as a function of the offset error along both directions. As expected, there is an increase in the crosstalk as the contact is shifted from its nominal position. However, even when the contact width is reduced to 1.5 μm, and

shifted by +/- 0.5 μm, the crosstalk is still better than -35 dB. It can also be observed that the response is more symmetric as the contact width is reduced. This is due to the fact that a narrower contact will remain within the image, even when the offset is applied. Offsetting a wider contact generates an asymmetric phase shift in the images, and therefore, the response becomes asymmetric with respect to the offset position. Unexpectedly, there is a position for Wc=3.5 μm at which the crosstalk is slightly lower than that calculated for the nominal position. Nevertheless, the selected nominal position provides the best switching performance when wavelength and polarization dependence are considered. The low crosstalk levels obtained during the off-state are a direct consequence of using wide access waveguides (3 μm) with a large separation between them (3 μm), combined with a 1 μm thick waveguiding layer.
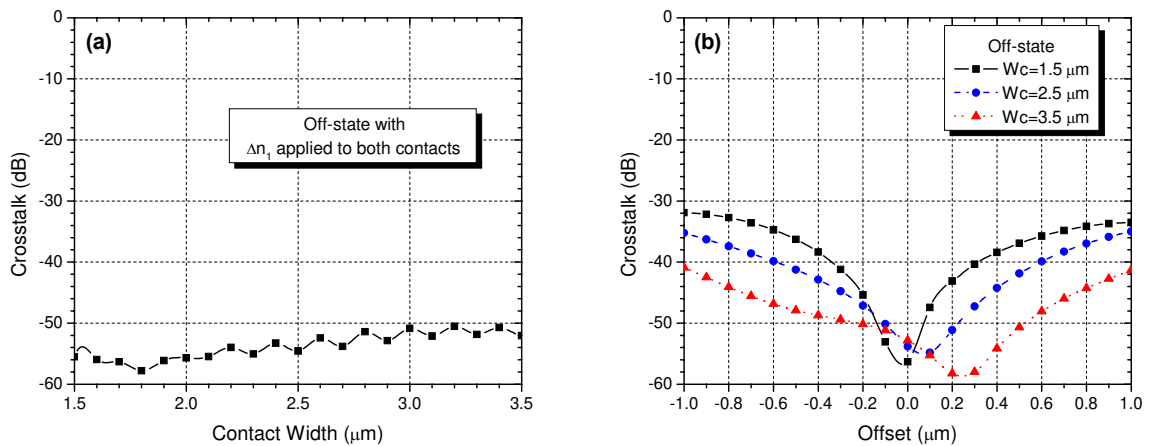
Figure 6.10 Off-state crosstalk as a function of (a) Contact width, and (b) Lateral offset for different contact widths.
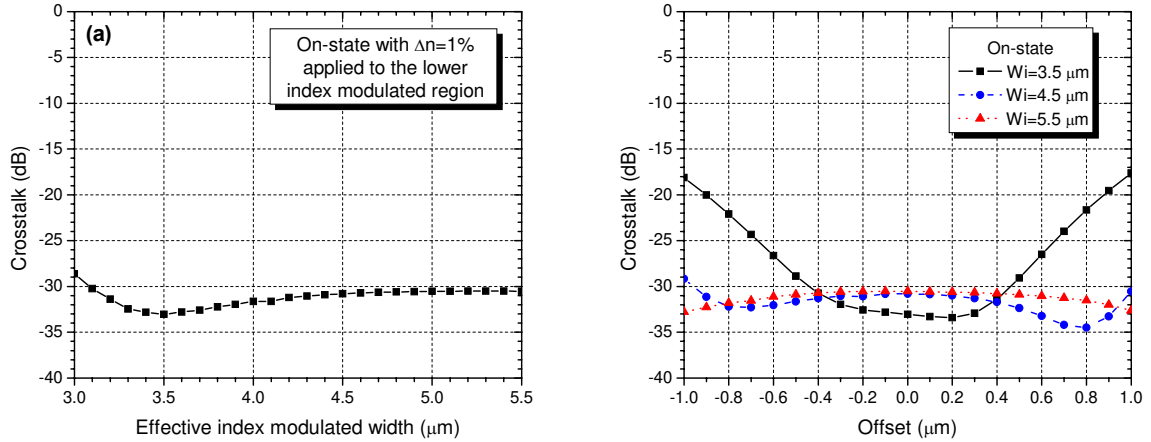
Figure 6.11 On-state crosstalk as a function of (a) Effective index modulated width, and (b) Lateral offset for different effective index modulated widths.

During the on-state, the major issue of concern is whether the injected current will be confined within the optimum index modulated region. As previously mentioned, regardless of the isolation technique, we can always expect a slight current leakage that will effectively increase the width of our contact. Therefore, it is important to determine the effects of increasing the width of the index modulation region. We define the effective index modulated width as $Wi=Wc+\Delta W$, where Wc corresponds to the optimum contact width of 3.5 μm and ΔW represents the amount of current spreading, namely 0 μm, 1 μm, and 2 μm. As shown in Fig. 6.11 (a), increasing this width has only a minor effect on the on-state crosstalk, with the value maintained below -30 dB. For completeness, the added effects of offset errors were considered, and the resulting crosstalk characteristics are shown in Fig. 6.11 (b). In this case, we can see that the device becomes less sensitive to offset errors as the width of the modulated regions is

increased. This is expected because, even though the modulated width is increased, the phase shift is still applied over the whole image whether offsets are present or not. This robustness is a direct result of the switch's high symmetry, and consequently, typical lateral offset errors can be considered negligible for this operational state.
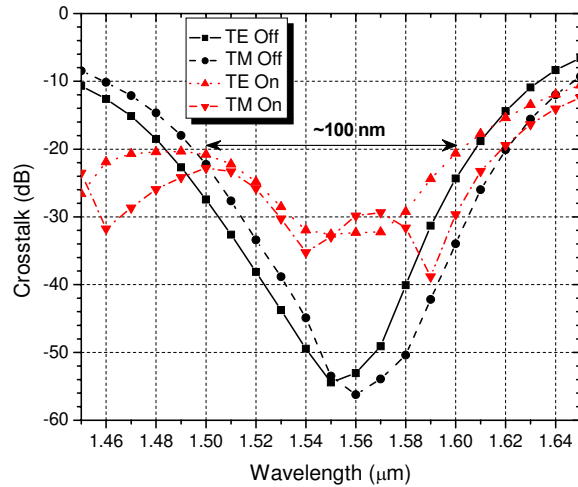
Figure 6.12 Wavelength and polarization dependence of switch crosstalk for both operation states

The wavelength and polarization response of the switch were also investigated. In this case, the wavelength was scanned from 1.45 to 1.65 μm for both TE and TM polarizations, and for both states of operation. As shown in Fig. 6.12, there is a 100 nm window within which the crosstalk can be maintained below -20 dB for both polarizations. The switching speed is initially limited by depletion of the injected carriers (typically within the nanosecond range). However, this restriction could be removed by taking advantage of the remarkable symmetry exhibited by the device. A way to

overcome the carrier lifetime limitation is to sweep out the injected carriers from the active region. This has generally been accomplished by reverse biasing the active region [130, 131]. In our device, both contacts can be reverse biased during the off-state without a major change in the off-state crosstalk, and with very low power consumption. During the on-state, one of the contacts is forward biased such that the light is switched. After the switching is completed, the contact is reverse biased so that the carriers are swept out of the active region, thus allowing a faster transition between the on and off states.

From these results, it is clear that contact dimensions can be modified as needed to optimize the index modulated region. For instance, any excessive current spreading can be mitigated by reducing the contact width without any deterioration of the switch performance. This allows the possibility of using very simple isolation techniques, such as zinc in-diffusion, for the fabrication of high performance photonic switches. Finally, it should be noted that the length of the switch can be reduced by narrowing the width of the MMI region. However, the switch becomes more sensitive to the issues that we previously discussed, and this leads to a deterioration of the crosstalk, and a narrowing of the operational window for both polarization and wavelength independence. The calculated dimensions correspond to the best device performance.

6.5 Tunable MMI Coupler

The primary focus of MMI devices has been on the development of 3-dB couplers. Even when they are highly tolerant to fabrication errors, there are always unexpected factors that can make the MMI deviate from perfect 3-dB splitting. In

addition, there are application where having different splitting ratios is necessary. In both cases a tunable coupler is the ideal device. Tunable couplers are particularly important in integrated optics because they allow the accurate setting of any splitting ratio. Such couplers are extremely useful when integrated within interferometric devices, where the splitting ratio determines the ultimate device performance.

In this section we demonstrate a tunable MMI coupler. Tuning is accomplished by modifying the refractive index at specific areas within the MMI waveguide, in a similar way as for the 2x2 switch. Since the device is operated by current injection, it is therefore necessary to electrically isolate the index modulated regions in order to regulate the current spreading within the MMI waveguide. Our zinc in-diffusion technique was employed to achieve selective-area definition of p-i-n regions. By using this technique, current spreading was effectively regulated, and an MMI tunable coupler was fabricated.

6.5.1 Tunable Coupler Design

The coupler dimensions were calculated using the MQW structure described in section 3.1. A schematic of the tunable MMI coupler is shown in Fig. 6.13. It consists of a multimode waveguide section that has a width of W=18 μm and a length of L= 504 μm. The light is launched to the device using 3 μm wide input and output waveguides that are separated by 3 μm. The shaded areas at the center of the MMI correspond to the index modulated regions. The location of these zones will be explained as follows. The

dimensions of the MMI coupler have been calculated using the well known relations for restricted interference in MMI waveguides.
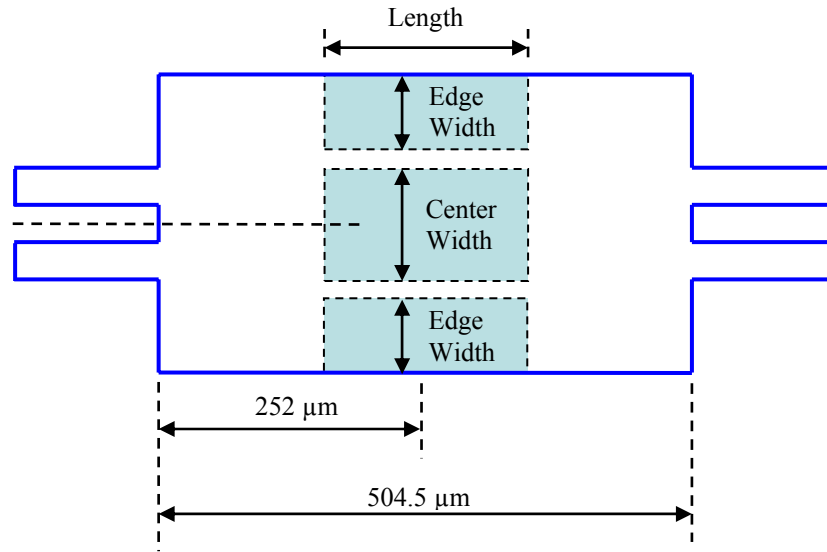
Figure 6.13 Schematic of the tunable MMI coupler and design parameters.

The dimensions of the MMI coupler are calculated such that when light is launched into either input waveguide without any external bias, the device operates as a perfect 3-dB coupler, as shown in Fig. 6.14 (a). A FD-BPM was used to study the beam propagation characteristics of the device. The formation of multiple images can also be observed at different intervals along the MMI. In this case, we will focus our attention to the four images that are formed exactly at the halfway point along the MMI length. As in the case of the 2x2 MMI switch, by modifying the phases of these four images the splitting ratio of the MMI coupler can easily be altered. The dimensions of the index

modulated regions were calculated such that the light could be switched from one output port to the other with the minimum current consumption. Optimum results were obtained using a refractive index change of $(\Delta n/n) = 0.5\%$. As shown in Fig. 6.13, a central electrode with a length of 65 μm and a width of 8 μm was calculated to provide sufficient phase modification of the two inner images. When this central contact is biased, the light is fully switched to the lower output waveguide as shown in Fig. 6.14 (b). In a similar way, edge electrodes with the same length and a 4 μm width are needed to switch the light into the upper waveguide. This is shown in Fig. 6.14 (c).
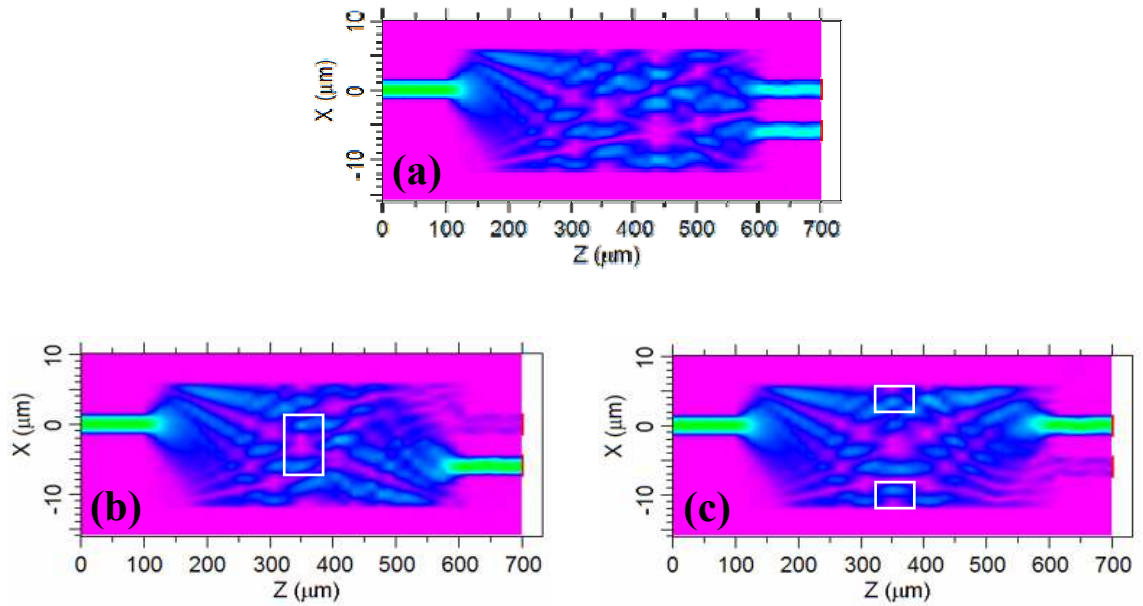
Figure 6.14 Beam propagation characteristics with (a) No applied bias, (b) Center biased electrode and (c) Edge biased electrodes.

6.5.2 Device Fabrication

The device was fabricated in a similar way as the beam steering device, and we only explain the fabrication steps. First the whole wafer is covered with a 200 nm thick Si_3N_4 film. Photolithography was then used to pattern windows on the index modulated areas, and the unwanted Si_3N_4 film was etched off using RIE. The zinc in-diffusion process was then performed during 30 min as explained in chapter 3. At this stage we completely removed the Si_3N_4 film, deposited a fresh Si_3N_4 layer, and open new windows on top of the zinc diffused areas using photolithography and RIE. This new film guarantees electrical isolation since the contact will be on top of the MMI structure. The Ti/Zn/Au p-type contacts were patterned on the zinc diffused areas by photolithography followed by evaporation and lift-off. The MMI structure was then patterned by photolithography, followed by selective wet chemical etching of the InGaAs top layer using a H_3PO_4 : H_2O_2 : DI water (1:1:38) mixture. The InGaAs layer was then used as a mask for the selective wet etching of InP using a HCl : Acetic Acid (1:6) mixture. The etch-stop layer provided a precise control on the etch-depth, resulting in constant height InP ridges as well as a smoothly etched surface. The wafer substrate was then lapped to a thickness of 150 μm and polished to a mirror finish. The n-type contact, consisting of a mixture of Ni/Ge/Au, was then deposited by thermal evaporation and annealed-in at 420 °C for 30 sec. At this point, the sample was cleaved, and mounted on a copper holder for device testing. A photograph of the top view of a fabricated batch of devices is shown in Fig. 6.15. Close-up pictures of the contacts and end sections of the MMI are also shown.

The angled corners at the end section are a result of the different etching planes inherent to the InP in acidic etchants.
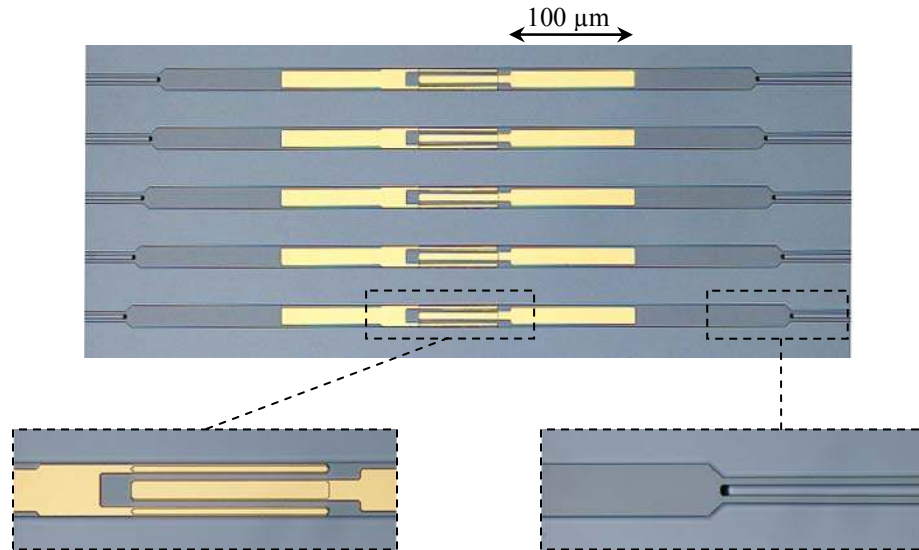
Figure 6.15 Pictures of the fabricated tunable MMI coupler.

6.5.3 Experimental Results

The devices were tested using the same setup as for the beam steering (Fig. 5.7). The normalized output intensity versus applied current characteristics of the device is shown in Fig. 6.16 (a) for 1570 nm wavelength. It can be seen that with no current applied, the splitting ratio is not exactly 50:50, but is very close to a 3-dB splitter. However, this can be tuned by injecting current into the patterned electrodes. When the edge electrodes are biased, the splitting ratio can be easily switched to better than a 90:10

138

splitting ratio. We should also note that during the first 3 mA of current injection, the splitting ratio is not modified. We believe that this is caused by a modification of the imaging due to strain from the Si_3N_4 and p-type contacts. However, as evidenced in Fig. 6.16 (a), the injection of only a small current (0.7 mA) through the center electrode is required to trim the device for an exact 50:50 split of the output powers. By increasing the applied current, the splitting ratio can be changed to a 30:70 split ratio in the other direction. After this point the behavior deviates significantly from the theoretically expected response. We believe that at this point, the injected electrons have spread too far beyond the optimum index modulated region and therefore the device stops working properly. Also shown in Fig. 6.16 (b), are pictures of the output facet for the cases of no bias applied and for the maximum splitting ratios with electrical current injected into the edge and center contacts respectively.
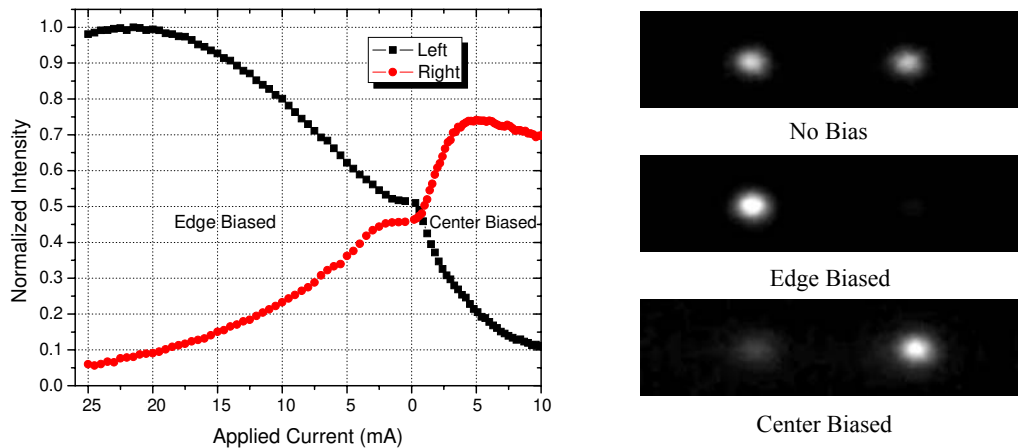
Figure 6.16 Tuning of the MMI coupler (left) and pictures of the device output facet for different biases (right).

From these results, it is clear that a couple of issues which might affect the MMI imaging need to be resolved. For instance, the angled corners that were caused by the wet chemical etching process (See Fig. 6.15) seem to adversely affect the MMI imaging. As we shown in chapter 4, this problem can easily be resolved by switching to a dry etching process. Furthermore, in our present device design the metal electrodes/bonding pads lie directly on top of the MMI region and appear to be adding a strain induced uniform index change that is shifting the position of the multiple images. As shown in Fig. 6.15, each batch of devices consisted of five different MMI lengths. When only the MMI structure was tested, without any zinc diffusion and contacts, the best imaging corresponded to the shortest device. After the whole device is completed, the best imaging was shifted to the longest device. This is a 50 μm increase in MMI length, and since the contacts are only 65 μm long, the overlapped between contacts and images was altered. This is a more serious issue, because, if the images do not overlap with the electrical injection regions, more current is required for the tuning of the output power split ratio and the performance is deteriorated. In our next device design, the metal pads will be fabricated outside of the MMI region after the device has been planarized. This requires more processing steps, but major improvements are expected in the device performance. Nevertheless, this shows the potential of our zinc diffusion process to fabricate highly functional MMI devices.

CHAPTER 7: CONCLUSIONS

An area-selective zinc-in diffusion technique has successfully been characterized for the development of photonic integrated circuits. The method is very simple yet highly controllable and reproducible. Using this technique, several integrated photonic switches in InP-based material have been demonstrated. This material system allows for the potential integration of switches and modulators with lasers and detectors, as well as very high speed electronic components.

A series of Mach-Zehnder interferometric (MZI) switches/modulators have been designed and fabricated. The diffusion process avoids the need for isolation trenches, and optical losses have been significantly reduced. A 1x2 MZI switch suitable for analog modulation has been demonstrated. Although further refinement of the wafer and waveguiding structure is required, the device exhibited good extinction ratio and low crosstalk levels. A 2x2 switch has also been fabricated. This structure proved to be more tolerant to slight fabrication errors. Extinction ratio and crosstalk levels lower than -20 dB were achieved using this structure when operated by electrical current injection.

A beam steering concept that works by electrical injection has also been demonstrated. By controlling the degree of lateral current spreading the injected currents have been optimized. This has been achieved by simply controlling the zinc depth. Beam

141

steering over a 21 μm range with electrical current values as low as 12.5 mA are demonstrated. Using this principle, a reconfigurable 1x3 switch has been implemented, with crosstalk levels better than -17 dB over a 50 nm range. As a result of the low operating currents, the devices have been operated uncooled with an applied d.c. bias.

We have also demonstrated that MMI structures can be used as active devices. In order to do so, selective refractive index perturbation within the MMI structure is required. Such elective perturbation is achieved using zinc diffusion, and operating the device with current injection. A compact MMI modulator as short as 350 μm was proposed. The main advantage of this modulator is that it is very tolerant to electro-absorption effects, since it does not rely on optical interference. A robust 2x2 photonic switch has also been proposed, and it is demonstrated that the device should be very tolerant to fabrication errors, In addition, polarization and wavelength independent operation is feasible by careful design of the wafer and waveguiding structure. Using a similar operational principle, we have demonstrated a tunable MMI coupler. To the best of our knowledge, the amount of tuning achieved has not been previously demonstrated. This is an encouraging result, since several similar integrated photonic device can be realized using similar effects.

LIST OF REFERENCES

[1]   G. P. Agrawal, "Fiber-Optic Communication Systems," *Wiley Series in Microwave and Optical Engineering, John Wiley and Sons Inc., 2nd Edition*, 1997.

[2]   O. Wada and H. Hasegawa, "InP-Based Materials and Devices," *Wiley Series in Microwave and Optical Engineering, John Wiley and Sons Inc.*, 1999.

[3]   W. S. Lee, Y. Zhu, B. Shaw, D. Watley, C. Scahill, J. Homan, C. Fludger, M. Jones, and A. Hadjifotiou, "2.56 Tb/s capacity, 0.8 b/Hz.s DWDM transmission over 120 km NDSF using polarisation-bit-interleaved 80 Gb/s OTDM signal," *OFC 2001*, vol. 2, pp. 1-4, 2001.

[4]   G. C. Gupta, L. L. Wang, O. Mizuhara, R. E. Tench, N. N. Dang, P. Tabaddor, and A. Judy, "3.2-Tb/s (40 ch x 80 Gb/s) transmission with spectral efficiency of 0.8 b/s/Hz over 21 x 100 km of dispersion-managed high local dispersion fiber using all-Raman amplified spans," *IEEE Photonics Technology Letters*, vol. 15, pp. 996-998, 2003.

[5]   T. Itoi, K. Fukuchi, and T. Kasamatsu, "Enabling technologies for 10 Tb/s transmission capacity and beyond," *ECOC '01*, vol. 4, pp. 598-601, 2001.

[6]   R. Kaiser and H. Heidrich, "Optoelectronic/photonic integrated circuits on InP between technological feasibility and commercial success," *IEICE Transactions on Electronics*, vol. E85c, pp. 970-981, 2002.

[7]   P. B. Chu, S. S. Lee, and S. Park, "MEMS: The path to large optical crossconnects," *IEEE Communications Magazine*, vol. 40, pp. 80-87, 2002.

[8]   P. De Dobbelaere, K. Falta, L. Fan, S. Gloeckner, and S. Patra, "Digital MEMS for optical switching," *IEEE Communications Magazine*, vol. 40, pp. 88-95, 2002.

[9]   T. Shibata, M. Okuno, T. Goh, T. Watanabe, M. Yasu, M. Itoh, M. Ishii, Y. Hibino, A. Sugita, and A. Himeno, "Silica-based waveguide-type 16 x 16 optical switch module incorporating driving circuits," *IEEE Photonics Technology Letters*, vol. 15, pp. 1300-1302, 2003.

[10] C. H. Jang and R. T. Chen, "Polymer-based 1x6 thermooptic switch incorporating an elliptic TIR waveguide mirror," *Journal of Lightwave Technology*, vol. 21, pp. 1053-1058, 2003.

[11] G. Aubin, J. Sapriel, V. Y. Molchanov, R. Gabet, P. Grosso, S. Gosselin, and Y. Jaouen, "Multichannel acousto-optic cells for fast optical crossconnect," *Electronics Letters*, vol. 40, pp. 448-449, 2004.

[12] S. Gosselin and J. Sapriel, "Versatile acousto-optic vector-matrix architecture for fast optical space switches," *ECOC '98*, vol. 1, pp. 253-254, 1998.

[13] N. A. Riza and N. Madamopoulos, "Compact switched-retroreflection-based 2x2 optical switching fabric for WDM applications," *Journal of Lightwave Technology*, vol. 23, pp. 247-259, 2005.

[14] B. Fracasso, J. L. D. de la Tocnaye, M. Razzak, and C. Uche, "Design and performance of a versatile holographic liquid-crystal wavelength-selective optical switch," *Journal of Lightwave Technology*, vol. 21, pp. 2405-2411, 2003.

[15] S. Akiyama, H. Itoh, T. Takeuchi, A. Kuramata, and T. Yamamoto, "Low-chirp 10 Gbit/s InP-based Mach-Zehnder modulator driven by 1.2V single electrical signal," *Electronics Letters*, vol. 41, pp. 40-41, 2005.

[16] K. Tsuzuki, T. Ishibashi, T. Ito, S. Oku, Y. Shibata, R. Iga, Y. Kondo, and Y. Tohmori, "40Gbit/s n-i-n InP Mach-Zehnder modulator with a pi voltage of 2.2 V," *Electronics Letters*, vol. 39, pp. 1464-1466, 2003.

[17] B. R. Bennett, R. A. Soref, and J. A. Delalamo, "Carrier-Induced Change in Refractive-Index of Inp, Gaas, and Ingaasp," *IEEE Journal of Quantum Electronics*, vol. 26, pp. 113-122, 1990.

[18] S. Abdalla, S. Ng, P. Barrios, D. Celo, A. Delage, S. El-Mougy, I. Golub, J. J. He, S. Janz, R. McKinnon, P. Poole, S. Raymond, T. J. Smy, and B. Syrett, "Carrier injection-based digital optical switch with reconfigurable output waveguide arms," *IEEE Photonics Technology Letters*, vol. 16, pp. 1038-1040, 2004.

[19] E. J. Murphy, "Integrated optical circuits and components: Design and applications," *Marcel Dekker, Inc.*, pp. 161-237, 1999.

[20] A. Katz, "Indium phosphide and related materials: Processing, technology, and devices," *Artech House, Inc.*, 1992.

[21] W. P. Hong, G. I. Ng, P. K. Bhattacharya, D. Pavlidis, S. Willing, and B. Das, "Low-Field and High-Field Transport-Properties of Pseudomorphic Inxga1-Xas In0.52al0.48as (0.53-Less-Than-or-Equal-to-X-Less-Than-or-Equal-to-0.65) Modulation-Doped Heterostructures," *Journal of Applied Physics*, vol. 64, pp. 1945-1949, 1988.

[22] M. A. Saleh, M. M. Hayat, O. H. Kwon, A. L. Holmes, J. C. Campbell, B. E. A. Saleh, and M. C. Teich, "Breakdown voltage in thin III-V avalanche photodiodes," *Applied Physics Letters*, vol. 79, pp. 4037-4039, 2001.

[23] B. Jalali and S. J. Pearton, "InP HBTs: Growth, Processing, and Applications," *Artech House, Inc.*, 1995.

[24] J. J. Saarinen, E. M. Vartiainen, V. Lucarini, and K.-E. Peiponen, *Kramers-Kronig relations in optical materials research*, vol. 110. Berlin, New York: Springer, 2005.

[25] C. Weisbuch and B. Vinter, *Quantum Semiconductor Structures: Fundamentals and Applications*. Orsay, france: Academic Press, Inc., 1991.

[26] H. Haug Ed., *Optical nonlinearities and instabilities in semiconductors*. New York: Academic Press, Inc., 1988.

[27] D. A. B. Miller, "Quantum well optoelectronic switching devices," *International Journal of Hihg Speed Electronics*, vol. 1, pp. 19-46, 1990.

[28] I. Barjoseph, C. Klingshirn, D. A. B. Miller, D. S. Chemla, U. Koren, and B. I. Miller, "Quantum-Confined Stark-Effect in Ingaas Inp Quantum-Wells Grown by Organometallic Vapor-Phase Epitaxy," *Applied Physics Letters*, vol. 50, pp. 1010-1012, 1987.

[29] E. E. Mendez and H. von Klitz Eds., *Physics and applications quantum wells and superlattices*. New York: Plenum Press, 1989.

[30] P. Bhattacharya, *Semiconductor Optoelectronic Devices*. New Jersey: Prentice-Hall, Inc., 1997.

[31] J. S. Weiner, D. A. B. Miller, and D. S. Chemla, "Quadratic Electrooptic Effect Due to the Quantum-Confined Stark-Effect in Quantum-Wells," *Applied Physics Letters*, vol. 50, pp. 842-844, 1987.

[32] J. E. Zucker, I. Barjoseph, G. Sucha, U. Koren, B. I. Miller, and D. S. Chemla, "Electrorefraction in Gainas Inp Multiple Quantum Well Heterostructures," *Electronics Letters*, vol. 24, pp. 458-460, 1988.

145

[33]   A. Bandyopadhyay and P. K. Basu, "Modeling of Excitonic Electrorefraction in Ingaasp Multiple-Quantum Wells," *IEEE Journal of Quantum Electronics*, vol. 29, pp. 2724-2730, 1993.

[34]   J. E. Zucker, I. Barjoseph, B. I. Miller, U. Koren, and D. S. Chemla, "Quaternary Quantum Wells for Electro-Optic Intensity and Phase Modulation at 1.3-Mu-M and 1.55-Mu-M," *Applied Physics Letters*, vol. 54, pp. 10-12, 1989.

[35]   H. Temkin, D. Gershoni, and M. B. Panish, "Ingaasp Inp Quantum-Well Modulators Grown by Gas Source Molecular-Beam Epitaxy," *Applied Physics Letters*, vol. 50, pp. 1776-1778, 1987.

[36]   C. H. Henry, R. A. Logan, and K. A. Bertness, "Spectral Dependence of the Change in Refractive-Index Due to Carrier Injection in Gaas-Lasers," *Journal of Applied Physics*, vol. 52, pp. 4457-4461, 1981.

[37]   E. Burnstein, "Anomalous optical absorption limit in InSb," *Phys. Rev.*, vol. 93, pp. 632-633, 1954.

[38]   J. G. Mendozaalvarez, R. H. Yan, and L. A. Coldren, "Contribution of the Band-Filling Effect to the Effective Refractive-Index Change in Double-Heterostructure Gaas Algaas Phase Modulators," *Journal of Applied Physics*, vol. 62, pp. 4548-4553, 1987.

[39]   D. Botteldooren and R. Baets, "Influence of Band-Gap Shrinkage on the Carrier-Induced Refractive-Index Change in Ingaasp," *Applied Physics Letters*, vol. 54, pp. 1989-1991, 1989.

[40]   L. A. Coldren, J. G. Mendozaalvarez, and R. H. Yan, "Design of Optimized High-Speed Depletion-Edge-Translation Optical Wave-Guide Modulators in Iii-V Semiconductors," *Applied Physics Letters*, vol. 51, pp. 792-794, 1987.

[41]   T. Hirao, M. Kitagawa, T. Kamada, K. Tsukamoto, Y. Yoshioka, K. Kuramasu, T. Korechika, and K. Wasa, "Effects of Deposition Methods on the Properties of Silicon-Nitride and Silicon Oxynitride Films," *Japanese Journal of Applied Physics Part 1-Regular Papers Short Notes & Review Papers*, vol. 27, pp. 1609-1615, 1988.

[42]   M. J. Madou, "Fundamentals of Microfabrication: The Sience of Miniaturization," *CRC Press, Second Edition*, 2002.

[43]   S. Adachi and H. Kawaguchi, "Chemical Etching Characteristics of (001)Inp," *Journal of the Electrochemical Society*, vol. 128, pp. 1342-1349, 1981.

[44]   K. Ikossianastasiou, S. C. Binari, G. Kelner, J. B. Boos, C. S. Kyono, J. Mittereder, and G. L. Griffin, "Wet Chemical Etching with Lactic-Acid Solutions for Inp-Based Semiconductor-Devices," *Journal of the Electrochemical Society*, vol. 142, pp. 3558-3564, 1995.

[45]   P. Elias, I. Kostic, J. Soltys, and S. Hasenohrl, "Wet-etch bulk micromachining of (100) InP substrates," *Journal of Micromechanics and Microengineering*, vol. 14, pp. 1205-1214, 2004.

[46]   Y. Nishi and R. Doering, "Handbook of semiconductor manufacturing technology," *Marcel Dekker Inc.*, 2000.

[47]   U. Schade and P. Enders, "Rapid Thermal-Processing of Zinc Diffusion in Indium-Phosphide," *Semiconductor Science and Technology*, vol. 7, pp. 752-757, 1992.

[48]   B. Tuck, "Atomic diffusion in III-V semiconductors " *Bristol [Avon]*, 1988.

[49]   G. J. Vangurp, T. Vandongen, G. M. Fontijn, J. M. Jacobs, and D. L. A. Tjaden, "Interstitial and Substitutional Zn in Inp and Ingaasp," *Journal of Applied Physics*, vol. 65, pp. 553-560, 1989.

[50]   F. C. Frank and D. Turnbull, "Mechanism of Diffusion of Copper in Germanium," *Physical Review*, vol. 104, pp. 617-619, 1956.

[51]   U. Gosele and F. Morehead, "Diffusion of Zinc in Gallium-Arsenide - a New Model," *Journal of Applied Physics*, vol. 52, pp. 4617-4619, 1981.

[52]   S. N. G. Chu, R. A. Logan, M. Geva, and N. T. Ha, "Concentration-Dependent Zn Diffusion in Inp during Metalorganic Vapor-Phase Epitaxy," *Journal of Applied Physics*, vol. 78, pp. 3001-3007, 1995.

[53]   G. J. Vangurp, P. R. Boudewijn, M. N. C. Kempeners, and D. L. A. Tjaden, "Zinc Diffusion in N-Type Indium-Phosphide," *Journal of Applied Physics*, vol. 61, pp. 1846-1855, 1987.

[54]   H. B. Serreze and H. S. Marek, "Zn Diffusion in Inp - Effect of Substrate Dopant Concentration," *Applied Physics Letters*, vol. 49, pp. 210-211, 1986.

[55]   I. Yun and K. S. Hyun, "Zinc diffusion process investigation of InP-based test structures for high-speed avalanche photodiode fabrication," *Microelectronics Journal*, vol. 31, pp. 635-639, 2000.

[56]   M. Yamada, P. K. Tien, R. J. Martin, R. E. Nahory, and A. A. Ballman, "Double Zinc Diffusion Fronts in Inp - Theory and Experiment," *Applied Physics Letters*, vol. 43, pp. 594-596, 1983.

[57]   K. H. Yoon, Y. H. Lee, D. H. Yeo, and S. J. Kim, "The characteristics of Zn-doped InP using spin-on dopant as a diffusion source," *Journal of Electronic Materials*, vol. 31, pp. 244-247, 2002.

[58]   C. Lauterbach, "Zinc Diffusion in Inp from Spin-on Films of Various Zinc Concentrations," *Semiconductor Science and Technology*, vol. 10, pp. 500-503, 1995.

[59]   M. Ogihara, M. Taninaka, and Y. Nakamura, "Open tube zinc diffusion into GaAs0.8P0.2 using AlN and SiNx cap films," *Journal of Applied Physics*, vol. 79, pp. 2995-3002, 1996.

[60]   J. Wisser, M. Glade, H. J. Schmidt, and K. Heime, "Zinc Diffusion in Inp Using Diethylzinc and Phosphine," *Journal of Applied Physics*, vol. 71, pp. 3234-3237, 1992.

[61]   T. H. Weng, "A comparative study of p-type diffusion in III-V compound semiconductors," *Proceedings Electron Devices Meeting*, pp. 120 - 122, 1997.

[62]   F. Riesz, L. Dobos, and J. Karanyi, "Thermal decomposition of bulk and heteroepitaxial (100) InP surfaces: A combined in situ scanning electron microscopy and mass spectrometric study," *Journal of Vacuum Science & Technology B*, vol. 16, pp. 2672-2674, 1998.

[63]   A. Katz, W. C. Dautremontsmith, S. N. G. Chu, P. M. Thomas, L. A. Koszi, J. W. Lee, V. G. Riggs, R. L. Brown, S. G. Napholtz, J. L. Zilko, and A. Lahav, "Pt/Ti/P-In0.53ga0.47as Low-Resistance Nonalloyed Ohmic Contact Formed by Rapid Thermal-Processing," *Applied Physics Letters*, vol. 54, pp. 2306-2308, 1989.

[64]   D. G. Ivey, "Platinum metals in ohmic contacts to III-V semiconductors," *Platinum Metals Rev.*, vol. 43, pp. 2-12, 1999.

[65]   C. Lin and C. P. Lee, "Comparison of Au/Ni/Ge, Au/Pd/Ge, and Au/Pt/Ge Ohmic Contacts to N-Type Gaas," *Journal of Applied Physics*, vol. 67, pp. 260-263, 1990.

[66]   W. C. Huang and C. L. Lee, "AuGePt ohmic contact to n-type InP," *Journal of Applied Physics*, vol. 79, pp. 9200-9205, 1996.

[67]   M. Harjanne, M. Kapulainen, T. Aalto, and P. Heimala, "Sub-mu s switching time in silicon-on-insulator Mach-Zehnder thermooptic switch," *IEEE Photonics Technology Letters*, vol. 16, pp. 2039-2041, 2004.

[68]   W. Hunziker and H. Melchior, "Low-power compact 2 x 2 thermooptic silica on silicon waveguide switch with fast response," *IEEE Photonics Technology Letters*, vol. 10, pp. 681-683, 1998.

[69]   R. A. Mayer, K. H. Jung, W. D. Lee, D. L. Kwong, and J. C. Campbell, "Thin-Film Thermooptic Gexsi1-X Mach-Zehnder Interferometer," *Optics Letters*, vol. 17, pp. 1812-1814, 1992.

[70]   F. Sun, J. Z. Yu, and S. W. Chen, "A 2x2 optical switch based on plasma dispersion effect in silicon-on-insulator," *Optics Communications*, vol. 262, pp. 164-169, 2006.

[71]   C. Rolland, R. S. Moore, F. Shepherd, and G. Hillier, "10 Gbit/S, 1.56-Mu-M Multiquantum-Well Inp/Ingaasp Mach-Zehnder Optical Modulator," *Electronics Letters*, vol. 29, pp. 471-472, 1993.

[72]   J. E. Zucker, K. L. Jones, B. I. Miller, and U. Koren, "Miniature Mach-Zehnder Ingaasp Quantum Well Wave-Guide Interferometers for 1.3-Mu-M," *IEEE Photonics Technology Letters*, vol. 2, pp. 32-34, 1990.

[73]   N. Agrawal, C. M. Weinert, H. J. Ehrke, G. G. Mekonnen, D. Franke, C. Bornholdt, and R. Langenhorst, "Fast 2x2 Mach-Zehnder Optical Space Switches Using Ingaasp-Inp Multi-Quantum-Well Structures," *IEEE Photonics Technology Letters*, vol. 7, pp. 644-645, 1995.

[74]   M. Fetterman, C. P. Chao, and S. R. Forrest, "Fabrication and analysis of high-contrast InGaAsP-InP Mach-Zehnder modulators for use at 1.55-mu m wavelength," *IEEE Photonics Technology Letters*, vol. 8, pp. 69-71, 1996.

[75]   N. Yoshimoto, Y. Shibata, S. Oku, S. Kondo, and Y. Noguchi, "Design and demonstration of polarization-insensitive Mach-Zehnder switch using a lattice-matched InGaAlAs/InAlAs MQW and deep-etched high-mesa waveguide structure," *Journal of Lightwave Technology*, vol. 17, pp. 1662-1669, 1999.

[76]   D. H. P. Maat, Y. C. Zhu, F. H. Groen, H. van Brug, H. J. Frankena, and X. J. M. Leijtens, "Polarization-independent dilated InP-based space switch with low crosstalk," *IEEE Photonics Technology Letters*, vol. 12, pp. 284-286, 2000.

[77] L. J. Harrison, T. J. Tayag, G. J. Simonis, M. Stead, G. W. Euliss, and R. P. Leavitt, "Monolithic integration of 1.3-mu m Stark-ladder electroabsorption waveguide modulators with multimode-interference splitters," *IEEE Photonics Technology Letters*, vol. 12, pp. 657-659, 2000.

[78] D. A. May-Arrioja, P. LiKamWa, P. Yu, and I. Shubin, "Integrated InP Mach-Zehnder Analog Modulator," *LEOS 2006, The 19th Annual Meeting*, vol. 1, pp. 406-407, 2006.

[79] D. A. May-Arrioja and P. LiKamWa, "Integrated electro-optic Mach-Zehnder switch realized by zinc in-diffusion," *SPIE Proceedings*, vol. 5622, pp. 833-837, 2004.

[80] A. B. Buckman, "Guided-Wave Photonics," *Saunders College Publishing*, 1992.

[81] A. Beaurain, S. Dupont, H. W. Li, J. P. Vilcot, C. Legrand, J. Harari, M. Constant, and D. Decoster, "Characterization and fabrication of InGaAsP/InP deep-etched micro-waveguides," *Microwave and Optical Technology Letters*, vol. 40, pp. 216-218, 2004.

[82] T. Aizawa, Y. Nagasawa, K. G. Ravikumar, and T. Watanabe, "Polarization-Independent Switching Operation in Directional Coupler Using Tensile-Strained Multiquantum-Well," *IEEE Photonics Technology Letters*, vol. 7, pp. 47-49, 1995.

[83] J. E. Zucker, K. L. Jones, M. G. Young, B. I. Miller, and U. Koren, "Compact Directional Coupler Switches Using Quantum Well Electrorefraction," *Applied Physics Letters*, vol. 55, pp. 2280-2282, 1989.

[84] H. Y. Wong, M. Sorel, A. C. Bryce, J. H. Marsh, and J. M. Arnold, "Monolithically integrated InGaAs-AlGaInAs Mach-Zehnder interferometer optical switch using quantum-well intermixing," *IEEE Photonics Technology Letters*, vol. 17, pp. 783-785, 2005.

[85] L. B. Soldano and E. C. M. Pennings, "Optical Multimode Interference Devices Based on Self-Imaging - Principles and Applications," *Journal of Lightwave Technology*, vol. 13, pp. 615-627, 1995.

[86] C. Themistos and B. M. A. Rahman, "Design issues of a multimode interference-based 3-dB splitter," *Applied Optics*, vol. 41, pp. 7037-7044, 2002.

[87] M. Kozhevnikov, N. R. Basavanhally, J. D. Weld, Y. L. Low, P. Kolodner, C. A. Bolle, R. Ryf, A. R. Papazian, A. Olkhovets, E. Pardo, J. Kim, D. T. Neilson, V. A. Aksyuk, and J. V. Gates, "Compact 64 x 64 micromechanical optical cross connect," *IEEE Photonics Technology Letters*, vol. 15, pp. 993-995, 2003.

[88] D. J. Bishop, C. R. Giles, and G. P. Austin, "The Lucent LambdaRouter: MEMS technology of the future here today," *IEEE Communications Magazine*, vol. 40, pp. 75-79, 2002.

[89] T. Pertsch, T. Zentgraf, U. Peschel, A. Brauer, and F. Lederer, "Beam steering in waveguide arrays," *Applied Physics Letters*, vol. 80, pp. 3247-3249, 2002.

[90] Q. W. Song, X. M. Wang, R. Bussjager, and J. Osman, "Electro-optic beam-steering device based on a lanthanum-modified lead zirconate titanate ceramic wafer," *Applied Optics*, vol. 35, pp. 3155-3162, 1996.

[91] F. Vasey, F. K. Reinhart, R. Houdre, and J. M. Stauffer, "Spatial Optical Beam Steering with an Algaas Integrated Phased-Array," *Applied Optics*, vol. 32, pp. 3220-3232, 1993.

[92] X. S. Dong, P. LiKamWa, J. Loehr, and R. Kaspi, "Current-induced guiding and beam steering in active semiconductor planar waveguide," *IEEE Photonics Technology Letters*, vol. 11, pp. 809-811, 1999.

[93] D. A. May-Arrioja, N. Bickel, and P. LiKamWa, "Optical beam steering using InGaAsP multiple quantum wells," *IEEE Photonics Technology Letters*, vol. 17, pp. 333-335, 2005.

[94] D. A. May-Arrioja and P. LiKamWa, "An Integrated 1x3 InP Photonic Switch," *LEOS 2006, The 19th Annual Meeting*, vol. 1, pp. 532-533, 2006.

[95] D. A. May-Arrioja, N. Bickel, and P. LiKamWa, "Reconfigurable 1x4 optical switch in InGaAsP multiple quantum wells," *SPIE Proceedings*, vol. 5622, pp. 828-832, 2004.

[96] D. A. May-Arrioja, N. Bickel, and P. LiKamWa, "Integrated beam-steered optical switch," *SPIE Proceedings*, vol. 5435, pp. 91-96, 2004.

[97] R. Papannareddy, W. Ferguson, and J. K. Butler, "Current Spreading and Carrier Diffusion in Zinc-Diffused Multiple-Stripe-Geometry Lasers," *Applied Physics Letters*, vol. 50, pp. 1316-1318, 1987.

[98]   T. Kumar, R. F. Ormondroyd, and T. E. Rozzi, "Numerical-Solution of Lateral Current Spreading and Diffusion in near-Threshold Dh Twin-Stripe Lasers," *IEEE Journal of Quantum Electronics*, vol. 21, pp. 421-433, 1985.

[99]   G. Lengyel, P. Meissner, E. Patzak, and K. H. Zschauer, "An Analytical Solution of the Lateral Current Spreading and Diffusion Problem in Narrow Oxide Stripe (Gaal)as Gaas Dh Lasers," *IEEE Journal of Quantum Electronics*, vol. 18, pp. 618-625, 1982.

[100]   K. H. Kim, O. K. Kwon, J. H. Kim, E. D. Sim, H. S. Kim, and K. R. Oh, "Monolithically integrated external cavity wavelength tunable laser using beam steering controller," *Electronics Letters*, vol. 41, pp. 1173-1175, 2005.

[101]   A. Olkhovets, P. Phanaphat, C. Nuzman, D. J. Shin, C. Lichtenwalner, M. Kozhevnikov, and J. Kim, "Performance of an optical switch based on 3-D MEMS crossconnect," *IEEE Photonics Technology Letters*, vol. 16, pp. 780-782, 2004.

[102]   T. Goh, A. Himeno, M. Okuno, H. Takahashi, and K. Hattori, "High-extinction ratio and low-loss silica-based 8 x 8 strictly nonblocking thermooptic matrix switch," *Journal of Lightwave Technology*, vol. 17, pp. 1192-1199, 1999.

[103]   T. Goh, M. Yasu, K. Hattori, A. Himeno, M. Okuno, and Y. Ohmori, "Low loss and high extinction ratio strictly nonblocking 16 x 16 thermooptic matrix switch on 6-in wafer using silica-based planar lightwave circuit technology," *Journal of Lightwave Technology*, vol. 19, pp. 371-379, 2001.

[104]   G. A. Fish, B. Mason, L. A. Coldren, and S. P. DenBaars, "Compact, 4 x 4 InGaAsP-InP optical crossconnect with a scaleable architecture," *IEEE Photonics Technology Letters*, vol. 10, pp. 1256-1258, 1998.

[105]   M. P. Earnshaw, J. B. D. Soole, M. Cappuzzo, L. Gomez, E. Laskowski, and A. Paunescu, "Compact, low-loss 4 x 4 optical switch matrix using multimode interferometers," *Electronics Letters*, vol. 37, pp. 115-116, 2001.

[106]   M. P. Earnshaw, J. B. D. Soole, M. Cappuzzo, L. Gomez, E. Laskowski, and A. Paunescu, "8 x 8 optical switch matrix using generalized Mach-Zehnder interferometers," *IEEE Photonics Technology Letters*, vol. 15, pp. 810-812, 2003.

[107]   T. Saida, A. Himeno, M. Okuno, A. Sugita, and K. Okamoto, "Silica-based 2 x 2 multimode interference coupler with arbitrary power splitting ratio," *Electronics Letters*, vol. 35, pp. 2031-2033, 1999.

[108] D. S. Levy, K. H. Park, R. Scarmozzino, R. M. Osgood, C. Dries, P. Studenkov, and S. Forrest, "Fabrication of ultracompact 3-dB 2 x 2 MMI power splitters," *IEEE Photonics Technology Letters*, vol. 11, pp. 1009-1011, 1999.

[109] R. M. Jenkins, J. M. Heaton, D. R. Wight, J. T. Parker, J. C. H. Birbeck, G. W. Smith, and K. P. Hilton, "Novel 1xn and Nxn Integrated Optical Switches Using Self-Imaging Multimode Gaas/Algaas Wave-Guides," *Applied Physics Letters*, vol. 64, pp. 684-686, 1994.

[110] J. M. Heaton, R. M. Jenkins, D. R. Wight, J. T. Parker, J. C. H. Birbeck, and K. P. Hilton, "Novel 1-to-N Way Integrated Optical Beam-Splitters Using Symmetrical Mode Mixing in Gaas/Algaas Multimode Wave-Guides," *Applied Physics Letters*, vol. 61, pp. 1754-1756, 1992.

[111] O. V. Mishechkin and M. Fallahi, "Sol-gel-derived 4X4 multimode interference coupler: optimization and fabrication," *Optical Engineering*, vol. 43, pp. 662-666, 2004.

[112] S. Nagai, G. Morishima, H. Inayoshi, and K. Utaka, "Multimode interference photonic switches (MIPS)," *Journal of Lightwave Technology*, vol. 20, pp. 675-681, 2002.

[113] C. H. Lien, H. H. Lin, S. W. Weng, H. J. Wang, and W. C. Chang, "A compact photonic switch based on multimode interference with partial index-modulation regions," *Microwave and Optical Technology Letters*, vol. 33, pp. 174-176, 2002.

[114] M. P. Earnshaw and D. W. E. Allsopp, "Semiconductor space switches based on multimode interference couplers," *Journal of Lightwave Technology*, vol. 20, pp. 643-650, 2002.

[115] J. Leuthold and C. H. Joyner, "Multimode interference couplers with tunable power splitting ratios," *Journal of Lightwave Technology*, vol. 19, pp. 700-707, 2001.

[116] M. Yagi, S. Nagai, H. Inayoshi, and K. Utaka, "Versatile multimode interference photonic switches with partial index-modulation regions," *Electronics Letters*, vol. 36, pp. 533-534, 2000.

[117] D. A. May-Arrioja, N. Bickel, and P. Likamwa, "Robust 2 x 2 multimode interference optical switch," *Optical and Quantum Electronics*, vol. 38, pp. 557-566, 2006.

[118] D. May-Arrioja, P. Likamwa, R. Selvas-Aguilar, and J. Sanchez-Mondragon, "Ultra-compact multimode interference InGaAsP multiple quantum well modulator," *Optical and Quantum Electronics*, vol. 36, pp. 1275-1281, 2004.

[119] D. A. May-Arrioja and P. LiKamWa, "Tunable Multimode Interference Devices," *SPIE Proceedings*, vol. 6243, pp. 62430H, 2006.

[120] D. A. May-Arrioja, N. Bickel, R. J. Selvas-Aguilar, and P. LiKamWa, "MMI-based 2x2 Photonic Switch," *SPIE Proceedings*, vol. 6013, pp. 206-211, 2005.

[121] D. A. May-Arrioja, R. J. Selvas-Aguilar, J. Escobedo-Alatorre, P. LiKamWa, and J. J. Sanchez-Mondragon, "Variable Optical Attenuator using Active Multimode Interference Waveguide," *SPIE Proceedings*, vol. 5622, pp. 731-734, 2004.

[122] R. Ulrich and G. Ankele, "Self-Imaging in Homogeneous Planar Optical-Waveguides," *Applied Physics Letters*, vol. 27, pp. 337-339, 1975.

[123] G. J. Liu, B. M. Liang, Q. Li, and G. L. Jin, "Beam propagation in nonlinear multimode interference waveguide," *Journal of Optics a-Pure and Applied Optics*, vol. 7, pp. 457-462, 2005.

[124] W. S. Mohammed, A. Mehta, and E. G. Johnson, "Wavelength tunable fiber lens based on multimode interference," *Journal of Lightwave Technology*, vol. 22, pp. 469-477, 2004.

[125] M. Bachmann, P. A. Besse, and H. Melchior, "General Self-Imaging Properties in N X N Multimode Interference Couples Including Phase-Relations," *Applied Optics*, vol. 33, pp. 3905-3911, 1994.

[126] L. B. Soldano, F. B. Veerman, M. K. Smit, B. H. Verbeek, A. H. Dubost, and E. C. M. Pennings, "Planar Monomode Optical Couplers Based on Multimode Interference Effects," *Journal of Lightwave Technology*, vol. 10, pp. 1843-1850, 1992.

[127] M. K. Chin, "Effect of Electroabsorption on Electrorefractive Intensity Modulators," *IEEE Photonics Technology Letters*, vol. 4, pp. 583-585, 1992.

[128] T. C. Huang, Y. C. Chung, L. A. Coldren, and N. Dagli, "Field-Induced Wave-Guides and Their Application to Modulators," *IEEE Journal of Quantum Electronics*, vol. 29, pp. 1131-1143, 1993.

[129] J. I. Shim, M. Yamaguchi, P. Delansay, and M. Kitamura, "Refractive-Index and Loss Changes Produced by Current Injection in Ingaas(P)-Ingaasp Multiple-Quantum-Well (Mqw) Wave-Guides," *IEEE Journal of Selected Topics in Quantum Electronics*, vol. 1, pp. 408-415, 1995.

[130] P. J. Duthie, N. Shaw, M. J. Wale, and I. Bennion, "Guided Wave Switch Array Using Electrooptic and Carrier Depletion Effects in Indium-Phosphide," *Electronics Letters*, vol. 27, pp. 1747-1748, 1991.

[131] C. A. Barrios, V. R. Almeida, R. Panepucci, and M. Lipson, "Electrooptic modulation of silicon-on-insulator submicrometer-size waveguide devices," *Journal of Lightwave Technology*, vol. 21, pp. 2332-2339, 2003.